Chip-Scale Fluorescence Microscope

Efthymios Papageorgiou

Electrical Engineering and Computer Sciences
University of California at Berkeley

Technical Report No. UCB/EECS-2019-31
http://www2.eecs.berkeley.edu/Pubs/TechRpts/2019/EECS-2019-31.html

May 10, 2019

Chip-Scale Fluorescence Microscope

by

Efthymios Philip Papageorgiou

A dissertation submitted in partial satisfaction of the

requirements for the degree of

Doctor of Philosophy

in

Engineering - Electrical Engineering and Computer Sciences

in the

Graduate Division

of the

University of California, Berkeley

Committee in charge:

Professor Bernhard E. Boser, Chair
Professor Mekhail Anwar
Professor Gerard Marriott

Spring 2019

Chip-Scale Fluorescence Microscope

Efthymios Philip Papageorgiou

Abstract

Chip-Scale Fluorescence Microscope

by

Efthymios Philip Papageorgiou
Doctor of Philosophy in Engineering - Electrical Engineering and Computer Sciences

University of California, Berkeley
Professor Bernhard E. Boser, Chair

CMOS image sensors have been widely used for decades, largely displacing CCD technology in cameras, scanners, telescopes, and a variety of medical sensors. Photodiodes are formed in the IC substrate and the technology has been repurposed to make more advanced structures with higher sensitivity, such as pinned or avalanche photodiodes. Less work has gone into generating optical elements using other features of the CMOS process, namely the metal interconnect. The precision deposition and spacing of the metal layers allows a variety of optical structures to be fabricated within the image sensor to perform both spatial and wavelength filtering. This is especially useful for applications where large-scale optical components, such as lenses or fiber optic bundles, cannot be used. For most intraoperative imaging applications and especially for modern minimally-invasive or robotic-assisted cancer surgery, these large optical elements restrict an imager's ability to thoroughly scan an entire tumor cavity.

This thesis presents an image sensor incorporating angle-selective gratings for resolution enhancement in contact imaging applications. Optical structures designed in the CMOS metal layers above each photodiode form the angle-selective gratings that limit the sensor angle of view to $\pm 18°$, rejecting background light and deblurring the image. The imager is based on a high-gain capacitive transimpedance amplifier pixel using a custom 11 fF MOM capacitor, achieving $8.2\,\mathrm{V\,s^{-1}\,pW^{-1}}$ sensitivity. The pixel also includes a leakage current minimization circuit to remove signal-dependent reset switch leakage and the corresponding dark current is $14\,\mathrm{aA/\mu m^2}$. The resulting 4.7 mm by 2.25 mm sensor (80 by 36 pixels) is designed specifically for intraoperative cancer imaging in order to solve the pervasive challenge of identifying microscopic residual cancer foci *in vivo*.

A custom amorphous silicon optical wavelength filter is used alongside the image sensor in order to perform fluorescence imaging. The filter rejects excitation light and has over five orders of magnitude rejection at 633 nm. Fluorescence emission light above 700 nm is allowed to transmit through. Several clinically-tested fluorophores, such as IR700DX, are compatible with this wavelength range. The filter is only 15 µm

thick and is suitable for *in vivo* contact imaging applications as it maintains the same high rejection for all angles of incident light.

We demonstrate imaging and detection of foci containing less than 200 cancer cells labeled with fluorescent biomarkers in 50 ms and signal-to-noise ratios greater than 15 dB using the custom image sensor and optical filter. We also demonstrate the detection of microscopic cancer using human tissue and residual tumor in mice models. The absence of large optical elements enables extreme miniaturization, allowing manipulation within a small, morphologically complex, tumor cavity.

To my friends and family.

Contents

List of Figures

List of Tables

Acknowledgments

I would like to thank my advisors, Prof. Bernhard Boser and Dr. Mekhail Anwar, for providing support, advice, and freedom to explore a variety of topics that were interesting to me while I have been at Berkeley. They have always been encouraging and allowed me space to grow as a researcher at my own pace. I would also like to thank Prof. Gerard Marriott for his advice on this thesis and Prof. Kris Pister for being the chair of my qualifying exam committee.

There are a number of colleagues who I have had the pleasure of working with and learning from. I have shared a cubicle with Burak Eminoglu for the past five years and we have had countless technical and non-technical discussions on more topics that I can possibly remember. Behnam Behroozpour was probably the first friend I made in the office and I very much enjoyed our joking and conversations in Swarm Lab. Hao-Yen Tang, Pramod Murali, Yu-Ching Yeh, and Igor Izyumin were also all members of Bernhard Boser's group when I arrived in Berkeley and I can't imagine a more welcoming group of people.

I would like to thank my Berkeley friends from outside Prof. Boser's group. I have been housemates with Andy Michaels for five years and it has been a great experience and friendship. Pratul Srinivasan, Alyssa Zhou, and Mahsa Sadeghi have also been great friends. Pratul's parents, Srinivasan and Preeti, have graciously invited me to their house for Thanksgiving for five years.

From the EECS department, I would like to thank Shirley Salanio for really keeping the department running and being the sole reason that students have any idea what they need to do to graduate. Richard Lossing and Kim Ly in the BSAC office have also been an enormous help to me.

I would like to thank my family, especially my parents Marci and Anargyros, who have supported me and provided advice throughout my entire life. My grandparents, Philip Mann, Jane Collentine, Efthymios Papageorgiou, and Maria Papageorgiou were also a great source of support for me. I would also like to thank my pets so they are immortalized somewhere: Jingle, Samantha, Sabrina, Rex, Fluffy, Lisa, Natalia, Jane, John, Xionati, Ajax, Nellie, Zikos, Max, Jack, Faye, the turtle, and that one fish that never had a name.

Chapter 1

Introduction

Miniaturized optical imaging systems are critical for both consumer and medical applications. These systems are portable and are used in spaces that are not accessible using conventional imagers. Indeed, chip-scale solutions for contact imaging have enabled a variety of applications ranging from optical scanning and fingerprint sensing to lab-on-a-chip or implantable sensors used for medical disease research and diagnosis. Additional applications have been and will continue to be made possible by replacing many of the traditional large-scale optical elements, such as lenses, filters, and gratings, with on-chip structures fabricated in the metal layers of modern integrated circuit (IC) processes.

These on-chip optical techniques take advantage of the material properties and precise alignment of the CMOS metal interconnect and surrounding dielectric. Structures designed to enable 3D imaging [1,2], polarization imaging [3], and optical wavelength filtering [4] have been previously described. However, one of the main attractions of CMOS image sensors is their planar form factor and ability to be scaled to any convenient surface area for contact imaging applications. Comparatively less work has been done to improve the resolution of these contact image sensors. We have developed on-chip optical structures called angle-selective gratings (ASGs) that restrict the angle of incident light allowed to enter the image sensor. The restricted angle-of-view provided by the ASGs not only allows higher resolution images to be obtained, but also blocks out a large portion of background light in applications where signal and background levels are comparable, such as in intraoperative imaging.

More specifically, one of the high impact applications for chip-scale angle-selective contact imagers is the successful treatment of early stage cancers. This treatment requires the surgical removal of microscopic cancer foci from a background of 10^8 to 10^9 physically similar healthy cells. While the goal is often to remove all cancer cells, foci of 200 cancer cells or more represent a clinical threshold in breast cancer staging, worsening patient outcomes, and need to be removed [5]. Similar considerations apply to prostate cancer treatment. Consequently, physicians face a challenging tradeoff between removing excessive healthy tissue or risking leaving tumor behind.

Removal of all disease, both gross and microscopic, is necessary for successful cancer surgery. Tumor cells left in the patient, known as microscopic residual disease (MRD) or a positive margin, significantly increase the chance of cancer recurrence across cancer types. However, identification of MRD intraoperatively remains a pervasive challenge. The lack of accurate spatial information on the presence, location, and quantity of MRD forces physicians to either empirically treat wide areas of normal-appearing tissue with surgery or radiation in an effort to eradicate all cancer cells or risk leaving tumor cells behind. In breast cancer, for example, an estimated 65% [6] of the 230,000 women [7] diagnosed annually in the United States undergo lumpectomy and MRD is found in 25–40 % of these women [8–10]. Left untreated, MRD doubles the local recurrence rate, from 15 % to 30 %, over 15 years [11], and decreases survival [12]. Consequently, re-excision is recommended in many cases [13, 14]. Even empirical resection of additional tissue, also called shave margins, results in a 20 % rate of MRD [10]. Similarly, rates of MRD after radical prostatectomy for high risk prostate cancer range between 20 % and 50 % [15, 16]. However, the tight physical confines of the prostate bed prohibit re-excision. Patients are instead treated with eight weeks of postoperative radiation therapy to the tumor bed, often with months to years of hormone therapy, resulting in both short and long term side effects. Despite these intensive therapies, only 45 % of these patients remain disease free four years later [17]. Therefore, to achieve excellent oncologic outcomes across cancer types, while reducing the need for additional therapy, real-time intraoperative assessment of MRD with precise localization is critically needed.

Pathologic assessment is the gold standard for postoperative MRD evaluation, but it remains elusive in the operating room. In the laboratory setting, microscopic disease is readily identified on the excised tumor specimen surface using a combination of specific molecular labeling and high-magnification microscopic evaluation of a few hundred cells at a time. If cancer is found on the excised tumor surface, it is assumed by proxy that residual cancer is present on the adjacent tissue remaining in the tumor bed. However, tissue processing and microscopy times restrict evaluation to the postoperative setting, necessitating an additional surgical procedure if residual tumor is determined to be present. Inaccurate co-registration of the pathologic specimen to the tumor bed and sampling error on the excised specimen occur frequently and lead to potentially missing MRD.

Successful intraoperative MRD evaluation requires (1) the ability to image the entire surface area, eliminating sampling error, (2) real-time operation, allowing for seamless surgical integration and instant re-excision of residual tumor, and (3) high sensitivity imaging devices. Pure visual or tactile methods for detecting cancer are limited to the detection of millimeter-scale or larger areas of tumor [18, 19], corresponding to 100s of millions of cells. As mentioned above, 200 cells is considered to be a clinical threshold for breast cancer staging. Such small clusters are effectively invisible to conventional methods that do not make use of molecular markers to distinguish tumor cells from their morphologically similar normal tissue counterparts.

In order to perform intraoperative imaging, cancer tissue in the patient needs to be labeled preoperatively. The labeling will not require any extra time during the operation. This can be accomplished using an injection of an antibody-fluorophore compound [20–24]. The antibody molecularly-targets cancer cells and the fluorophore allows visualization of the cancer. These compounds require as little as several hours to bind and the cancer will remain fluorescent for several days. Thus the injection can occur on the same day as the operation or in one of the preceding days as part of the preoperative outpatient workflow. There have been numerous successful clinical trials using this strategy for a variety of cancers including ovarian [25], head and neck [26], breast [27], and esophageal (NCT02129933). There are also several clinical trials ongoing (NCT02422979 for head and neck cancer and NCT03052127 for ocular melanoma). High tumor-to-background ratios have been reported, including in the clinical trials (5-10 in [26] and up to 9 in [27]), indicating that non-specific binding of the molecular agents to healthy tissue remains low enough to allow MRD imaging. The fluorophores used for *in vivo* imaging emit in the far-red and near-infrared where there is negligible tissue autofluorescence. At least several dyes are proved to be non-toxic and are FDA approved, including indocyanine green [28]. Additionally, commercial entities have developed dyes, such as IR700DX and IR800CW, that have been tested successfully in non-human primates [29] and humans [26,27] and are being used in ongoing clinical trials (NCT02422979, NCT03052127).

Despite recent advances in targeted molecular imaging agents to label cancer *in vivo*, imaging devices themselves remain the limiting factor. Current intraoperative fluorescence imagers [25,30] that place a large microscope above the tumor bed require the use of rigid and bulky optics to guide, focus, and filter excitation and emission light. This makes them inadequate for MRD detection for two key reasons: (1) they are restricted to line-of-sight imaging, missing the majority of the complex tumor cavity surface, and (2) they image far from the tumor bed, with reduced resolution and sensitivity as light diverges.

These large-scale fluorescence microscopes are incompatible with the small, 1–3 cm diameter, tumor cavities common in modern minimally invasive surgeries such as lumpectomy and robotic assisted prostatectomy. The entire 3–30 cm^2 surface area of these cavities need to be rapidly imaged (<1 min) by a small, highly maneuverable imager with the ability to detect about 100 to 1000 cancer cells, necessitating imaging speeds of up to 0.5 cm^2/s. Miniaturized optical elements are difficult to fabricate and they often suffer from increased aberrations and other issues such as ghost images [31–33]. Goggle-based approaches [34,35] are easier to use, but suffer from low sensitivity due to the distance from the tumor bed and cannot image the complex tumor cavity sidewalls. A variety of handheld devices for residual cancer detection have been designed that use optical coherence tomography (OCT) [36], spectroscopy [37–39], birefringence [40], magnetic tracers [41], radio tracers [42], or fluorescence [43]. These are either too large to fit inside the resection cavity itself [36] or only image single-points [37–41]. Techniques using fiber optic bundles [42,43] suffer from a fundamental

trade-off of flexibility versus imaging area, prohibiting rapid imaging of the entire tumor bed surface in a small, complex-shaped, resection cavity. Existing compact alternatives do not have adequate resolution to detect microscopic cancer [44, 45]. Other chip-scale sensors requiring microfluidics or tissue samples need handling that is incompatible with the constraints of surgical procedures [4, 46, 47].

A contact image sensor can be designed to eliminate these challenges by largely dispensing with conventional focusing optics. Integrated circuit (IC) technology is ideally suited for contact imaging as it is inherently planar, with thickness ranging from 500 µm down to less than 10 µm [48], and is scalable from single millimeter dimensions [49] up to several centimeters [50], due to the parallel, arrayed nature of the pixels. Scalability and direct integration with surgical tools is therefore possible with minimal form-factor disruption. Consequently, these imagers can be designed for a range of tumor cavity shapes and sizes and easily mounted on highly maneuverable probes, since only electrical signals, rather than light, need to be transmitted outside the tumor cavity. Furthermore, CMOS-based imagers can be disposable due to their low-cost batch fabrication.

We overcome these limitations by introducing a custom CMOS image sensor incorporating an amorphous silicon optical filter and ASGs as indicated above. The optics of conventional microscopes are shrunk down by orders-of-magnitude while retaining the ability to identify 200 tumor cells. The sensor is characterized and demonstrated with 3D cell cultures, human tissue, and mouse tumor models. The miniature size and high sensitivity of our device facilitates its eventual integration into surgical tools, enabling real-time visualization of cancerous tissue without disrupting established surgical procedures.

Organization of the Thesis

This thesis is organized into seven chapters. Chapter 2 details the angle-selective imaging operation and the design of the ASGs used in this work. Chapter 3 describes the presented angle-selective fluorescence contact imaging system and Chapter 4 describes details of the pixel circuit design and operation. The amorphous silicon optical filter is presented in Chapter 5. We present experimental results validating the sensor's ability to detect microscopic and residual cancer in Chapter 6. The conclusion is provided in Chapter 7.

Chapter 2

Angle-Selective Imaging and Grating Design

The goal of angle-selective contact imaging is to replace large optical elements that limit miniaturization. A contact imager only produces a perfect image if the sample is placed directly on the imaging surface. Any distance between the sample and imager surface will allow light to diverge and blur the resulting image. Optical structures, angle-selective gratings (ASGs), can be included within the pixels of the imaging chip to reject light that is not incident perpendicular to the surface of the chip and recover some of the resolution lost due to increased imaging distance. This procedure as well as the design of the ASG structure used in our image sensor will be described in this chapter.

2.1 Angle-Selectivity Function

As illustrated in Fig. 2.1(a), each pixel in the imaging array accepts light from a limited angle of view (AOV) that is set by the ASGs. This AOV can be found from the angle-selectivity function, $f(\theta)$, of the gratings. The ideal angle-selectivity function, $f_{ideal}(\theta)$, would have a uniform response up to a specific angle, θ_{crit}, as shown in the left part of Fig. 2.1(b). Given knowledge about the size and shape of the objects to be imaged, θ_{crit} can be chosen such that in the resulting image all of the signal from the imaged object is contained in a single pixel, as illustrated in the right part of Fig. 2.1(b). Practical structures conforming to the design rules for CMOS metal interconnect do not have a perfect angle-selectivity function. As shown in Fig. 2.1(c), these structures have a more smoothly varying function, $f_{real}(\theta)$, and there will be some blurring between adjacent pixels in the captured image.

As long as the angle-selectivity function is well defined and the imaging distance is known, the point spread function (PSF) of the imaging system can be estimated accurately. A more selective angular response makes the estimate of the PSF insen-

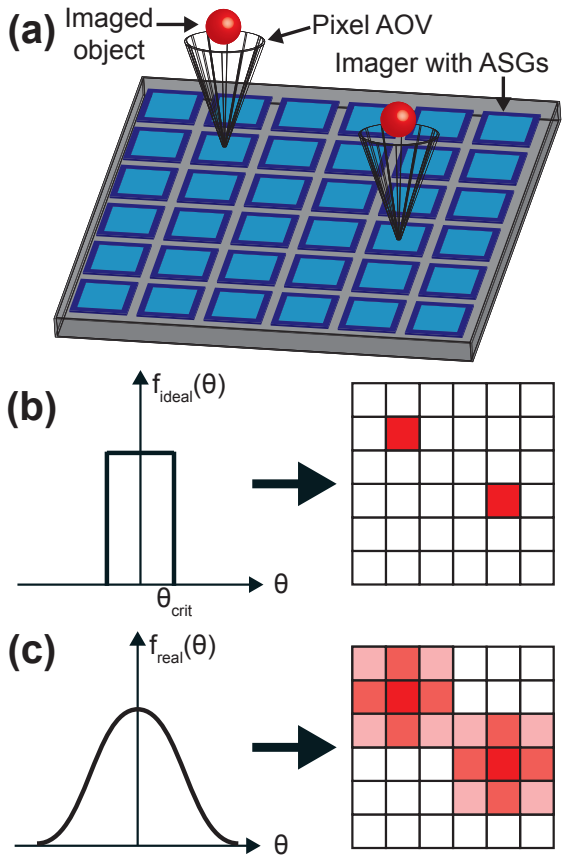

Figure 2.1: (a) Angle-selective imaging operation. Each pixel has a restricted angle-of-view to enhance image resolution. (b) Ideal angle-selectivity function and captured image. (c) Realistic angle-selectivity function and captured image.

sitive to variation in the actual imaging distance, which is nominally set by a spacer placed over the surface of the sensor. The PSF is analogous to the impulse response of a dynamic system and can be used to predict the resulting image, $I(x, y)$, using:

$$I(x, y) = S(x, y) * PSF(x, y), \tag{2.1}$$

where $S(x, y)$ is the surface being imaged. The inverse operation can also be performed to estimate the original surface using a variety of inverse filter and deconvolution algorithms. Details about the implementation of this approach and results are presented in Section 6.2.

2.2 Angle-Selective Grating Structure

The ASG structure contained in our image sensor is shown in Fig. 2.2 and is included in each sensor pixel. As shown in the top view in Fig. 2.2(a), each ASG

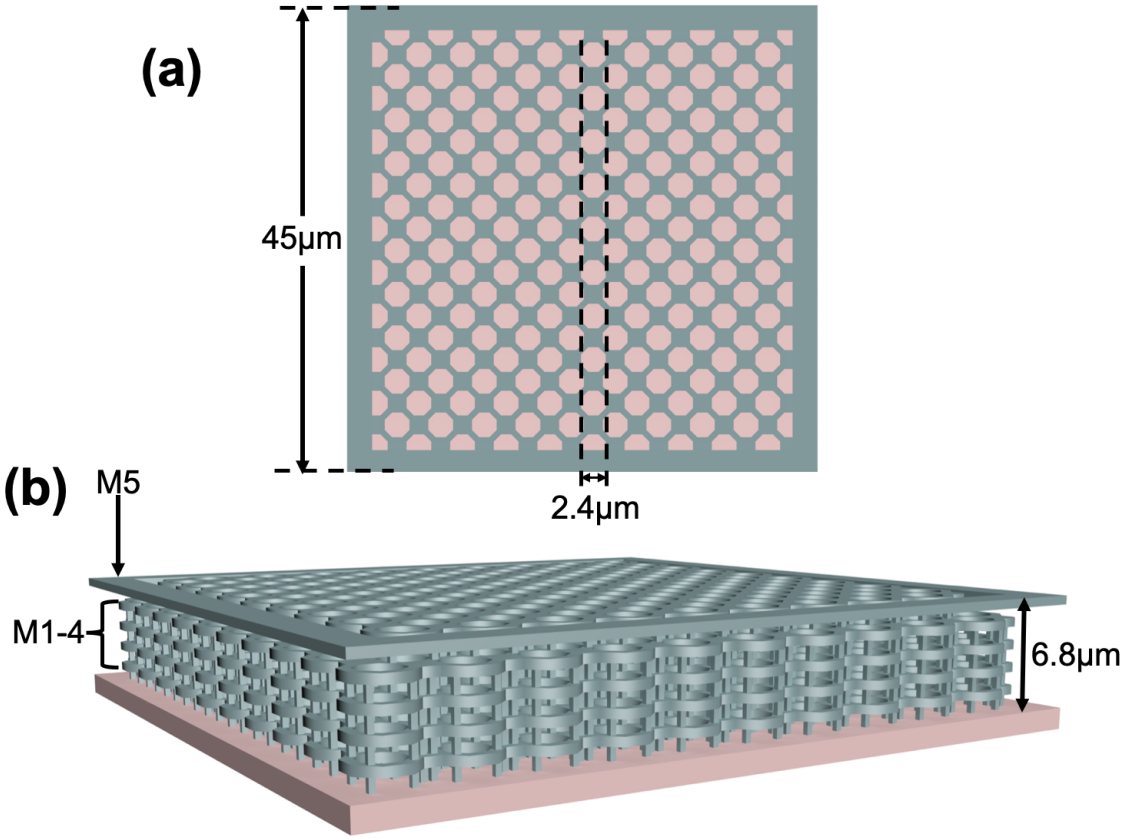

Figure 2.2: (a) Top view of the ASG structure showing octagonally-packed array with 2.4 µm apertures. (b) Perspective side view of the 6.8 µm tall ASG structure in metal layers 1–5.

consists of a 45 µm by 45 µm octagonally packed array with 2.4 µm apertures that completely covers the photodiode in the pixel. The grating blocks approximately 55 % of the photodiode area, leading to a 3.5 dB optical insertion loss. The perspective side view of the ASGs is shown in Fig. 2.2(b). The structure is designed in metal layers 1–5 and is encased in the inter-level dielectric (oxide). All of the metal layers are electrically connected together using vias. Metal layer 6 (the top metal layer) was not used as no chemical mechanical planarization is performed on the IC surface after its deposition. Including metal layer 6 would lead to an unpredictable and uneven surface that can affect the performance of the ASGs by changing the incident angle of light. The entire structure is 6.8 µm tall. This grating structure is natively manufactured in a conventional 0.18 µm CMOS process and does not require any additional fabrication or deposition steps.

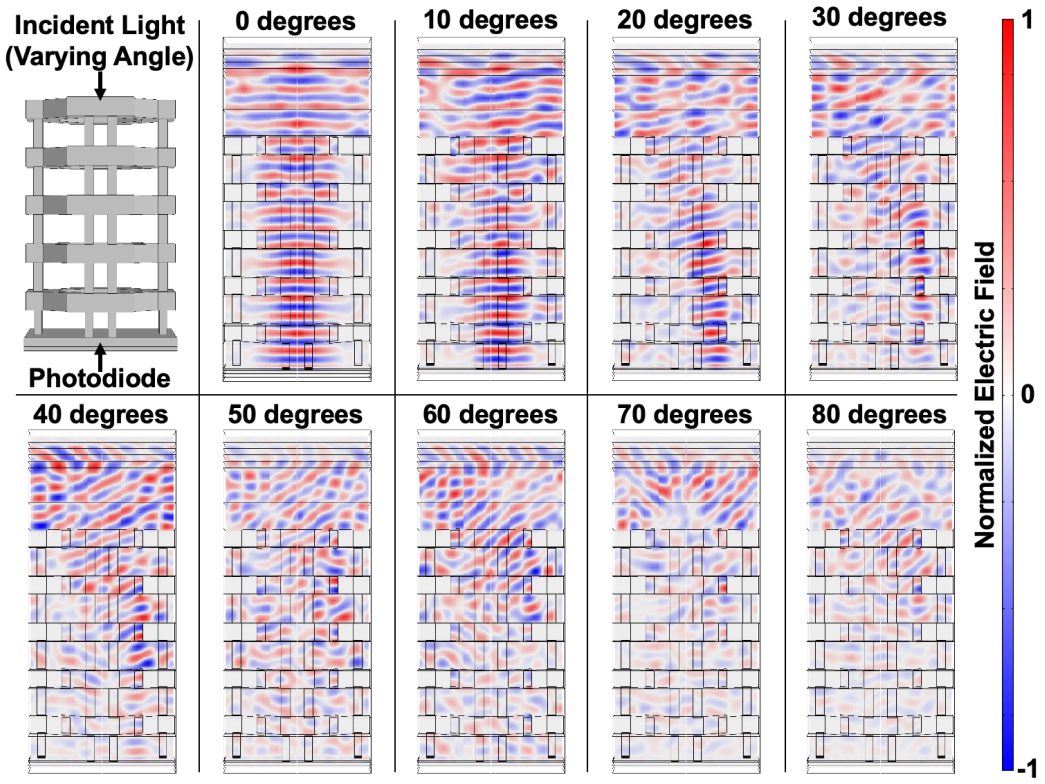

Figure 2.3: ASG 3D FEM simulation for varying incident angle showing increased attenuation for steeper angles. Periodic boundary conditions are used and only a single element in the octagonally-packed array is simulated.

2.3 Angle-Selectivity Simulation and Measurement

The ASG structure was designed and simulated using the finite element method (FEM) in COMSOL. The structure was optimized to provide a sharp angle-selectivity function without an excessively large insertion loss and while keeping to the design rules provided in the used 0.18 µm technology. The simulated field plot of the ASGs for varying incident angle is shown in Fig. 2.3. Periodic boundary conditions were used to reduce the simulation size. Thus only the simulation of a single element in the ASG array is shown. Light is incident from the top side of the structure and the detector (photodiode) is placed at the bottom. As the incident angle is increased, less light is allowed to pass through the ASG and more light is reflected out of the structure. Hence, for each angle, a certain portion of the light reaches the photodiode.

The simulated transmittance of the ASG versus incident angle compiled from the FEM simulations is shown in Fig. 2.4 in blue. In the same plot, we also show the measured response of the ASGs from the fabricated image sensor in red. The two results are in close agreement and the difference between the two is likely due to the imperfect fabrication of the metal structures in the CMOS process (i.e. the

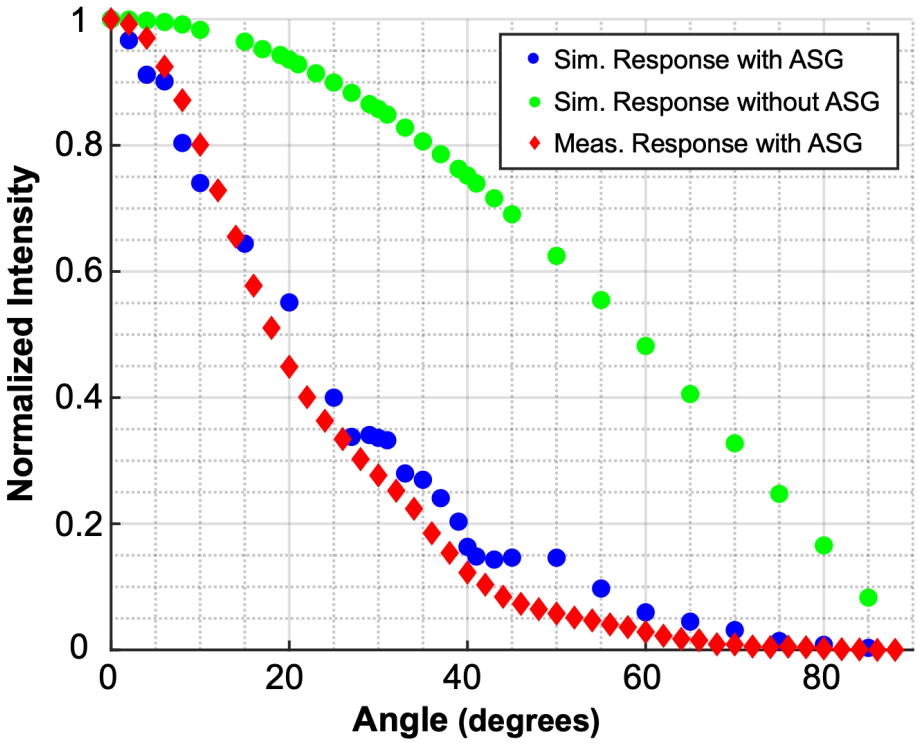

Figure 2.4: Simulated (Sim. in blue) and measured (Meas. in red) ASG response versus input angle showing good agreement. The simulated response of an uncovered photodiode without ASGs (green) is also shown.

fabricated metal wires do not have perfectly sharp edges or corners). The response of the photodiode covered with ASGs decreases to 50 % at approximately 18°, a full width at half maximum (FWHM) of 36°. Also shown in Fig. 2.4 is the simulated response of an image sensor that does not incorporate ASGs. This response is a cosine function with a FWHM of 120°, due to the effective reduction in imaging area as incident light angle increases. The reduced FWHM of the response of the photodiode with ASGs allows it to obtain a higher imaging resolution, as well as block a large portion of background light.

2.4 2D and 3D Signal Calculation Methods for Angle-Selective Imagers

One of the main benefits of including ASGs inside an image sensor in addition to resolution enhancement is the reduction in background light and a subsequent increase in signal-to-background ratio (SBR). In this section, we go over a simple method to calculate the signal levels received by pixels incorporating ASGs when

imaging a 2D surface. We also explain how to extend this method to imaging a 3D volume. These methods can be used to calculate the improvement in SBR due to the presence of ASGs. The 3D method is more accurate, but computationally expensive. However the 2D method provides good insight about the impact of the angle-selectivity function.

If the pixels in an imaging array were selective for only light that is incident perpendicular to the normal vector of the array, then a perfect image could be constructed. However, this scenario is not practical as when the subset of angles of incident light allowed to hit the photodiode is limited to a very small $d\theta$, the received power in the photodiode also approaches 0. A method for evaluating the performance improvements achieved by angle-selectivity must be devised in order to design for a specific application. It can be shown that a small pixel of area A_{pix} across from an infinite plane emitting light of intensity I_0 (power per area) collects a power of

$$P = \tfrac{1}{2} I_0 A_{pix} \int_{\theta_{min}}^{\theta_{max}} \tan(\theta) f(\theta) d\theta, \tag{2.2}$$

from light incident at angles between θ_{min} and θ_{max}. $f(\theta)$ is the angle-selectivity function and the product of A_{pix} and $f(\theta)$ can also be understood as the effective pixel area when looking at the pixel from an angle θ. For a normal photodiode without ASGs $f(\theta) = \cos(\theta)$ as described above.

If a pixel is directly opposite a circular area of interest of radius r on the infinite plane, then the SBR can be found using Eq. 2.2. The signal-to-noise ratio (SNR) can be found using the same equation and the noise performance of the image sensor (see Section 4.5). Light incident on the pixel that originated from within this circular region will be contained in the subset of angles from 0 to θ_{sig}, where $\theta_{sig} = \tan^{-1}(r/h)$, and h is the distance from the surface of the imager to the object. The background light originates outside the circle of interest, at angles greater than θ_{sig}.

Due to the presence of the tangent term inside Eq. 2.2, it is clear that the photodiode receives an increasing portion of light at higher incident angles. This light does not carry much information and it is difficult to determine where it is incident from computationally, particularly if it is incident from somewhere outside the X-Y dimensions of the imaging array. For this reason, it is critical to minimize the angle-selectivity function $f(\theta)$ as much as possible for large θ. This remains true for imaging a 3D volume of tissue as well.

When imaging a 3D volume and especially when imaging a 3D tissue structure light is received not only from the surface, but also from deeper tissue as well. The easiest way to calculate the received signal is to consider the imaged volume as a 3D array of voxels. This scenario is illustrated in Fig. 2.5, however only a 2D slice is shown for simplicity. The light path from each voxel to a pixel on the imaging chip needs to be mapped in order to find the total imaging distance, as well as final angle of incidence on the surface of the chip. This light path will also depend on the index of refraction of the tissue and any other material that is in the imaging

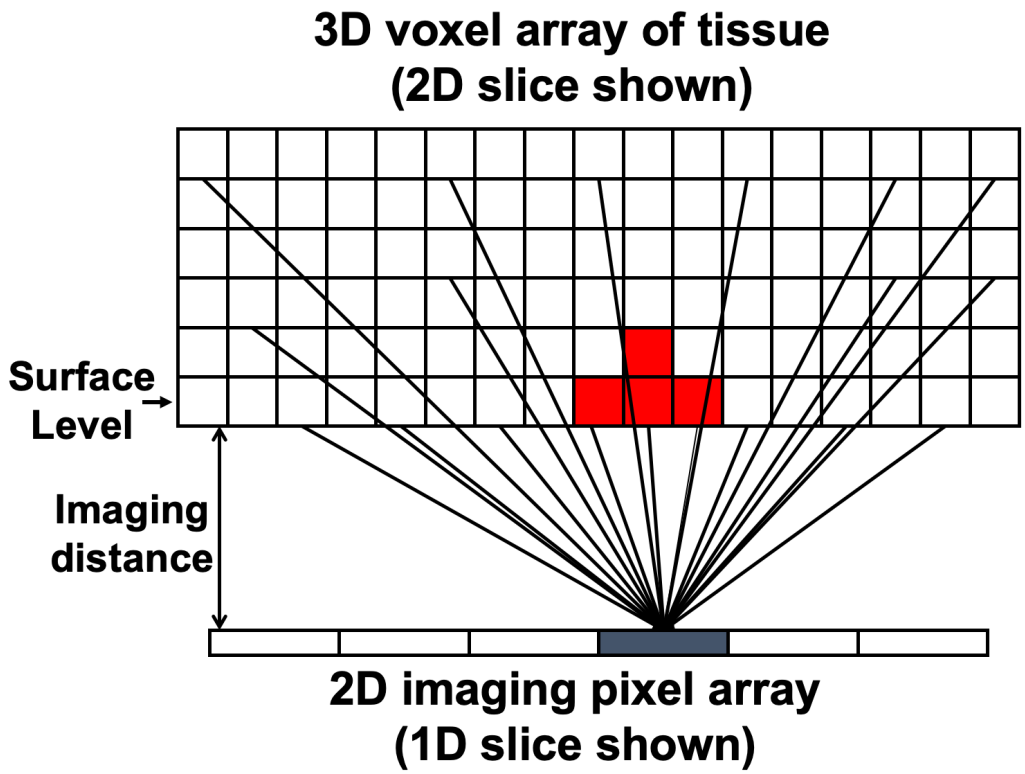

Figure 2.5: Illustration for calculating received pixel signal when imaging a 3D volume. The 3D space is modeled as an array of voxels and the path from each voxel to each pixel in the imaging array must be determined. A 2D slice of the voxel array is shown for simplicity.

path. Additionally for intraoperative imaging, there will be wavelength-dependent scattering and absorption in the tissue that needs to be accounted for as well.

This method can be used to calculate what the resulting image will look like for an arbitrary 3D volume and sensor distance, however it is computationally very expensive and may require significant processing time, depending on the dimensions of the volume to be imaged and required resolution. Alternatively, if the primary interest is to detect cancer on the surface tissue (and high resolution is only required for the surface), a more computationally efficient method is to use the 2D techniques described above. The additional background light that enters the pixel due to the rest of the 3D volume can be calculated by using a low-resolution 3D voxel structure for the deeper tissue beneath the surface. This method retains the advantages of the 2D and 3D approaches, combining the computational simplicity of the former, while maintaining the greater accuracy of the latter.

Chapter 3

Sensor for *In Vivo* Fluorescence Imaging

Image sensors incorporating angle-selective gratings (ASGs) can be used in a variety of applications, including intraoperative cancer imaging. This chapter presents details on fluorescence imaging in general, the system architecture for our angle-selective contact fluorescence imager, the improvement in resolution due to the presence of the ASGs, and a method to calculate expected fluorescence signal levels.

3.1 Fluorescence Imaging

We are performing fluorescence imaging as illustrated in Fig. 3.1. The tumor cells are labeled with a fluorescent probe. This probe consists of a fluorophore conjugated with an antibody that specifically targets and binds to tumor cells. This fluorescent probe can be injected into the patient several hours or days before an operation is performed in order to allow time for the binding to occur [27]. Excitation light (from a laser, shown in blue) is used to excite the fluorophores, causing them to emit at a higher wavelength (shown in red). The emitted light is selected by an optical filter and is then detected by a sensor (photodiode).

3.2 Angle-Selective Contact Fluorescence Imaging System

Traditional fluorescence microscopy as shown in Fig. 3.2(a) requires bulky and rigid optics to maintain dual optical pathways and obtain high quality and high resolution images. Contact imagers dispense with optics and instead rely on proximity to the sample to obtain high spatial resolution and sensitivity by gathering light before it significantly diverges. For *in vitro* systems, the sensor can be placed directly

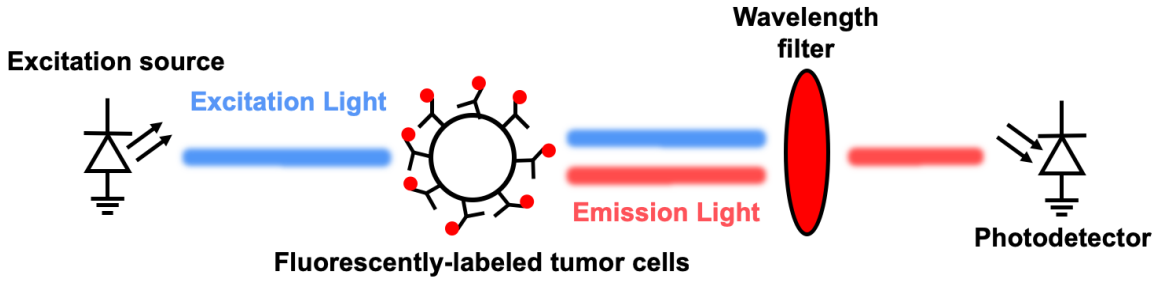

Figure 3.1: Fluorescence imaging operation. The object or sample to be imaged needs to be labeled using a targeted fluorescent molecule. An excitation light source to excite the fluorophores, a wavelength filter to select the fluorescence emission, and a photodetector are needed to perform imaging.

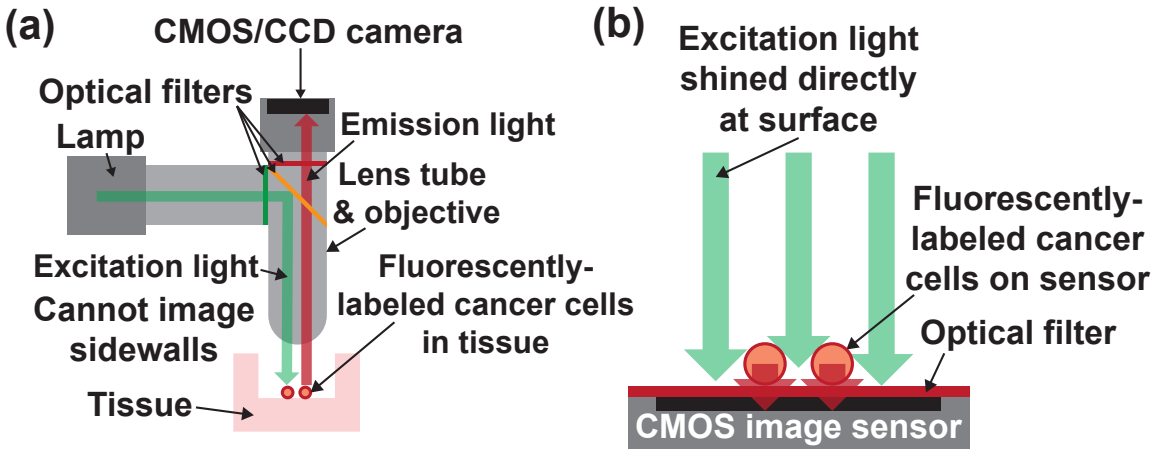

Figure 3.2: (a) Conventional fluorescence microscopes cannot enter the tumor cavity due to their rigid and bulky optical elements. (b) *In vitro* contact imaging can use *en face* illumination. The presence of tissue prevents this method from being used for *in vivo* imaging.

against the sample and excitation light can be applied using illumination through the sample as depicted in Fig. 3.2(b). However, for *in vivo* intraoperative devices, the presence of the human tissue in the traditional *en face* illumination pathway requires oblique illumination from the side of the sensor, precluding direct placement against the tissue.

A diagram of our chip-scale angle-selective fluorescence contact imager is shown in Fig. 3.3. The excitation light can be provided by a linear fiber optic array, collimated light source, or, for a fully-integrated solution, by laser diodes arrayed around the imaging chip. A small gap is needed between the image sensor and the surface containing the labeled cancer tissue in order to apply the excitation light. This gap is provided by a 500 µm thickness fused silica spacer as shown. The minimum spacing

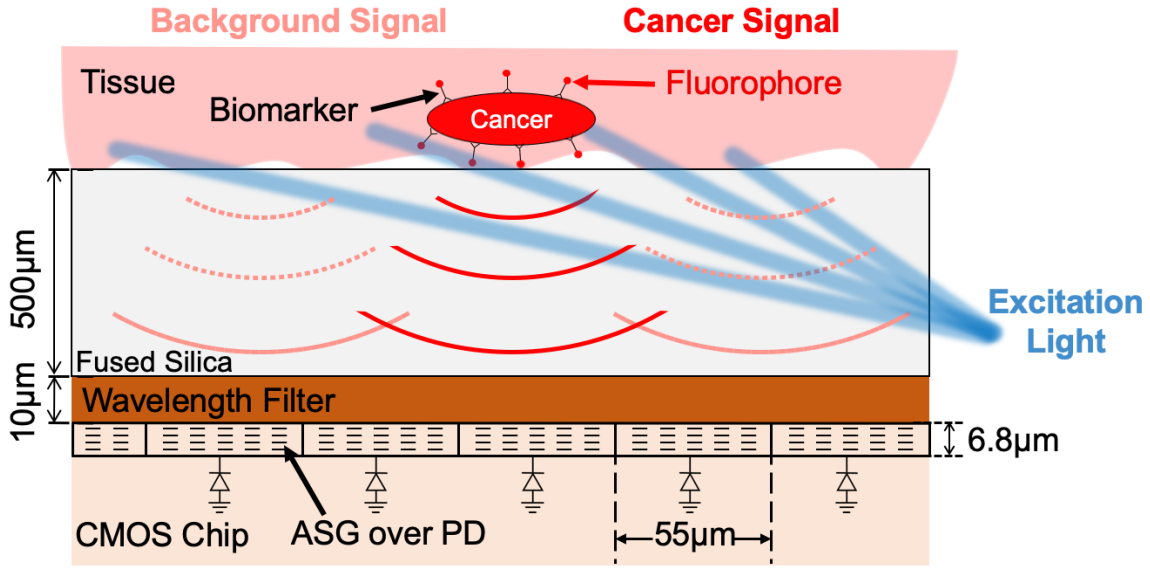

Figure 3.3: Angle-selective contact fluorescence imaging system including labeled cancer tissue, excitation light, optical wavelength filter, and angle-selective imaging chip.

is close to 500 µm for an imager with one dimension equal to 2.25 mm. The required spacing between the tissue and the sensor must allow for excitation at or below the total internal reflection critical angle, approximately 75° for a tissue-glass interface [51]. The critical angle of the fused silica-tissue interface limits this spacing from being reduced further.

The optical filter is a layer on the order of 10 µm thick that allows the fluorescence emission light (shown in red) to pass through, but blocks the excitation light. We are using an amorphous silicon absorption filter (see Chapter 5) in order to block the excitation light at all incident angles while maintaining a small form factor. The angle-selective imaging chip is used to detect the fluorescence and consists of an array of photodiodes covered by the ASGs as described in the previous chapter. The grating layer is 6.8 µm thick, but it does not add any extra imaging distance as it is embedded within the CMOS imager itself.

3.3 Impact of the ASGs on Image Resolution

The resolution of contact imagers degrades with increasing imager-tissue separation due to the divergence of unfocused light. While surgical "resolution" (i.e. the minimum amount of resectable tissue) is on the millimeter to centimeter scale, the need for higher spatial resolution is driven by the requirement to distinguish a small fluorescent residual cancer signal from the background signal due to non-specific

antibody binding to healthy tissue. Given that this background can vary over the tissue surface due to variations in antibody distribution and tissue heterogeneity, high spatial resolution on the order of the cell cluster size to be detected is required for accurate background subtraction and edge detection. The resolution of the contact imager is determined by the angle of view (AOV) of individual pixels and not by the pixel pitch that can be on the micron scale in modern IC processes. Taking the full width at half maximum of the angular response to be the AOV of standard CMOS photodiodes, its value can be in the range 100–120° and often it will not be the same in both the horizontal and vertical directions [52, 53], leading to uneven blurring in the image. This corresponds to a minimum field of view (FOV) for each pixel of approximately 0.6 mm with a 0.5 mm spacing between the image sensor and the imaged sample. This increases to 0.9 mm at 0.65 mm imaging distance. The wide FOV per pixel and rapid loss of image resolution cannot be mitigated by smaller pixel pitch.

In order to improve spatial resolution while minimizing imager-tissue separation, ASGs are included in our imaging chip. The ASGs do not focus light, but rather reject light that is not incident perpendicular to the sensor surface. This results in a reduction of the AOV of each pixel to 36° (see Chapter 2), corresponding to a FOV of 0.22 mm, spanning approximately 120 cells, for a 0.5 mm tissue-to-imager spacing. The FOV increases to only 0.28 µm at an imaging distance of 0.65 mm. This indicates another feature of angle-selective imagers in addition to their higher imaging resolution: they are robust to imaging distance variation. The exact minimum resolvable detail in the resulting image will depend on the exact profile of the angle-selectivity function as described in the previous chapter as well as tissue morphology, but the numbers given here illustrate the benefits of using ASGs. The pixel pitch we have chosen, 55 µm, is smaller than the FOV for typical imaging distances and is chosen such that the resolution is not impacted.

3.4 Fluorescence Signal

The fluorescence signal received from a single cell or a focus of cells can be estimated using information about the cell and antibody binding properties, as well as the imaging distance and imager sensitivity. The signal from a single cell, F (in W), can be expressed as:

$$F = \sigma_{fl} Q_{fl} P_{in} N_{fl}, \tag{3.1}$$

where σ_{fl} is the fluorophore absorption cross section in cm^2, Q_{fl} is the fluorescence quantum yield, P_{in} is the incident light flux in $\mathrm{W/cm}^2$, and N_{fl} is the number of fluorophores bound to the cell. A typical fluorophore that emits in the near-infrared, such as IR700DX, has a quantum yield and absorption cross section of approximately 10–30 % and $10^{-16}\,\mathrm{cm}^2$, respectively [54–56]. A single cell can bind on the order of one million fluorophores and typical excitation powers are close to $100\,\mathrm{mW/cm}^2$.

In order to calculate the received signal during contact imaging from a focus

of cancer containing N_{cell} cells, we need to also incorporate the fluorophore emission profile, the pixel area (A_{pixel}), and the pixel response. Fluorophores uniformly emit radially in all directions, spreading the emitted power over a surface area of $4\pi z_{dist}^2$, where z_{dist} is the imaging distance. The power incident on a single pixel can thus be expressed as:

$$P_{incident} = F \cdot N_{cell} \cdot \frac{A_{pixel}}{4\pi z_{dist}^2}. \tag{3.2}$$

For the typical values given above, an imaging distance of 0.65 mm, and a pixel area of 44 µm^2, 200 cancer cells will provide a signal of close to 150 fW (using 20 % for Q).

The power that is actually received and the current generated in the photodiode will additionally depend on the angle-selectivity function, the insertion loss, L, due to the presence of the angle-selective gratings, and the responsivity, R, of the pixel. The angle-selectivity function is approximately equal to one when considering the pixel directly opposite a cancer cell focus, but needs to be accounted for when computing the background light received by a pixel (which arrives from all angles). The responsivity expresses how efficiently a photodiode or pixel converts incoming light power into the measured output signal, which may be a current or the output voltage. Accounting for all of these parameters, the final output signal is:

$$Signal = F \cdot N_{cell} \cdot \frac{A_{pixel}}{4\pi z_{dist}^2} \cdot f(\theta) \cdot (1 - L) \cdot R. \tag{3.3}$$

It is critical to maximize the pixel responsivity considering the small signal provided by even 200 cancer cells.

Chapter 4

Angle-Selective Imaging ASIC

This chapter goes over the details of the design of the angle-selective imaging chip. The pixel design and performance is especially emphasized as it most significantly impacts the resulting image. In general, it is critical to minimize or avoid introducing any sources of error that are signal-dependent, requiring pixel-by-pixel calibration. This calibration can be complicated and may need to be performed frequently, slowing down the imaging process and making the sensor more difficult to use. Thus, many of the design features incorporated in the pixel are chosen to avoid these signal-dependencies and keep calibration down to a minimum, as described below. Additionally, the pixel noise performance is detailed, with complete expressions provided for the relevant noise sources.

4.1 ASIC Overview

The block diagram of the imaging chip is shown in Fig. 4.1. The chip consists of an 80 (horizontal) by 36 (vertical) array of pixels. Each pixel contains a photodiode covered by an angle-selective grating. The details of the pixel architecture will be explained in Section 4.2. This is a global shutter image sensor and the pixels are read out row-wise onto shared pseudo-differential column lines. Digital row driving circuitry shown on the right selects which row is read and the rows are read sequentially. The 80 differential column lines are multiplexed to eight output lines that are digitized using off-chip ADCs. An FPGA reads the data from the ADCs, performs the digital programming and control of the chip, and also communicates with a PC for real-time data capture and visualization.

The microphotograph of the image sensor appears in Fig. 4.2(a). The sensor is 4.7 mm by 2.25 mm and most of the area (4.4 mm by 1.98 mm) is taken up by the imaging array. The analog column current sources, multiplexers, and buffers are along the bottom row of the array. The digital decoders and row driving circuitry are along the right side. An inset showing a close-up image of four pixels is also shown in

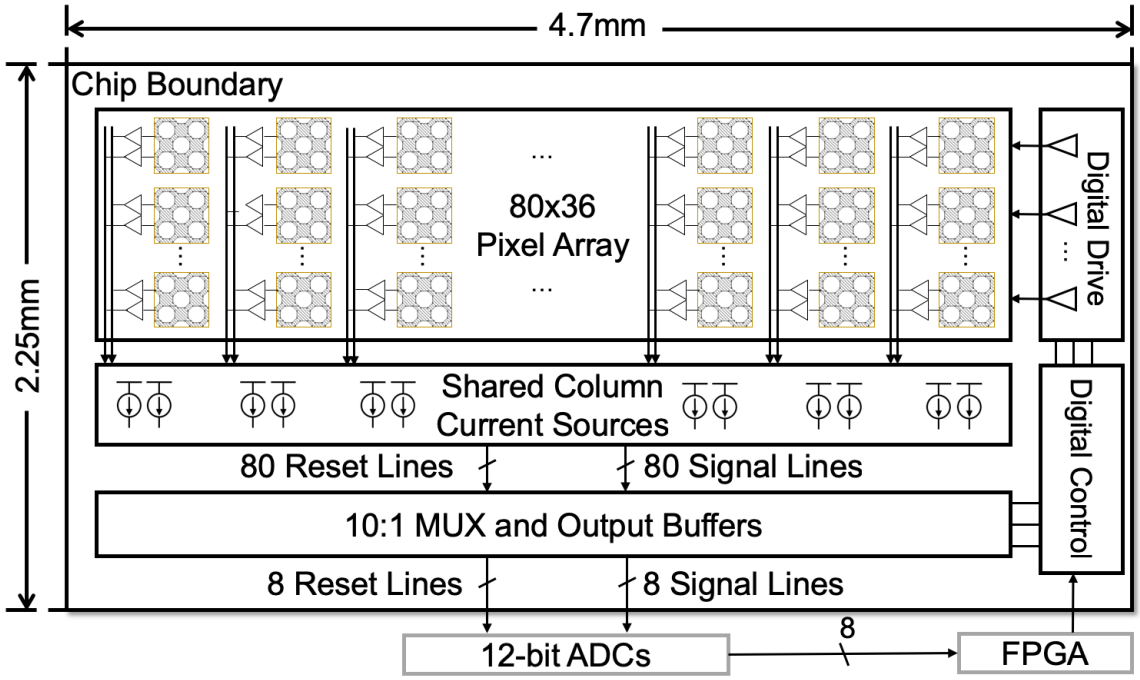

Figure 4.1: Imaging chip block diagram showing 80 by 36 pixel array. The array is read out row-wise on to shared column lines.

Fig. 4.2(b). The angle-selective gratings (ASGs) are visible above each photodiode. The pixel pitch is 55 µm. Each photodiode has dimensions 44 µm on a side and the pixel readout circuitry is placed in the surrounding 11 µm channels. The overall fill factor of each pixel is 28 %, accounting for the area covered up by the ASGs.

4.2 Pixel Operation and Timing

There are a number of challenges associated with ultrasensitive optical detection including signal-dependent dark current, signal-dependent gain and in-pixel offsets. The pixel circuit has been designed to eliminate these error sources in order to avoid extraneous calibration steps that affect the ease of use of the sensor. A custom metal-oxide-metal (MOM) integration capacitor and high gain amplifier is used to ensure a linear pixel response. A leakage current minimization circuit is used to remove signal-dependent reset switch leakage and correlated double sampling (CDS) circuitry suppress offset and noise. The design and operation of the pixel circuit and these elements are discussed in this section and the subsequent sections.

Fig. 4.3(a) shows the architecture of the pixel. This is a customized capacitive transimpedance amplifier (CTIA) architecture that was chosen for its high linearity and accurate gain while maintaining shot noise limited performance. The pixel

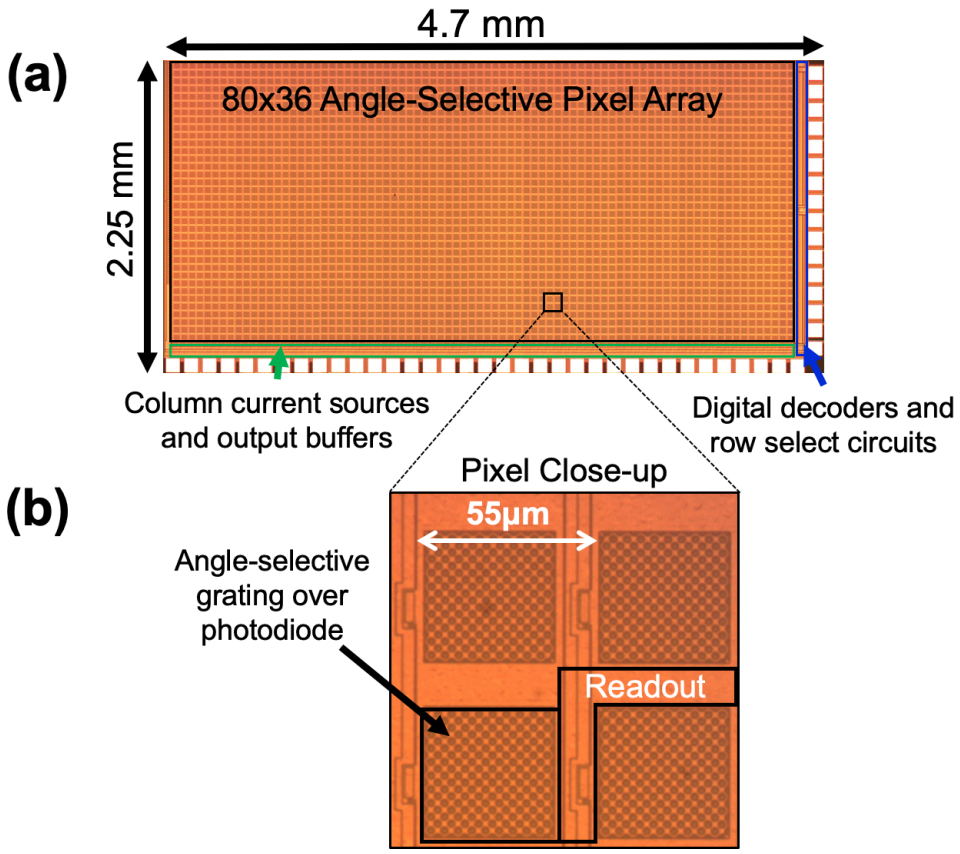

Figure 4.2: (a) Die microphotograph showing imaging array, analog circuitry along the bottom side, and digital circuitry along the right. The chip is 4.7 mm by 2.25 mm and the array is 4.4 mm by 1.98 mm. (b) The inset showing pixels with 55 µm pitch and ASGs over the 44 µm by 44 µm photodiodes.

contains the angle-selective photodiode, an integration capacitor, C_{int}, an amplifier (Amp), a reset switch, two sample-and-hold capacitors, and two source follower (SF) output buffers for readout on the column lines. The timing diagram for the pixel circuit appears in Fig. 4.3(b). Initially Φ_{RST} is high for a time t_{RST} (typically 100 µs) and the reset switch is closed, draining the charge across C_{int}. The signals Φ_R and Φ_S are also high, connecting the load capacitors C_{LR} and C_{LS} to the output of the amplifier. Φ_R goes low a time t_{wait} (also 100 µs) after the reset signal ends, allowing the amplifier to settle, and the initial output value of the amplifier is stored on on C_{LR}. After a further time, T_{int}, equal to the integration time of the amplifier (generally 10 ms to 50 ms), Φ_S goes low, storing a second value on C_{LS}. The difference between the two values is the output voltage of the pixel and is read onto the columns when the row select signal, Φ_{SEL}, goes high during the imaging array readout. The

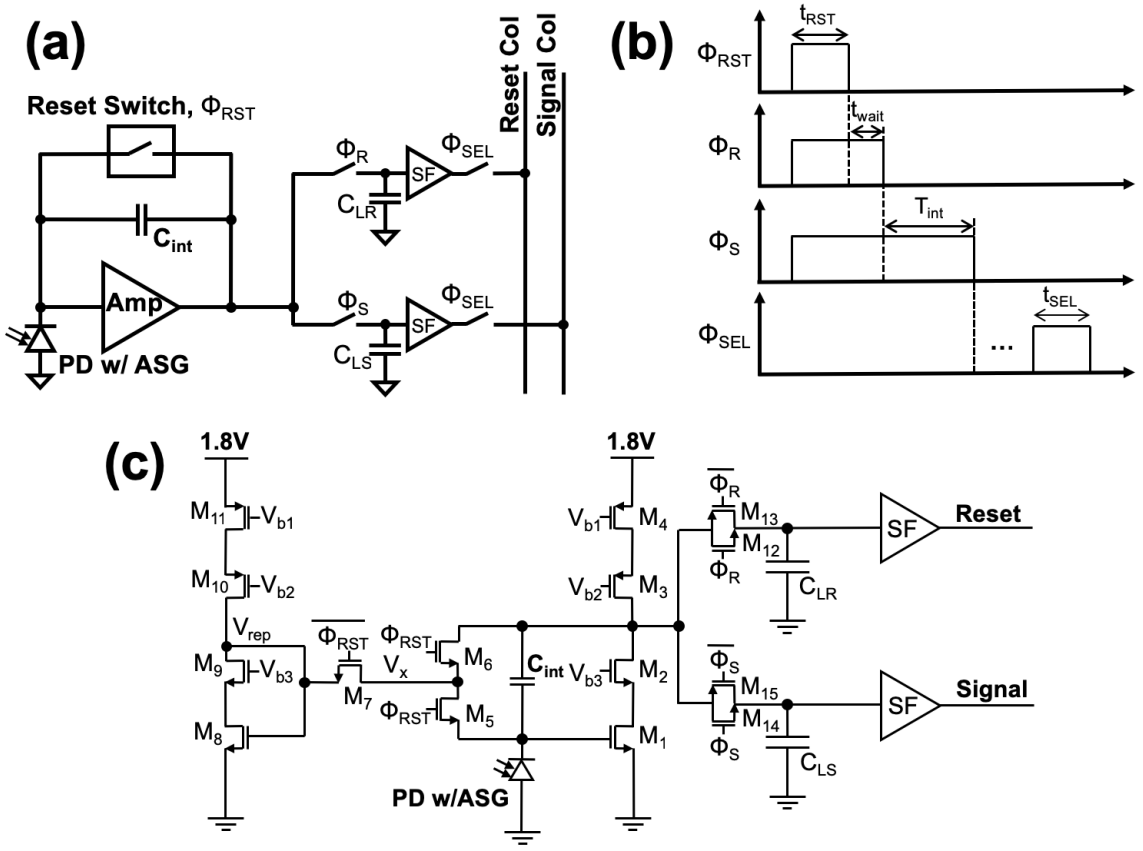

Figure 4.3: (a) General pixel architecture showing photodiode, amplifier, integration capacitor, reset switch, sampling capacitors, and output source follower buffers. (b) Pixel timing diagram. (c) Detailed CTIA pixel schematic showing cascoded common source amplifier implementation and replica reset amplifier for leakage current minimization.

resulting pixel output, V_{out} is

$$V_{out} = \frac{I_{in} \cdot T_{int}}{C_{int}}, \tag{4.1}$$

where I_{in} is the photocurrent generated in the integration capacitor by the input light. Details of the design of this pixel circuit are presented below.

4.3 Pixel Amplifier

The detailed pixel schematic appears in Fig. 4.3(c). The in-pixel amplifier consists of transistors M_1–M_4 configured in a cascoded common source configuration. The bias voltages V_{b1}–V_{b3} are provided through current mirrors placed outside the pixel array and are common to every pixel in the array. The nominal bias current

is 50 nA. This current needs to be high enough to maintain the amplifier gain while charging the load capacitance for the maximum possible input signal level (∼1 pA). The bias current should also be chosen large enough for fast dynamic settling during reset. However, we seek to minimize power consumption as much as possible and so a nominal bias of 50 nA was selected. The integration capacitor is connected between the gate of M_1 and the drains of M_2 and M_3. The sampling switches are full transmission gates consisting of pairs (M_{12}, M_{13}) and (M_{14}, M_{15}). The sample-and-hold capacitance is provided by a pair of MOS capacitors, C_{LS} and C_{LR} that have a nominal value of 150 fF, however, the actual value of these sample-and-hold capacitances depends significantly on the gate voltage level. This voltage-dependency does not affect the operation of the amplifier significantly, but must be accounted for in the noise calculations as described in Section 4.5. The reset switch and replica amplifier, used to drain the charge stored on C_{int} after integration and readout are completed, consists of transistors M_5–M_{11} and are described in more detail in the next section.

An advantage of the chosen CTIA architecture is that the amplifier gain is set by the value of the integration capacitor, C_{int}, rather than the variable and nonlinear photodiode capacitance. This capacitor can be designed as a metal-oxide-metal (MOM) or metal-intrinsic-metal (MIM) capacitor such that its value is independent of the input signal. For this amplifier, we have designed the lateral flux MOM integration capacitor shown in Fig. 4.4(a) with a value of 11 fF, significantly smaller than the 350 fF photodiode capacitance, allowing for a 30 dB higher voltage gain in the pixel. The resulting sensitivity of the pixel is $8.2\,\mathrm{V\,s^{-1}\,pW^{-1}}$ of incident light power. The capacitor is designed in metal layers 2–5 and has dimensions 9.3 µm by 2.7 µm. Some additional area in the pixel is required for this capacitor, but it is not significant compared to the large 44 µm by 44 µm photodiode.

The MIM capacitors in this technology exhibit worse matching (due to imprecise vertical control of the metal spacing) than the chosen lateral flux MOM topology. Mismatch between the gains of different pixels across the array is directly proportionate to the mismatch between the integration capacitors, as well as mismatch in the responses of the photodiodes. We have measured the gain response across the pixels in the array by applying a uniform, collimated, light on the surface of the image sensor and the resulting normalized gain histogram is plotted in Fig. 4.4(b) with a fit to a normal distribution shown in red. The standard deviation is 0.8 %. For typical signal levels up to approximately 550 mV, the gain error will be below the noise of the pixel, and no gain calibration is necessary.

The total power consumption of the entire pixel array is approximately 500 µW. There is an additional 3 mW consumption from the column current sources and output buffers during readout (taking 1.1 ms for the entire array). However, this power can be reduced by turning off these elements while integrating the input light signal.

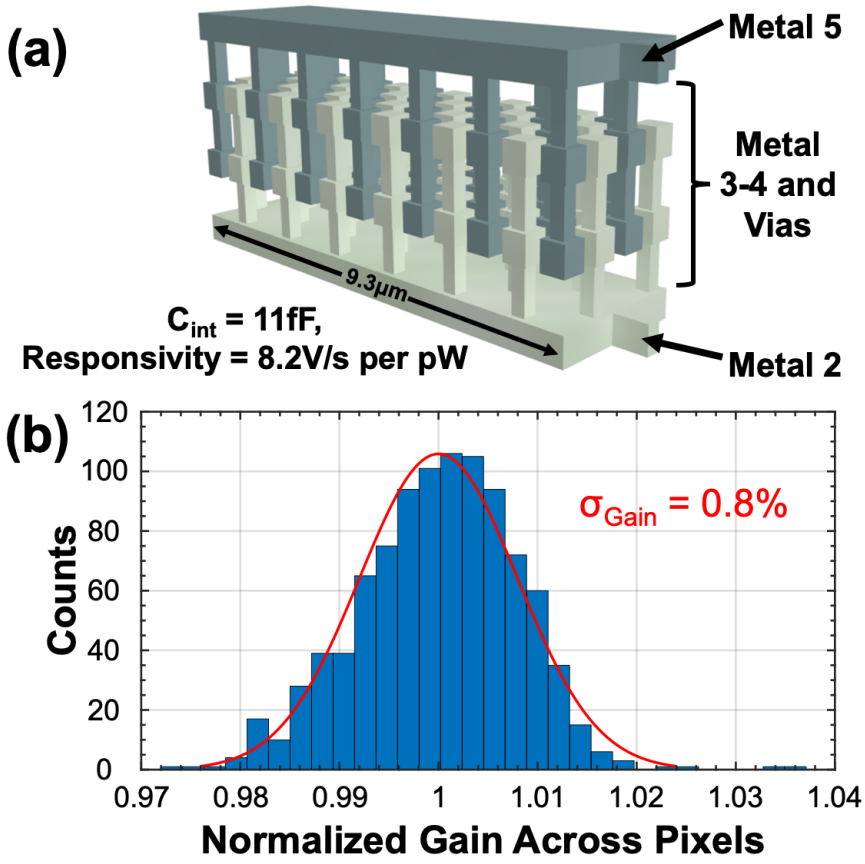

Figure 4.4: (a) Lateral flux MOM capacitor 3D structure. (b) Measured normalized gain histogram across the chip showing 0.8 % standard deviation.

4.4 Leakage Current Minimization

Dark current can present a serious challenge when trying to image small fluorescence signals. Any dark current effectively reduces the dynamic range available for imaging and will increase the amount of shot noise in the captured image. However, if the fluorescence excitation light can be turned off, the dark current itself can be easily canceled at the beginning of the imaging process by taking several dark frames to obtain a pixel-by-pixel estimate of the dark current. This dark current image can be automatically subtracted in hardware or software from the images taken during the fluorescence imaging procedure. However, any signal-dependent leakage will not be canceled by this operation and must be prevented.

Conventionally, a single reset switch is used to drain the charge on C_{int} during reset as shown in Fig. 4.5(a). In this configuration, when the transistor M_R is off during integration, the leakage current will be dependent on the voltage across it, which will in turn depend on the input signal level. This signal-dependent leakage requires complex calibration for each image. In order to avoid this, we have used

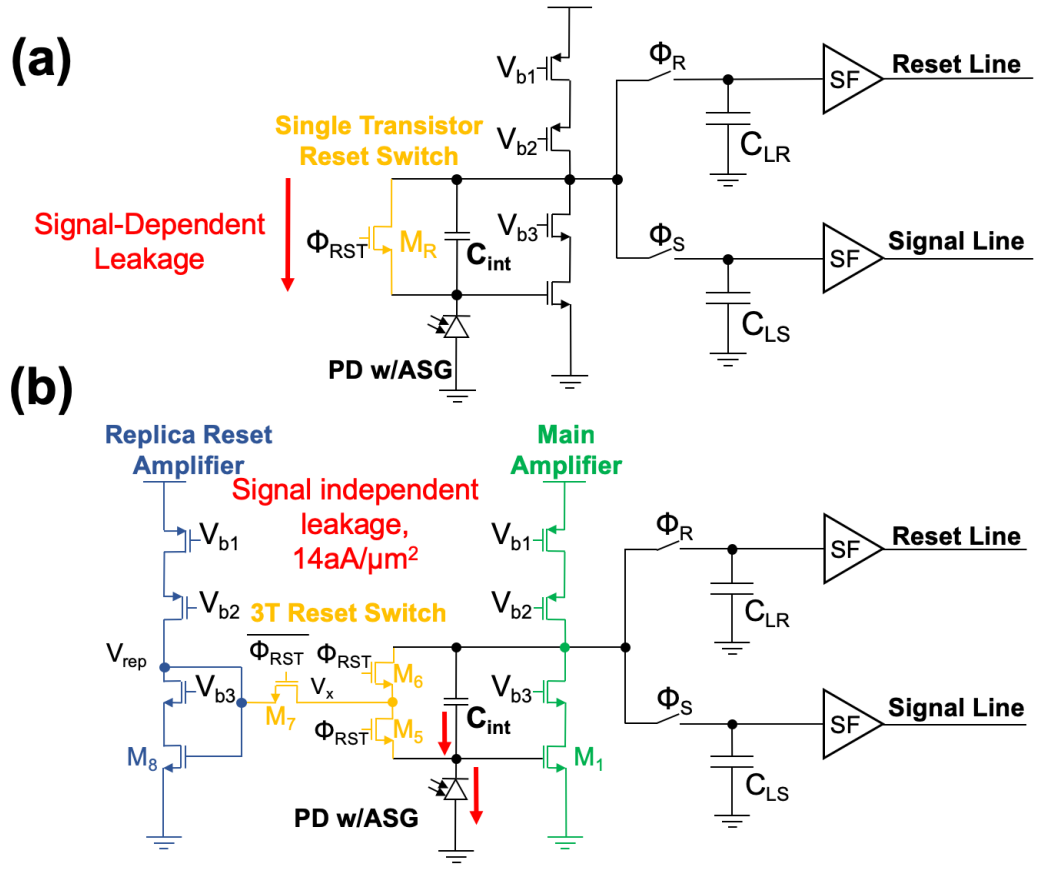

Figure 4.5: (a) A conventional single-transistor reset switch has signal-dependent leakage. (b) The three-transistor reset switch and replica reset amplifier limit the voltage across the reset switch M_5, minimizing leakage current.

the topology presented in Fig. 4.5(b). A three transistor reset switch consisting of M_5, M_6, and M_7 is used. The charge across C_{int} is drained through M_5 and M_6 during reset. During signal integration, these two devices are open and M_7 is closed, connecting the replica reset amplifier and the voltage V_{rep} to V_x. The replica reset amplifier is a duplicate of the main amplifier branch with the same 50 nA bias current. This operation limits the voltage across M_5 to approximately the mismatch voltage between M_1 and M_8, which is on the order of several mV and is signal independent. A histogram of the dark current is shown in Fig. 4.6 measured at room temperature along with a fit to a normal distribution shown in red. The mean dark current in each pixel is 27 fA, 14 aA/μm^2 of photodiode area, and the standard deviation is 3.4 fA.

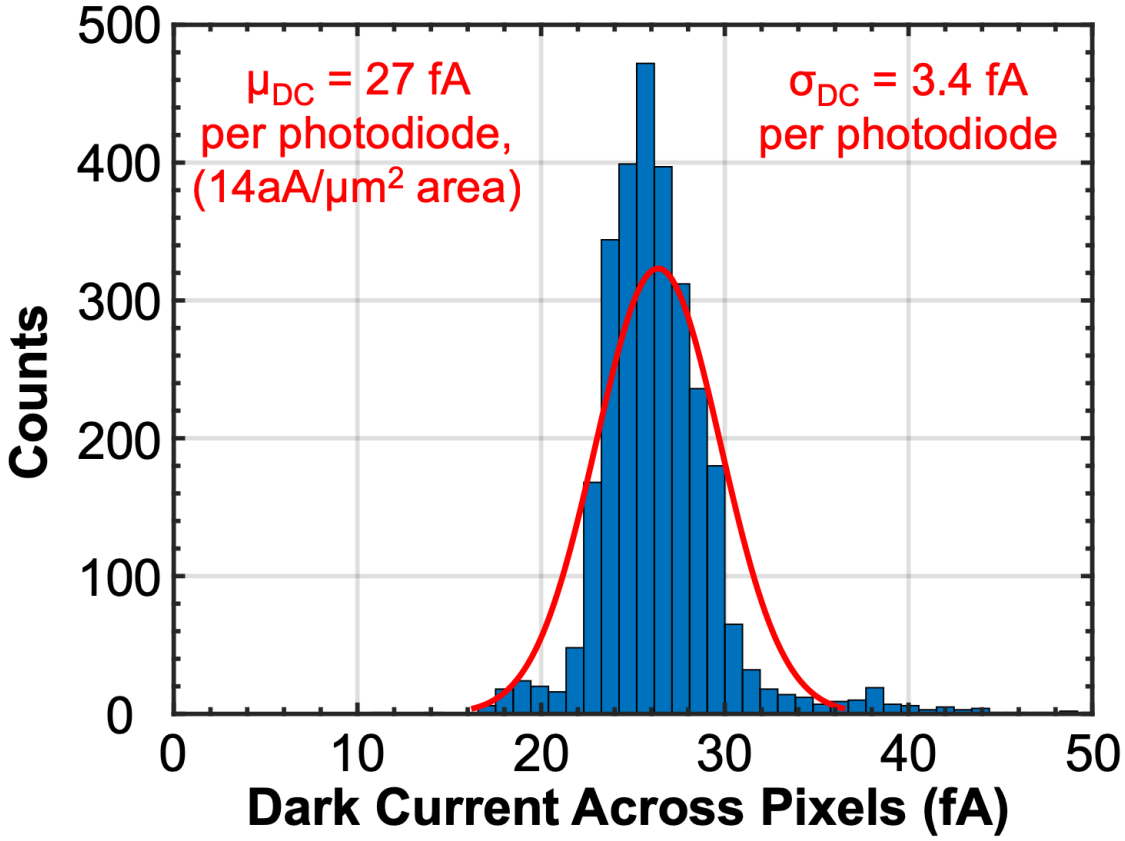

Figure 4.6: Histogram of measured dark current across the chip showing 27 fA mean and 3.4 fA standard deviation.

4.5 Noise Analysis and Measurement

The small integration capacitor and the resulting high gain of the pixel ensures that noise sources other than the pixel noise are negligible even for small fluorescence signals. The main noise sources in the pixel amplifier are shown in Fig. 4.7 and include M_1 and M_2's thermal and flicker noise, the photodiode shot noise, and the noise from the two sampling switches SW_1 and SW_2. Correlated double sampling (CDS) is used in this pixel to cancel the intrinsic amplifier offsets and also helps to suppress the amplifier noise. Two samples are taken during each integration cycle, one at the beginning of integration and one at the end. In general, the noise transfer functions for the same noise source will not be the same at these two different time points. In this amplifier, the loading capacitance changes between these two time points, as the MOM capacitor value depends on the sampled signal level and additionally one of the load capacitors is disconnected to take the first sample (the reset level sample). The noise transfer functions for each noise component can thus be expressed in the

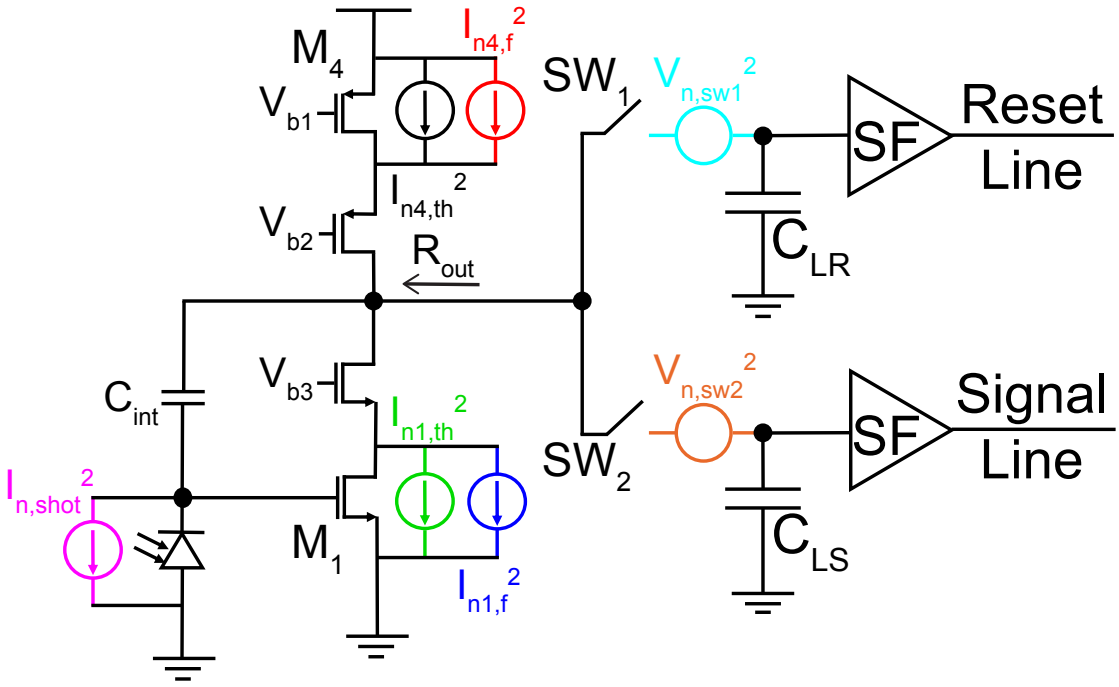

Figure 4.7: Pixel schematic showing thermal, flicker, shot, and switch resistor noise sources.

general form as

$$H_n(s) = H_2(s)e^{-s \cdot T_{int}} - H_1(s), \tag{4.2}$$

where $H_1(s)$ and $H_2(s)$ are the transfer functions at the beginning of integration (right before SW_1 is disconnected) and end of integration (right before SW_2 is disconnected), respectively.

The thermal and flicker noise components all see the same transfer functions. Assuming the switch resistance values are chosen low enough to not interfere with the settling operation of the amplifier, this transfer function can be expressed as

$$H_{n,th,fl,k}(s) = \frac{R_{out}}{1 + sR_{out}C_{Ltot,k}} \quad k = 1, 2, \tag{4.3}$$

where R_{out} is the output resistance of the cascoded common source with C_{int} connected in feedback, $C_{Ltot,1}$ is the total load capacitance right before the reset sample is taken, and $C_{Ltot,2}$ is the total load capacitance at the end of the integration cycle before the second sample is taken. Note that this transfer function represents the transimpedance from a thermal noise or flicker noise current to the output voltage. The output resistance of the cascoded common source is very large, so $R_{out} = \frac{1}{F \cdot g_{mn}}$, where F is the feedback factor of the amplifier and g_{mn} is the transconductance of the transistor M_1. The feedback factor is defined as $F = \frac{C_{int}}{C_{int}+C_{PD}}$, where C_{PD} is the photodiode capacitance. The two load capacitances are $C_{Ltot,1} = C_{LR} + C_{LS} + C_{int}(1 - F) =$

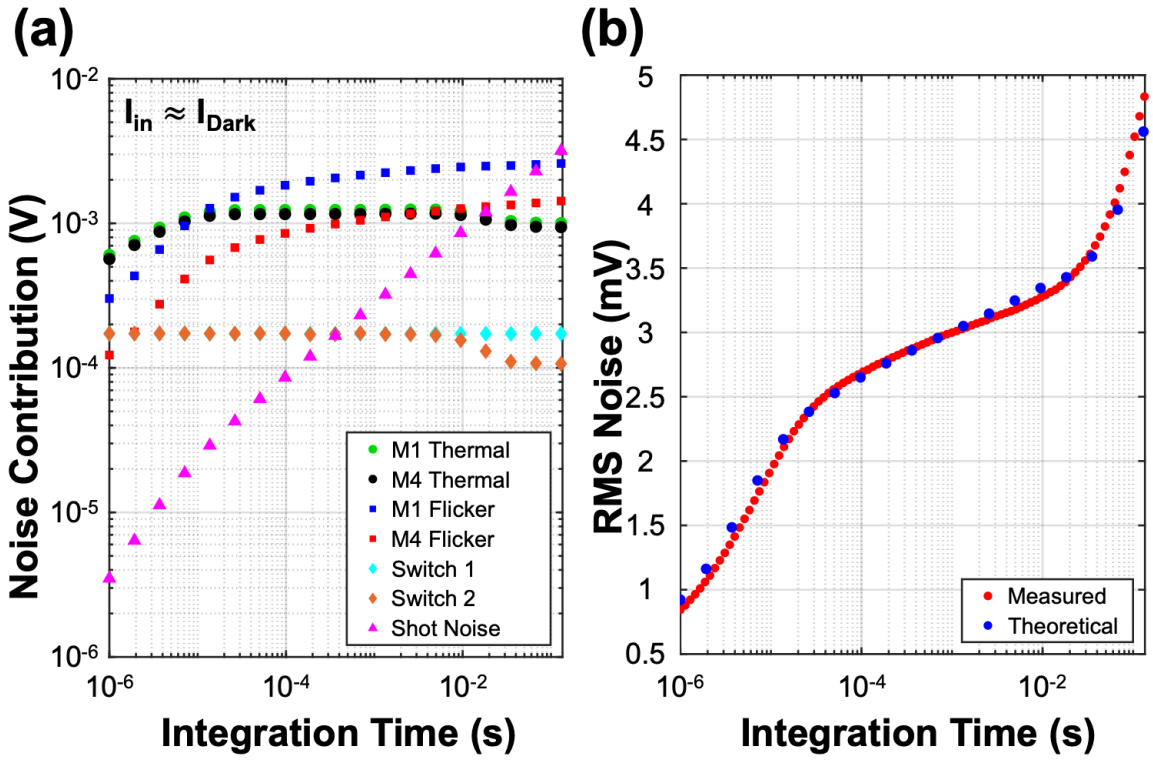

Figure 4.8: (a) Theoretical RMS noise contributions for various noise sources versus integration time for a small input current value close to the dark current. (b) Measured (red) and theoretical (blue) total RMS noise versus integration time showing good agreement.

$2C_L + C_{int}(1-F)$ and $C_{Ltot,2} = C_{LS} + C_{int}(1-F) = C_L + C_{int}(1-F)$, where $C_{LR} = C_{LS} = C_L$.

The shot noise is integrated on C_{int} along with the input signal and has the same transfer function as the input signal. This transfer function can be expressed as

$$H_{n,sh,k}(s) = \frac{\frac{g_{mn}}{sC_{int}} - 1}{s(C_{PD} + C_{L,k} + \frac{C_{PD}C_{L,k}}{C_{int}}) + g_{mn}} \quad k = 1, 2, \tag{4.4}$$

where $C_{L,1} = 2C_L$ and $C_{L,2} = C_L$. Note that the shot noise density is input dependent and expressed as a current ($i^2_{n,shot} = 2qI_D\Delta f$, where I_D is the total diode current), so this transfer function represents a transimpedance once again.

In the above equations, the load capacitors C_{LR} and C_{LS} are MOS capacitors and their capacitance may change throughout integration, depending on input signal level. This varying capacitance must be accounted for and these terms can more generally be written in the form $C_L(V_L)$. This effect is significant in this design, with the initial value of the MOS capacitors being 65 fF at the reset voltage (0.53 V) and increasing up to 200 fF at 1.5 V.

The noise from the resistance of the sampling switches SW_1 and SW_2 is negligible for typical circuit component values, but the corresponding noise transfer function equations are included in the next section along with an explanation on how to find the expanded equations for thermal, flicker, and shot noise that account for the switch resistance.

The RMS noise contribution for each of the noise sources described above versus integration time is plotted in Fig. 4.8(a) for an input diode current approximately equal to the average pixel dark current. Even for this smallest input current, the shot noise is the most significant noise source for the largest integration times, when the dynamic range of the pixel is being completely utilized. Fig. 4.8(b) depicts the total RMS noise in the amplifier versus integration time, showing both the calculated value (in blue) and the measured value from the ASIC (in red). The calculated and measured values are in close agreement. For typical signal levels and integration times, the RMS noise will be close to 4.5 mV.

4.6 Noise Equations Accounting for Switch Resistance

In general, the resistance, R_S, of the switches SW_1 and SW_2 in Fig. 4.7 should be chosen to not limit the settling time of the amplifier ($R_S \lessapprox \frac{R_{out}}{10}$). However if this is not the case, this switch resistance can potentially affect the noise performance. For the switch noise transfer function, it is simplest to look at the impedance divider formed by the load capacitance, the resistance of each switch, and the parallel combination of all the other impedances connected to the output of the in-pixel amplifier. The latter term is expressed as Z_1 at the beginning of the integration time and Z_2 at the end of the integration time:

$$Z_1 = R_{out} \left\| \left(\frac{1}{sC_{int}(1-F)} \right) \right\| \left(R_S + \frac{1}{sC_{L1}} \right), \tag{4.5}$$

$$Z_2 = R_{out} \left\| \left(\frac{1}{sC_{int}(1-F)} \right) \right., \tag{4.6}$$

For SW_2, the noise transfer function is of the same general form as Eq. 4.2 and its transfer function (using a series resistor noise voltage as input) at the beginning of integration can be expressed as:

$$H_{n,SW2,1}(s) = \frac{Z_1}{(1 + sR_SC_{L,1})(Z_1 + R_S + \frac{1}{sC_{L1}})}. \tag{4.7}$$

The transfer function at the end of integration can be expressed as:

$$H_{n,SW2,2}(s) = \frac{1}{1 + sC_{L,2}(R_S + Z_2)}. \tag{4.8}$$

There is no noise transfer function for SW_1 at the end of integration since the switch is open. Thus the noise from this switch is unaffected by CDS and its overall noise transfer function can be expressed as:

$$H_{n,SW1}(s) = \frac{1}{1 + sC_{L,1}(R_S + Z_1)}. \tag{4.9}$$

The complete transfer functions for thermal, flicker, and shot noise can be found most easily by replacing the C_L terms in the expanded versions of Eq. 4.3 and Eq. 4.4 with the term $\frac{C_L}{1+sR_SC_L}$ to account for the different amplifier load impedance and multiplying each equation by $\frac{1}{1+sR_SC_L}$ to account for the low-pass filter behavior of the switch and load capacitance.

Chapter 5

Amorphous Silicon Optical Filter

Instead of conventional thin-film interference filters, we use a novel angle-insensitive optical filter compatible with organic fluorophores used in both animal and human clinical studies, relieving the requirement of tight control over the incident light angle. This filter enables a lens-free fluorescence contact imaging platform. We leverage the intrinsic absorptive properties of amorphous silicon with a band gap of approximately 1.65 eV, to create an angle insensitive long-pass filter above 700-800 nm. This wavelength range is appropriate for clinically used fluorophores such as IR700DX [57], IR800CW [58], and indocyanine green (ICG) [59], as well as commonly used quantum dots. A single thin-film layer achieves over five orders of magnitude of excitation light rejection and can be directly fabricated on top of a CMOS chip, simplifying the manufacturing of fully integrated contact imagers. This filter has been integrated with the previously described imaging chip in order to make a complete imaging system capable of detecting resdidual cancer *in vivo*.

5.1 Oblique Illumination for Intraoperative Contact Imaging

Fluorescence microscopes use the same illumination path for fluorescence excitation and imaging and rely on bulky optical lens systems and dichroic mirrors to seperate light as shown in Fig. 5.1(a). However, the size and rigidity of the microscope lens system restricts it from entering the tumor cavity or imaging its complex sidewalls. The dichroic mirrors, thin-film interference filters, cannot be used in imaging applications where the angle of the excitation light cannot be well-controlled, as will be described in the next section. In contrast to fluorescence microscopes, contact imagers, as shown in Fig. 5.1(b), overcome the dual challenges of sensitivity and maneuverability by dispensing with focusing optics, significantly reducing physical size, and having physical proximity to tissue. *In vitro* contact imagers can use *en face*

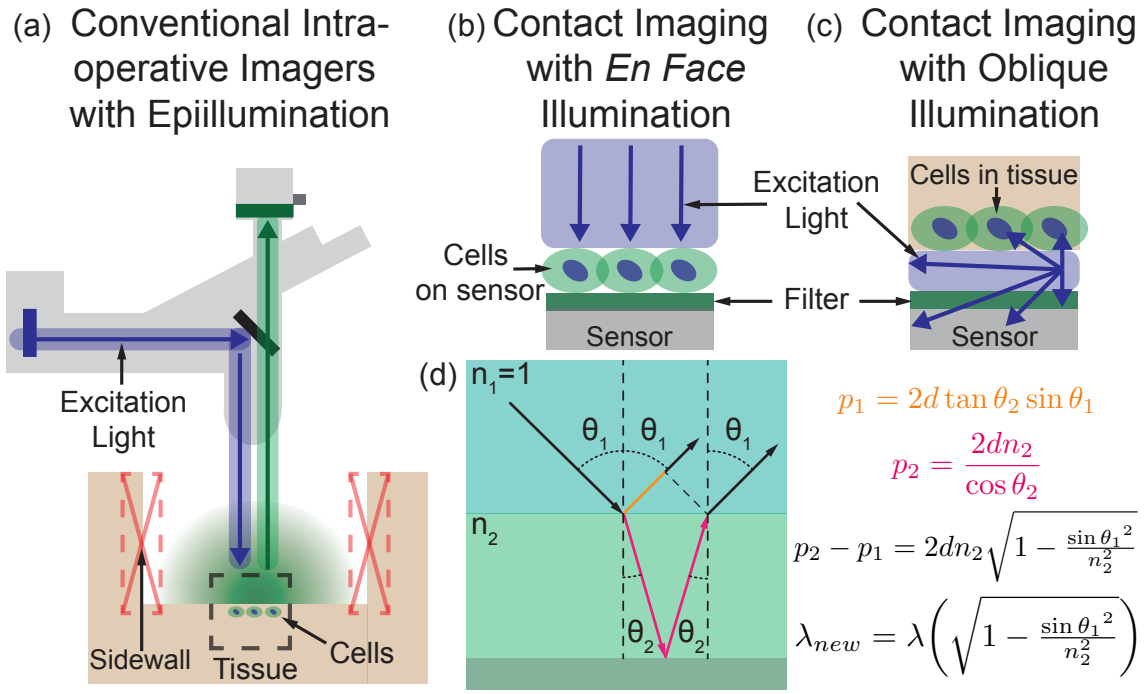

Figure 5.1: (a) Conventional fluorescence microscopes cannot image tumor cavity sidewalls. (b) *En face* illumination contact imagers can only be used *in vitro*. (c) Oblique illumination required for intraoperative contact imagers. (d) Thin-film interference filters' pass-band blue-shifts as illumination angle is increased and cannot be used with oblique illumination.

illumination as they are not physically restricted by the human body tissue [46, 47]. However, oblique illumination is required intraoperatively as depicted in Fig. 5.1(c) due to the tissue proximity. The optical filter needs to not only have high rejection for the excitation light, but also needs to maintain its performance over all incident light angles. Any photon detected by the sensor that does not originate from a fluorophore, including excitation light that leaks through the filter, both consumes pixel capacity and increases shot noise.

5.2 Conventional Optical Filters

Conventional interference filters make use of finely controlled layers of materials with different indices of refraction [60]. Although these filters have high performance for perpendicularly incident light, they suffer from a dependence on the incident light angle. As this angle increases as shown in Fig. 5.1(d), the optical path length difference between path p_1, in orange, and path p_2, in red, blue-shifts the filter response. For small angles of incidence, the spectrum is shifted in wavelength according to

$\lambda_{new} = \lambda[1 - \sin\theta_1^2/n_{eff}^2]^{1/2}$, where λ_{new} is the shifted wavelength, n_{eff} is the effective index of refraction of the filter, and θ_1 and λ are the incident angle and the nominal filter wavelength, respectively. At large angles this effect grows and there is a reduction in filter rejection. Consequently, interference filters allow obliquely incident excitation light to pass directly through and cannot be used in miniature fluorescence imagers.

Alternatives to explicit filters including on-chip wavelength filtering methods [61, 62] generally reduce sensitivity or do not have adequate excitation light rejection for fluorescence imaging applications. Time-resolved methods [63] are not suitable for intraoperative use as the pico to nanosecond decay times of most organic fluorophores are similar to those of molecules inherently present in tissue, making cancer indistinguishable. High speed and high power electronics that consume significant chip area are also required to measure these rapidly decaying signals. Techniques using total internal reflection and compressive sampling [64] work well *in vitro*, but are hard to implement *in vivo* since a sparse signal is required.

5.3 Optical Filter Specifications

Based on the discussion in Section 3.4, a conservative estimate for the fluorescence signal level from 200 cancer cells will be close to 150 fW for a single pixel when using a 100 mW/cm^2 excitation light. This signal power is equivalent to 77.5 aW/µm^2 or 7.75 nW/µm^2 on the surface of the chip. Assuming the excitation light is properly aligned and facing towards the tissue to be imaged, typically only a small amount, close to 1 % or 1 mW/cm^2, of the excitation light will be incident on the surface of the chip. Even accounting for this attenuation, the emission filter must provide over five orders of magnitude rejection for the excitation light to bring it below the signal level for small cancer cell clusters. For image sensors incorporating angle-selective gratings (ASGs), the required rejection may be somewhat less. A large portion of the excitation light is likely to come from oblique angles and be blocked by the ASGs. However, this significantly depends on tissue morphology and high rejection, 10^5 or greater, will still be needed in practice to ensure proper operation under all imaging conditions.

5.4 Amorphous Silicon Material Properties

We can achieve this rejection level for all incident angles while also eliminating the need for precision multi-layer depositions by using an absorption-based filter. The choice of material and thickness depends on the intrinsic bandgap and the steepness of the absorption spectrum fall-off, the Urbach tail, which needs to be considered for amorphous semiconductors. Many organic fluorophores are optimally excited at 30–50 nm below their maximal emission, but they often have broad absorption spectra,

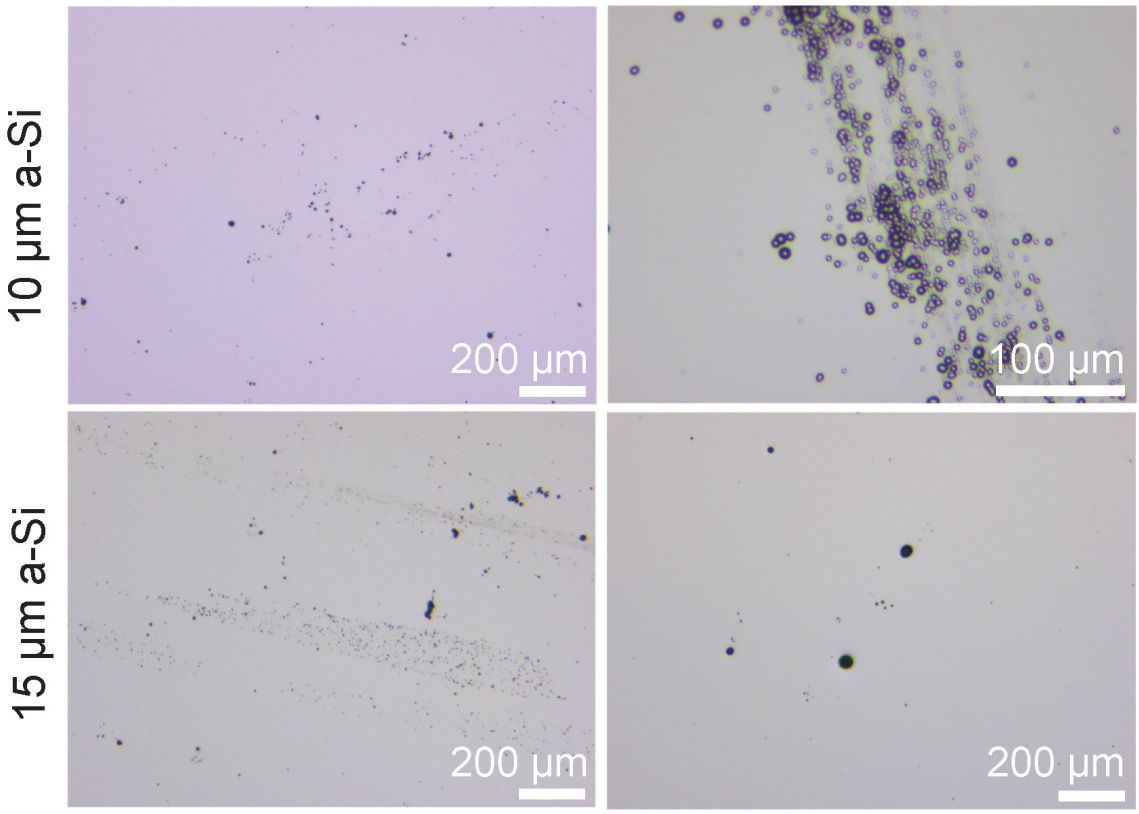

Figure 5.2: Hillock size and density increases as amorphous silicon film thickness increases, but remain sparse enough to obtain areas suitable for imaging.

albeit at lower fluorescence efficiency. Depending on the fluorophore, for a 100 nm difference between excitation and emission wavelengths, only a 50 % reduction in emitted photons is incurred. ICG is a commonly used, FDA-approved, fluorophore with such properties. IR700DX and IR800CW present similar behaviour. The bandgap of amorphous silicon can range from approximately 1.4 eV to 2 eV, depending on fabrication methods, but typically will be close to 1.65 eV [65, 66], corresponding to a wavelength of 750 nm, for the thick layers needed for filtering applications. There is no precise cutoff frequency due to the exponential Urbach tail in the absorption spectrum of amorphous silicon allowing the filter to be designed to work with different fluorophores depending on thickness [66]. Since amorphous silicon begins absorbing photons with energy approximately close to and above its bandgap, a thin layer can be designed to act like a long-pass filter ideally suited to standard optical fluorophores with emission wavelengths from 500–900 nm.

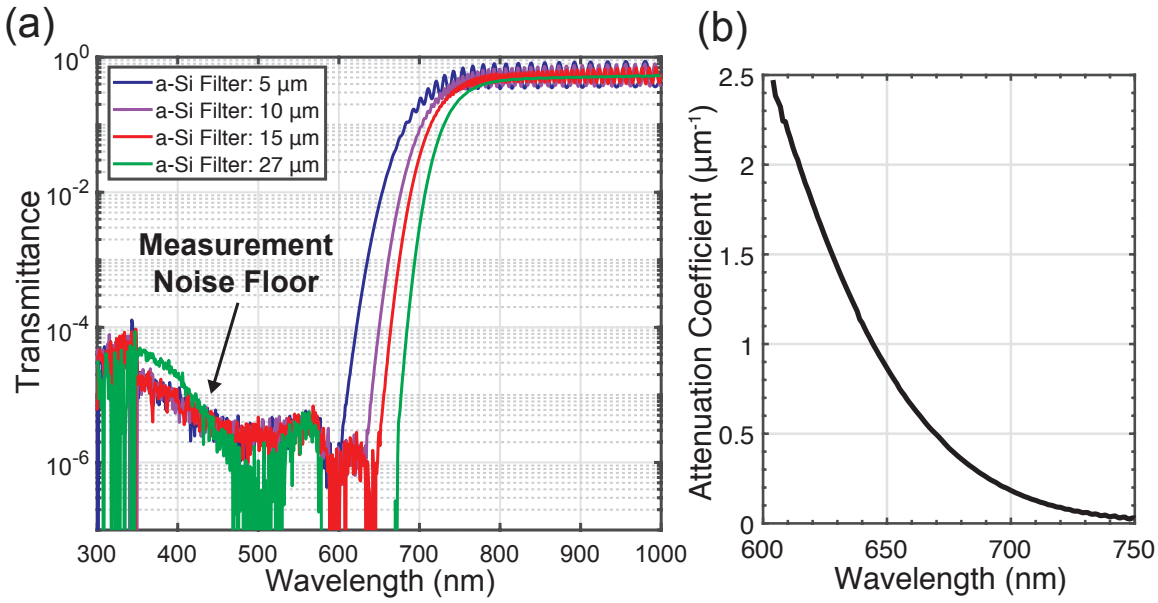

Figure 5.3: (a) Amorphous silicon filter transmittance spectra. (b) Attenuation coefficient extracted from the spectra.

5.5 Measurement Results for Fabricated Amorphous Silicon Filters

To demonstrate this concept, filters were fabricated at the University of Washington, Nanofabrication Facility. Hydrogenated amorphous silicon was deposited onto 500 µm thickness fused silica wafers at a rate of 120 nm/ min using a SPTS APM PECVD with a process pressure and temperature of 1 Torr and 350 °C, respectively. Silane (SiH_4) and argon gas flow into the chamber at 300 sccm and 1500 sccm, respectively. 5 µm, 10 µm, 15 µm, and 27 µm thick filters were fabricated. Hillock density [67] increases with increasing film thickness over some areas of the wafer. The hillocks become noticeable for 10 µm, 15 µm, and 27 µm thickness layers as shown in Fig. 5.2, but remain sparse enough to obtain flat, uninterrupted sections for imaging.

Fig. 5.3(a) shows the transmittance spectra taken using a Perkins Elmer Lambda 850 UV-Vis Spectrometer for the all the amorphous silicon filters. Thicker films push the long-pass transmission wavelength above 700 nm, with a sharper cutoff. At 15 µm thickness, over five orders of magnitude of optical rejection is achieved when illuminating at 633 nm and imaging at 733 nm. The rejection at 633 nm is 60.7 dB. The transmission in the pass-band is approximately 54 %, an insertion loss of 2.7 dB, mainly due to reflection off the high refractive index, 4.3, amorphous silicon. The ripple in the pass-band is due to interference effects in the thin filter layer. Fig. 5.3(b) displays the absorption coefficient versus wavelength extracted from the transmittance curve data. The spectra are fit to $T = exp(-d\alpha)$, where T is the tranmittance, d

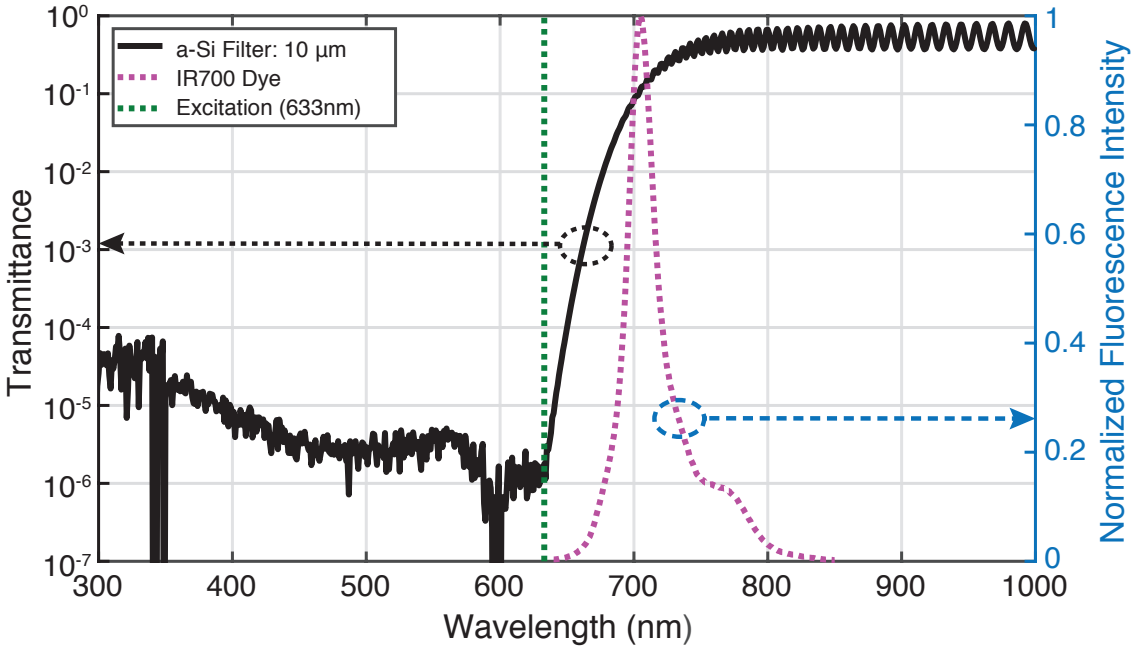

Figure 5.4: 10 µm amorphous silicon filter measured transmittance spectrum overlaid with the IR700DX dye emission spectrum and 633 nm excitation line.

is the layer thickness, and α is the attenuation coefficient. The optical properties of our amorphous silicon filter agree with previously published work [65,66,68]. Fig. 5.4 shows the 10 µm film thickness transmittance data overlaid with the excitation point and emission curves for IR700DX. This demonstrates that our filter is applicable to commonly used and clinically-tested fluorophores.

Dye-based absorption filters typically have 20–30 dB lower rejection in the stopband for similar thicknesses [69–73]. While dye-based filters have 1–2 dB lower insertion loss in the passband, this can be compensated by increasing excitation light power and the amorphous silicon filter offers a higher contrast due to its superior stopband rejection. Additionally, the amorphous silicon filter can be readily fabricated and patterned with micron-precision at the wafer-level. The insertion loss of the filter slightly increases with angle due to a longer path length, but this effect is negligible due to the high refractive index of the filter that limits the path length increase to less than 1 % for incident angles in the ±18° angle-of-view of the image sensor with ASGs (see Chapter 2).

To demonstrate the angle insensitivity of the amorphous silicon filter compared to that of two thin-film interference filters, ET700/75m and ET705/40m (Chroma), we epoxied 3 mm by 5 mm sections of the respective filters onto the CMOS imager with ASGs using EpoTek 301 epoxy. The amorphous silicon filter was 15 µm thick. We illuminated the sensor with 633 nm collimated light at incident angles from the perpendicular ranging from 0° to 90° and measured the received signal response. A

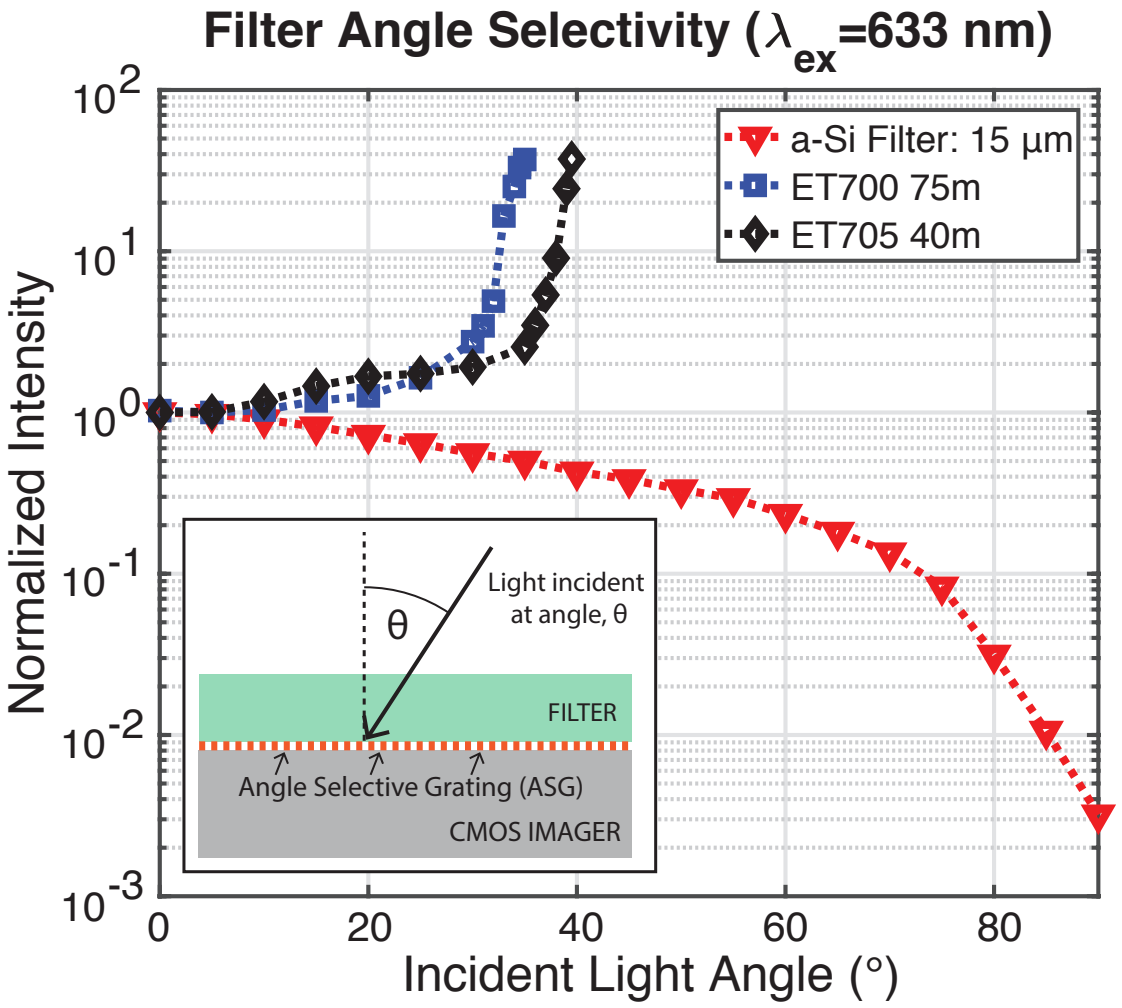

Figure 5.5: Normalized angular response of a CMOS image sensor with ASGs and optical filter using a 633 nm collimated laser source. The performance using two interference filters, ET700/75m and ET705/40m, and the 15 µm amorphous silicon filter is shown.

small fraction of light penetrates the filter providing the signal. The normalized signal versus incident angle for all three filters is plotted in Fig. 5.5. The rejection of the two conventional interference filters degrades gradually with increasing angle below 30°. Above approximately 30°, their rejection degrades exponentially. This behavior makes thin-film interference filters incompatible with applications requiring illumination at even modestly steep angles or where the illumination light may be scattered by human tissue. The signal received by the sensor covered with the amorphous silicon filter smoothly falls off as angle is increased, making the filter suitable for these applications, including intraoperative cancer imaging.

5.6 Other Potential Semiconductor Filters

We have dispensed with conventional thin-film interference filters that have poor angular response and instead use an amorphous silicon absorption filter epoxied onto a custom CMOS image sensor. No large optical elements or physically restricting optical fibers are necessary to control the illumination and emission angles with a filter of this type and without these components, the imager can be miniaturized and placed directly in contact with the tissue surface, enabling rapid intraoperative imaging of fluorescently labeled tumor cells. Our approach, using semiconductors as optical filters, is not limited to only amorphous silicon.

While amorphous silicon is ideal for fluorophores that emit close to 700–800 nm, including Alexa Fluor 700 and IR700DX, it is possible to use other materials compatible with microfabrication, including gallium phosphide (2.25 eV bandgap, 550 nm cutoff), cadmium selenide (1.74 eV bandgap, 710 nm cutoff), gallium arsenide (1.43 eV bandgap, 870 nm cutoff), indium phosphide (1.27 eV bandgap, 980 nm cutoff), and crystalline silicon (1.11 eV bandgap, 1100 nm cutoff). These materials allow a range of fluorophores and imaging systems to be used depending on the application. Care needs to be taken with the fabrication of some of these materials to ensure uniformity, as well as their biocompatibility, but in general the semiconductors listed here will provide high filter rejection and steep transition bands.

Chapter 6

Cell Culture and Tissue Imaging

This chapter describes imaging of a variety of samples, including 3D cell cultures, human breast cancer tissue, and mouse tissue. The 3D cell culture results are used to characterize the imager's sensitivity to cancer cell foci with a wide range of sizes. The tissue results demonstrate the imager's ability to detect residual cancer in an intraoperative setting.

6.1 Imaging Setup

The imaging setup is detailed in Fig. 6.1. The imaging ASIC is shown in Fig. 6.1(a) on the carrier PCB in the left image. The imaging ASIC with an optical filter attached is shown on the right. The optical filter is deposited on a fused silica wafer that is diced to fit the imaging ASIC. After deposition, the diced filters are epoxied on the surface of the ASIC using a clear optical epoxy. Dark epoxy is used for electrical isolation. Fig. 6.1(b) shows the setup for capturing fluorescence microscope images simultaneously with images from the ASIC. The ASIC and carrier PCB are suspended over an inverted fluorescence microscope. A glass slide carrying the sample to be imaged is held in between the two on an X-Y stage. Fig. 6.1(c) shows a diagram of this imaging setup. The imaging ASIC and optical filter are shown at the top of the diagram. The fused silica serves as a spacer that separates the imager from the sample to be imaged and has 500 µm thickness.

The sample to be imaged is placed on a 1.5 mm thick glass slide underneath a coverslip that adds 150 µm to the imaging distance. For large tissue samples, a similar procedure is used as shown in Fig. 6.1(d). An IVIS Spectrum live animal imaging system is used to obtain reference images instead of the fluorescence microscope for these samples due to their large size. The illumination light intensity used for imaging is approximately 7.5 mW and is provided by a collimated laser diode light source.

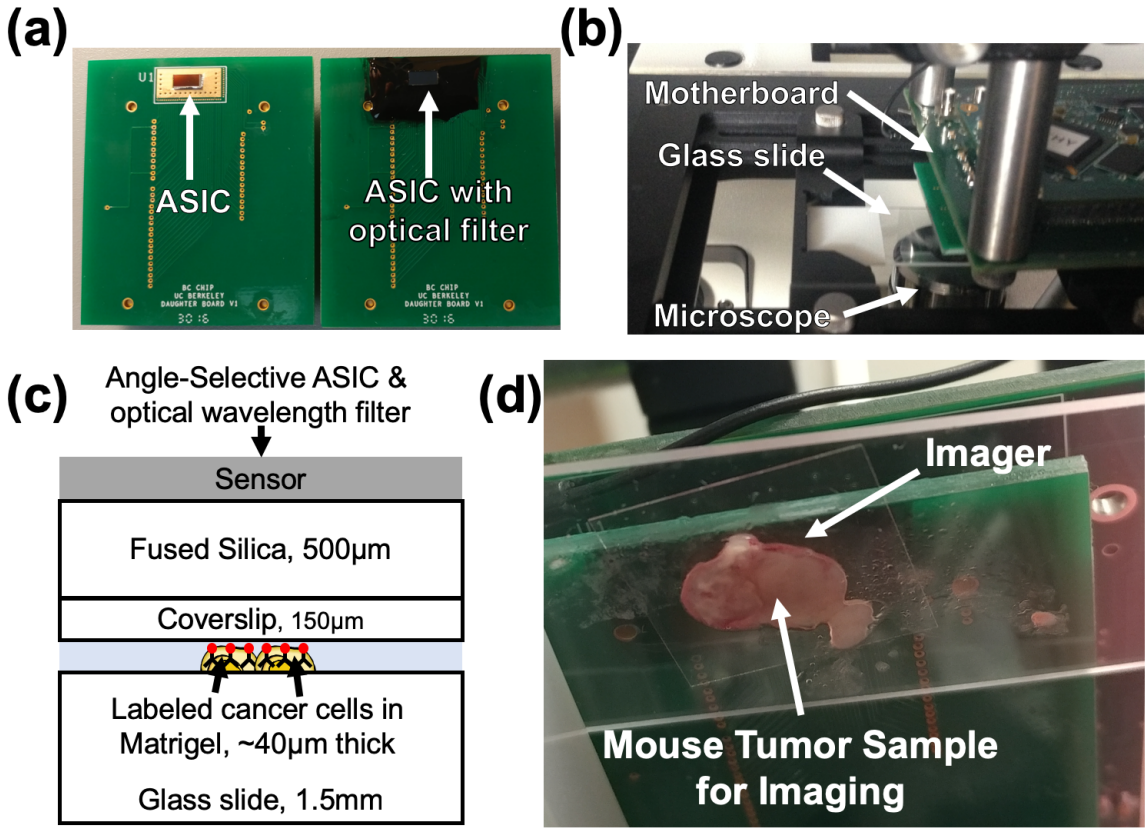

Figure 6.1: (a) Imaging ASIC on PCB both without (left) and with (right) an optical filter. Dark epoxy is used for electrical isolation. (b) Imaging setup for 3D cell culture and tissue samples. The imaging ASIC is suspended over an inverted fluorescence microscope with a glass slide in between. (c) Diagram of imaging system. (d) Bottom view of imaging setup for larger tissue samples.

6.2 3D Cell Cultures

We have demonstrated imaging with 3D breast cancer cell cultures (HER2+ HCC1569 cells) in order to characterize the ability of the imager to detect small foci of tumor containing on the order of 200 cells or fewer. These cell cultures are 40 µm thick, containing approximately 3–4 cell layers. A set of example images is shown in Fig. 6.2. A long integration time, 1 s, tabletop fluorescence microscope image is shown for reference at the top of the figure. The short integration time, 50 ms, image taken with our ASIC is shown at the bottom of the figure. The image taken with the ASIC is unfiltered and represents the raw data. Despite the lack of post-processing, all of the tumor foci identifiable in the fluorescence microscope image are clearly visible in the ASIC image. The tumor foci labeled A and B contain close to 180 and 270 cancer cells, respectively, and are detectable with close to 15 dB SNR.

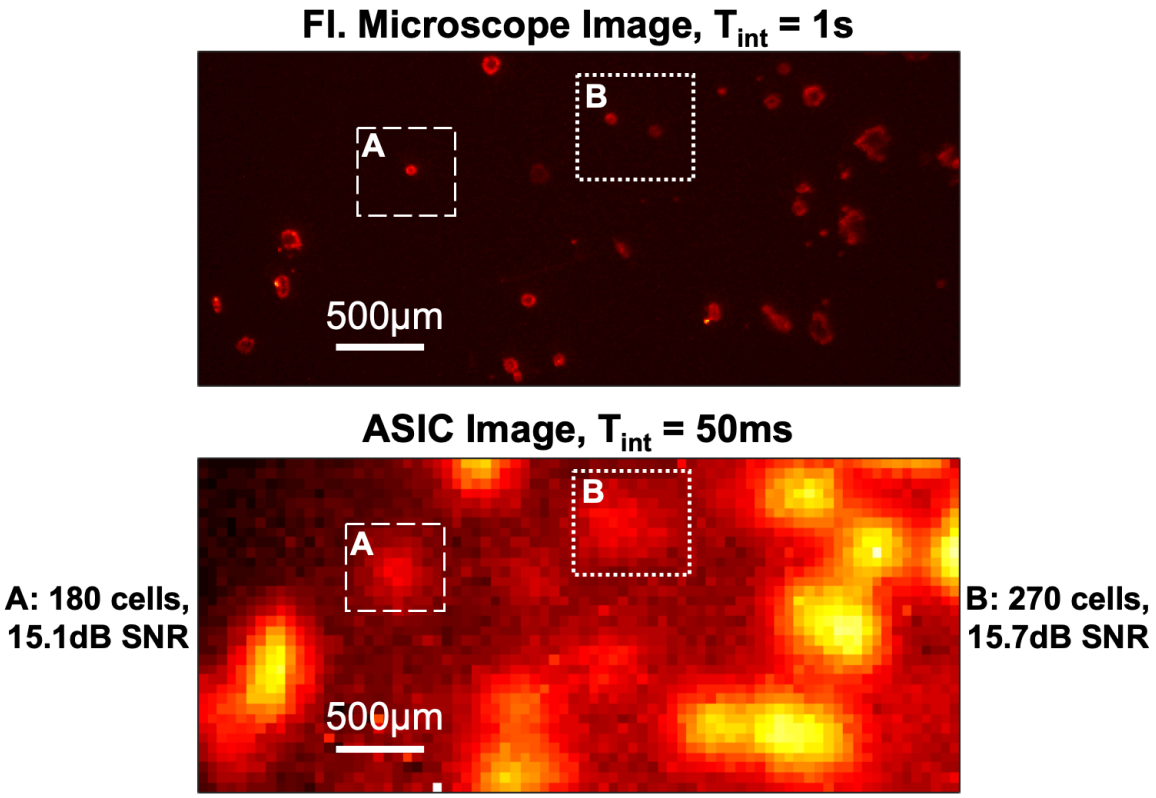

Figure 6.2: Example image of 3D breast cancer cell cultures. A 1 s tabletop fluorescence microscope image is shown (top) for reference and all cancer foci are visible in the 50 ms ASIC image (bottom).

We can calculate the expected SNR from foci containing 200 cancer cells by combining the fluorescence signal calculations in Section 3.4 with the pixel responsivity and noise performance as described in Section 4.2. The expected incident power from 200 cancer cells is 150 fW, the responsivity is $8.2\,\mathrm{V\,s^{-1}\,pW^{-1}}$, and there is an additional 55 % loss due to the presence of the gratings. For this signal level and a 50 ms integration time, the expected RMS noise is approximately 4.5 mV, and thus the overall expected SNR is 15.5 dB, very close to the measured results. The signal estimate was conservative, using pessimistic numbers for the total fluorophores per cancer cell. Even higher SNR was measured other foci containing similar numbers of cancer cells, as shown below.

In order to validate the sensor performance for a wide variety of tumor foci sizes, we have imaged over one hundred foci. The SNR versus the number of cells in a focus is plotted in Fig. 6.3. The plotted SNR represents the SNR of the pixel that received the highest signal from each focus. There is a clear trend with increasing SNR for larger foci, due to their increased signal level. However even for small foci, containing around one hundred cancer cells, the SNR is greater than 10 dB for all cases. There

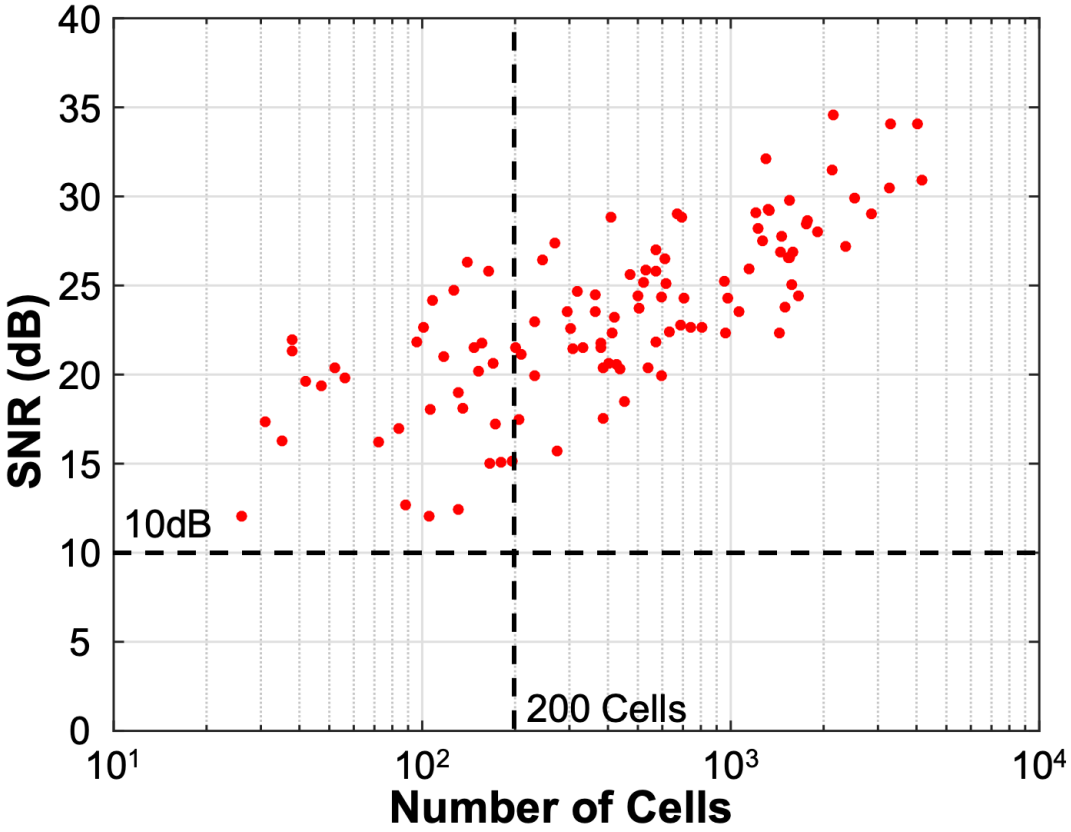

Figure 6.3: SNR for tumor foci containing less than one hundred up to thousands of cancer cells.

is a spread in the measured SNR for similar sizes due to the morphological difference between these foci (i.e. some foci may be more dense or closely packed than others), variation in the cell size, as well as variation in the binding efficiency of the antibody-fluorophore conjugate.

To improve the image quality, a variety of computation techniques can be used. As described in Section 2.1, the angle-selectivity function can be used to estimate the PSF of the imaging system. The PSF can be used to predict the ASIC images as shown in Fig. 6.4. The 1 s integration time fluorescence microscope (top left) image is used as the ground truth image and for computing the estimated ASIC image (top right). This image shows very good agreement with a filtered ASIC image (bottom right) taken with a 50 ms integration time. The filtered image is taken using the same process as the image shown on the bottom in Fig. 6.2 followed by a Gaussian filter with radius equal to the dimension of two pixels on the ASIC (110 µm) to further reduce spatial noise. The PSF of the imaging system is used along with the filtered ASIC image to compute the deconvolved ASIC image (bottom left) using the Lucy-Richardson deconvolution algorithm implemented in software. The resulting images

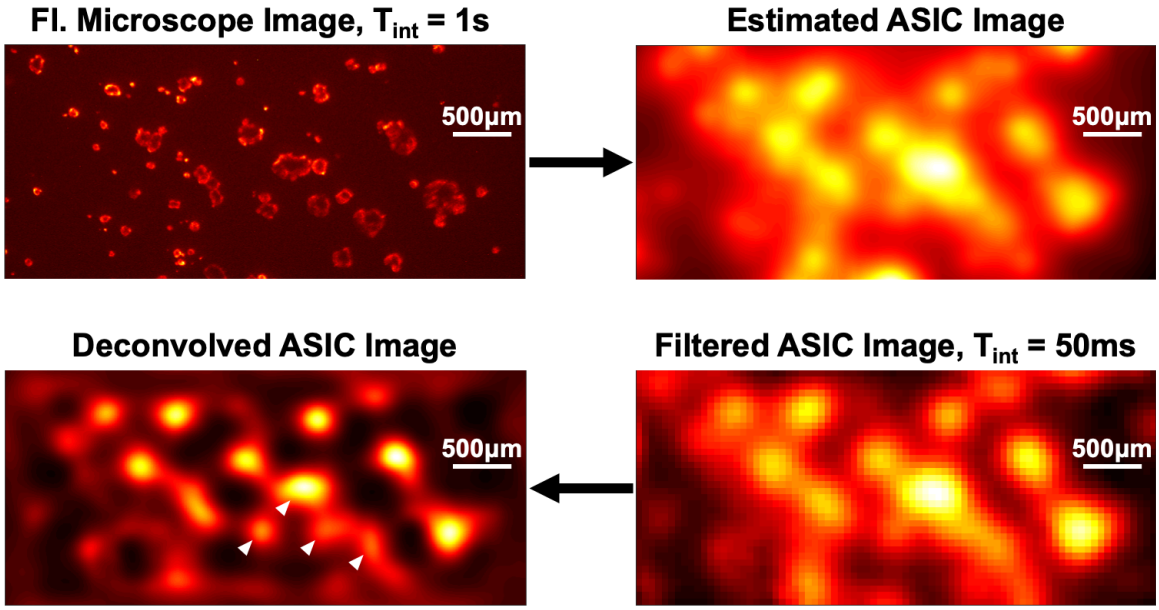

Figure 6.4: The PSF estimated using the ASIC angle-selectivity function can be used to both estimate the ASIC image from the fluorescence microscope image (top). Additionally the PSF can be used to deconvolve the images captured using the ASIC (bottom) in order to obtain a higher resolution image of the tumor position.

have significantly enhanced resolution compared to the raw chip images. Foci of cancer cells that have blurred together in the filtered image are clearly distinguishable in the deconvolved image (labeled with white arrowheads). This process can provide further information to the surgeon or be used as part of a tumor recognition algorithm to automatically detect if cancer is present based on the captured images.

6.3 Sensitivity and Specificity

Analysis was performed on captured images to more accurately represent the requirements of intraoperative tumor identification. Sensitivity and specificity were determined from the component true positive, false positive, true negative, and false negative values. In order to evaluate the sensitivity and specificity of this measurement, we use an algorithm for mapping cell clusters identified in the fluorescence microscope images to corresponding distinct regions in the custom sensor images. The two images are overlaid and cell clusters that fall within a defined capture radius around the center of a cluster identified on the custom sensor image are considered to be true positives. The capture radius consists of the sum of a constant value, the offset radius, and an intensity-based value. Details and examples of this process are explained in section 6.4.

Two modes of the algorithm are used. In the fully-automated mode, cell clusters

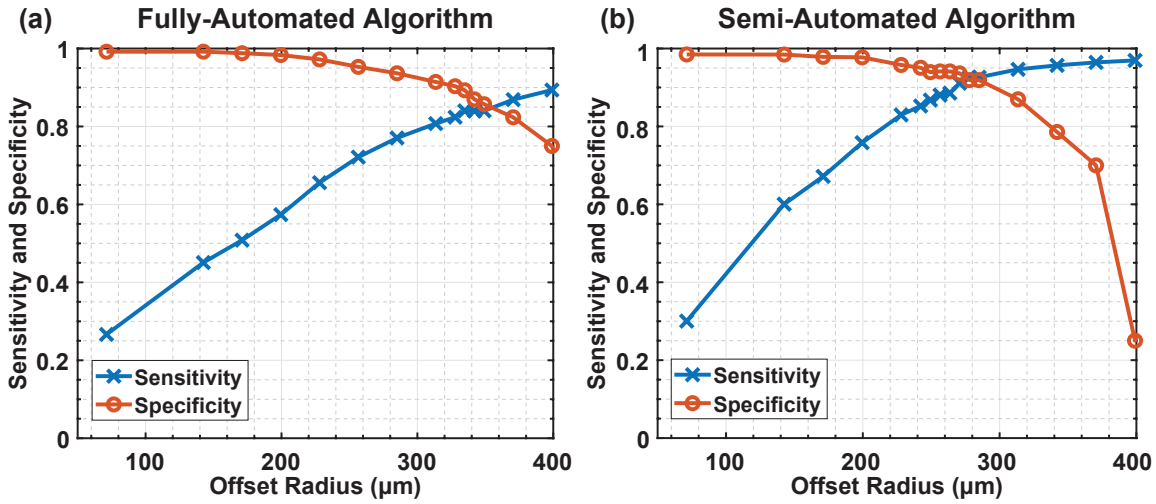

Figure 6.5: (a) Sensitivity and specificity when using the fully-automatic image recognition algorithm. For 340 µm offset radius, the sensitivity and specificity are both 85 %. (b) Sensitivity and specificity when using the semi-automatic recognition algorithm. Missed cancer cell clusters are manually identified in the custom sensor image. The sensitivity and specificity improve when using the semi-automated algorithm and for 280 µm offset radius, both sensitivity and specificity are 92 %.

are automatically detected in the custom sensor images and no user input is required. In the semi-automated mode of operation, additional cell clusters not automatically detected can be manually indicated by the user. The sensitivity and specificity for varying offset radius are plotted in Fig. 6.5 for HCC1569 cancer cell clusters. The results for the fully-automated algorithm appear in Fig. 6.5(a). The results for the semi-automated algorithm appear in Fig. 6.5(b), where additional cancer cell clusters were identified by an oncologist. If the offset radius is set too small, the algorithm does not adequately account for blurring in the image and many areas of cancer cells go undetected, leading to reduced sensitivity. If the offset is set too large, areas that are not cancerous can be misidentified, reducing the specificity. For an offset radius of 340 µm, the sensitivity and specificity are both 85 % using the fully-automated mode. Using the semi-automated mode of operation, the sensitivity and specificity can be improved to 92 % for an offset radius of 280 µm. This indicates that cancer can be reliably detected using the custom imaging system.

6.4 Cell Cluster Recognition Algorithm

In order to evaluate sensitivity and specificity, clusters of cancer cells were detected using both a fully-automated and semi-automated process in the custom sensor image and a fully-automated process in the microscope image. The positions of the

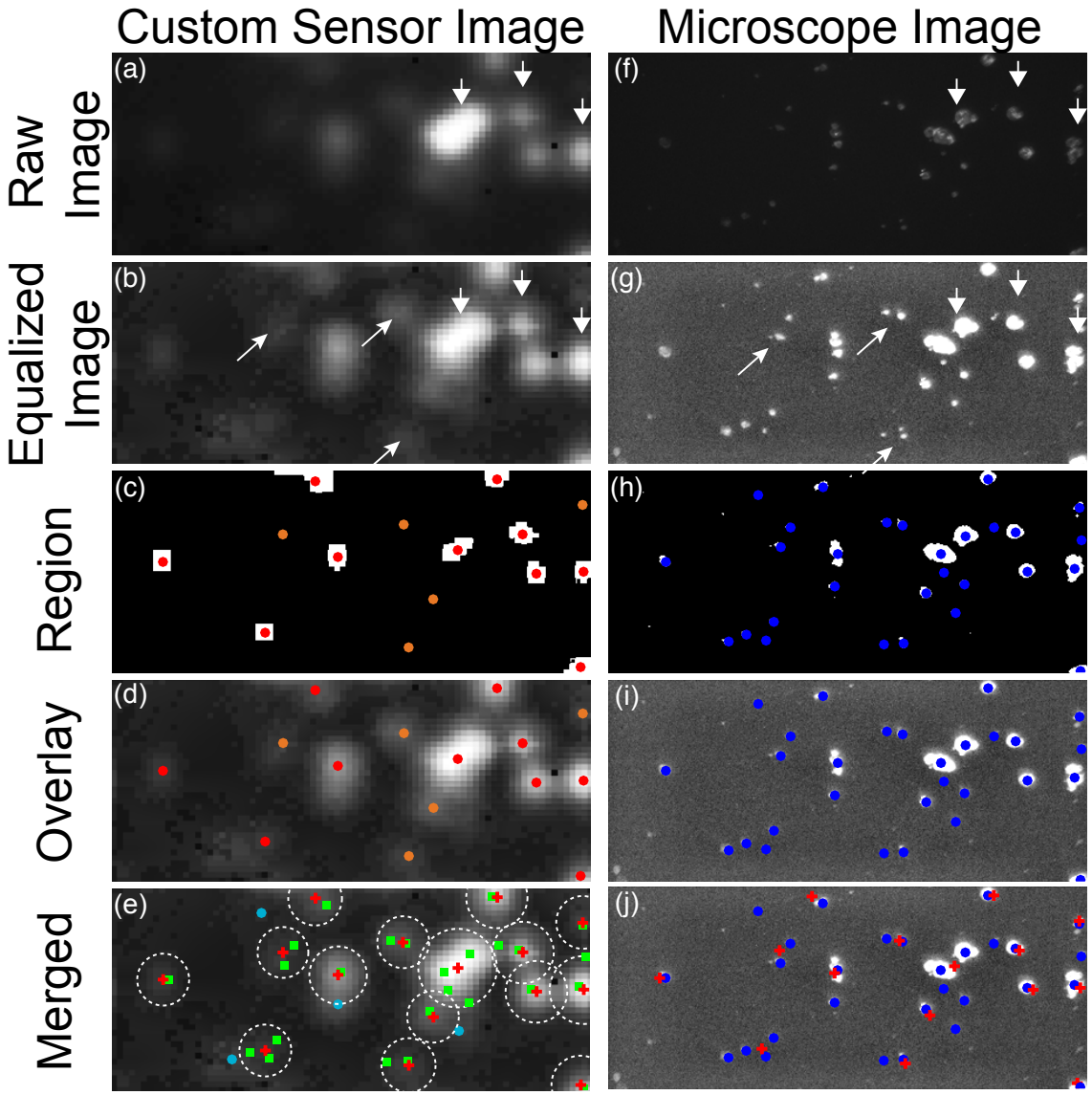

Figure 6.6: (a) Raw custom sensor image. (b) Non-linearly scaled equalized custom sensor image. (c) Regions are identified with red and orange markers. (d) Regions are overlaid on the equalized image. (e) The clusters identified in the custom sensor image appear overlaid with the clusters that are identified in the microscope image using a similar procedure to the one described in (a-d) and illustrated in (f-i). (j) An overlay of the identified clusters on the microscope image for reference.

clusters were compared to determine correctly and incorrectly detected cancer cell clusters. The detection process is illustrated in Fig. 6.6. The raw custom sensor image Fig. 6.6(a) is non-linearly scaled to make the equalized image Fig. 6.6(b). This image is thresholded and clusters are automatically identified in red when using the

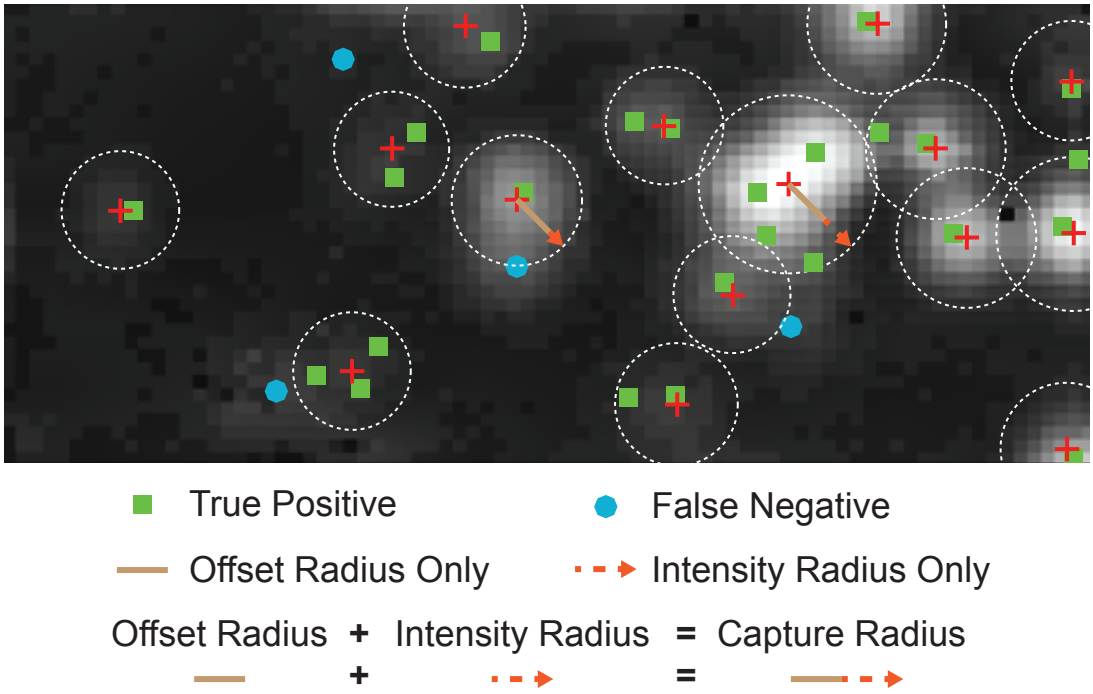

Figure 6.7: The cell clusters identified in the custom sensor image (red cross) and microscope image are compared. Clusters from the microscope image are classified as true positives (green square) if they fall within the capture radius of any cluster identified in the custom sensor image. Otherwise they are considered false negatives (light blue circle).

fully-automated mode of operation. If the semi-automated mode is used, additional clusters can be manually identified by the user. The manually added clusters are shown in orange in Fig. 6.6(c). An overlay of the identified clusters and the equalized image is shown in Fig. 6.6(d). A similar process is used to identify clusters in the microscope image as shown in Fig. 6.6(f-i), but all clusters are automatically detected. An overlay of the identified clusters in both images on top of the equalized custom sensor image is shown in Fig. 6.6(e). Areas of the custom sensor image assigned to a cluster are marked within a circle with radius equal to the capture radius as described below. Microscope clusters within the capture radius of a cluster are classified as true positives and marked with green squares. Clusters that fall outside of this radius are classified as false negatives and marked with light blue circles. A false positive corresponds to a cluster identified in the custom sensor image that has no corresponding cluster in the microscope image. A value for true negative is calculated by dividing the area outside all capture radii by the area of a circle with radius equal to the offset radius. An overlay of the identified clusters on the equalized microscope image is shown for reference in Fig. 6.6(j).

The capture radius for each cluster identified in the custom sensor image consists of the sum of a constant factor and an intensity-dependent quantity:

$$CR = OR + IR, \tag{6.1}$$

where CR is the capture radius, OR is the offset radius, and IR is the intensity radius, all with units µm. The offset radius is a constant factor and accounts for blurring in the custom sensor image. The intensity radius is given as:

$$IR = IF \cdot I, \tag{6.2}$$

where IF is the intensity factor with units $\mu m\,V^{-1}$, and I is the mean signal level of all the pixels identified to be within a cluster. Fig. 6.7 shows an example custom sensor image with the offset radius indicated as a brown line and the intensity radius indicated with a red dashed line. True positives (green squares) and false negatives (light blue circles) are also shown.

6.5 Impact of Increasing Imager-Tissue Separation

During surgery, variation in the imager-tissue separation is introduced by blood and other fluid buildup on tissue. Given that a 250 µm layer of blood is opaque, representing a reasonable upper limit of intraoperative thickness, the image sensor needs to be robust to variations of this order. We examine the effect of sample-to-imager distance variation in this section, and the effect of scattering and absorption through blood in the next section.

We varied the separation *in vitro* by increasing the distance between the imager surface and the HCC1569 breast cancer cell cultures as shown in Fig. 6.8(a). A varying number of spacers, 150 µm thickness glass coverslips, coupled together using immersion oil of approximately 100 µm thickness are used to increase the distance from the nominal 0.65 mm to 1.8 mm. One hundred 50 ms integration time images of the same area were taken with the custom image sensor and averaged together to increase SNR and accurately evaluate the degradation in spatial resolution. The custom sensor images with increasing distance are shown in Fig. 6.8(b1-g1). To more easily visualize the change in spatial resolution, the images are normalized in Fig. 6.8(b2-g2), with each image scaled relative to its own maximum pixel. The reference 1s microscope image is shown in Fig. 6.8(h).

The two primary effects of increased imager-tissue separation are (1) a reduction in spatial resolution and (2) a decrease in SNR. The reduced resolution is primarily visible in Fig. 6.8(b2-g2) where two distinct cancer cell spots gradually blur together to form one larger spot as the distance is increased. Sub-millimeter resolution is achieved even at a large 1.8 mm separation and the SNR is only degraded by a gradual $6\,dB\,mm^{-1}$ as imaging distance is increased. With an expected intraoperative distance variation of 250 µm, the expected SNR variation is less than 1.5 dB.

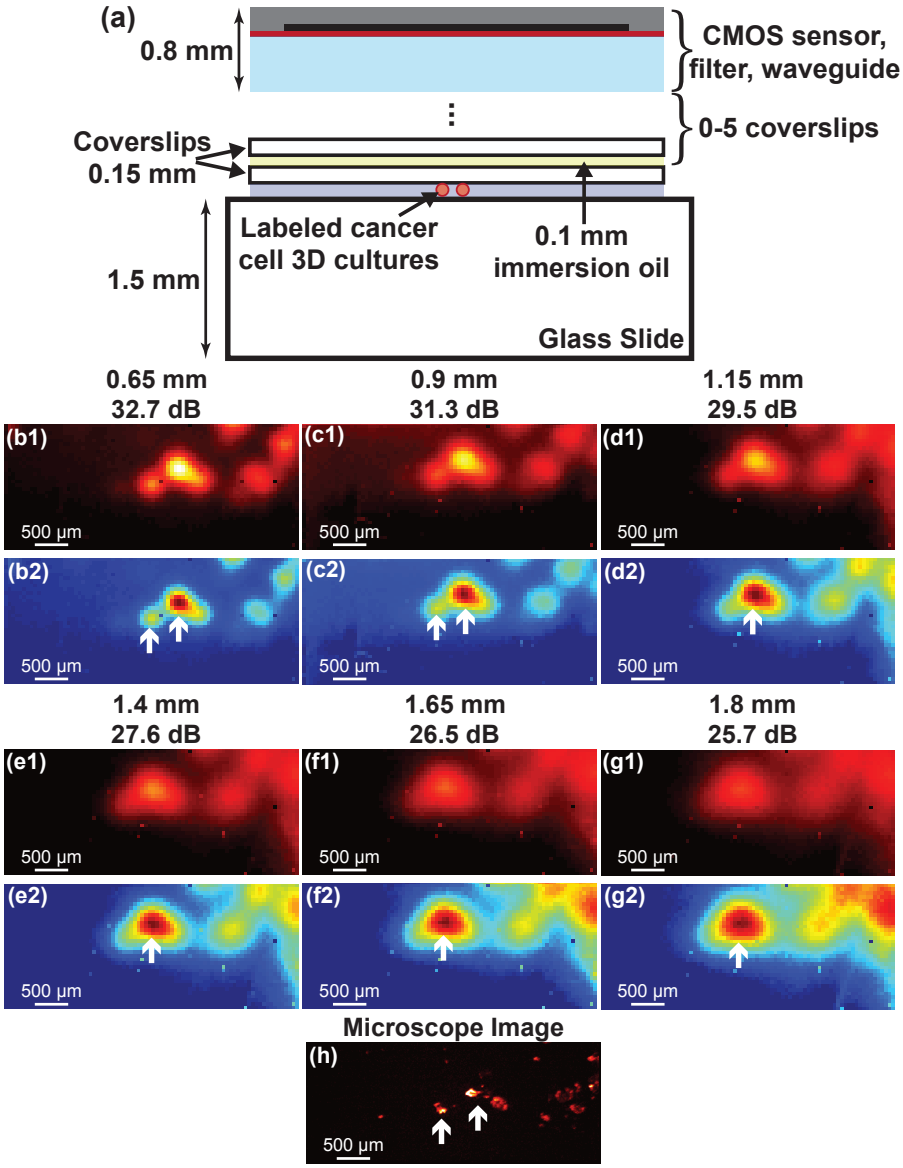

Figure 6.8: (a) Test setup for measuring distance variation. (b1-g1) One hundred averaged 50 ms custom sensor images taken at increasing distance from 0.65 mm to 1.8 mm in 0.25 mm intervals. The maximum SNR in each image is noted. (b2-g2) Normalized versions of the images to more clearly visualize the degradation in imaging resolution with increasing distance. (h) 1 s integration time microscope image for reference.

6.6 Impact of Blood Scattering and Absorption

While tumor cavities are irrigated continuously during surgical procedures, a residual thin layer of diluted blood is common. Without this irrigation, blood in

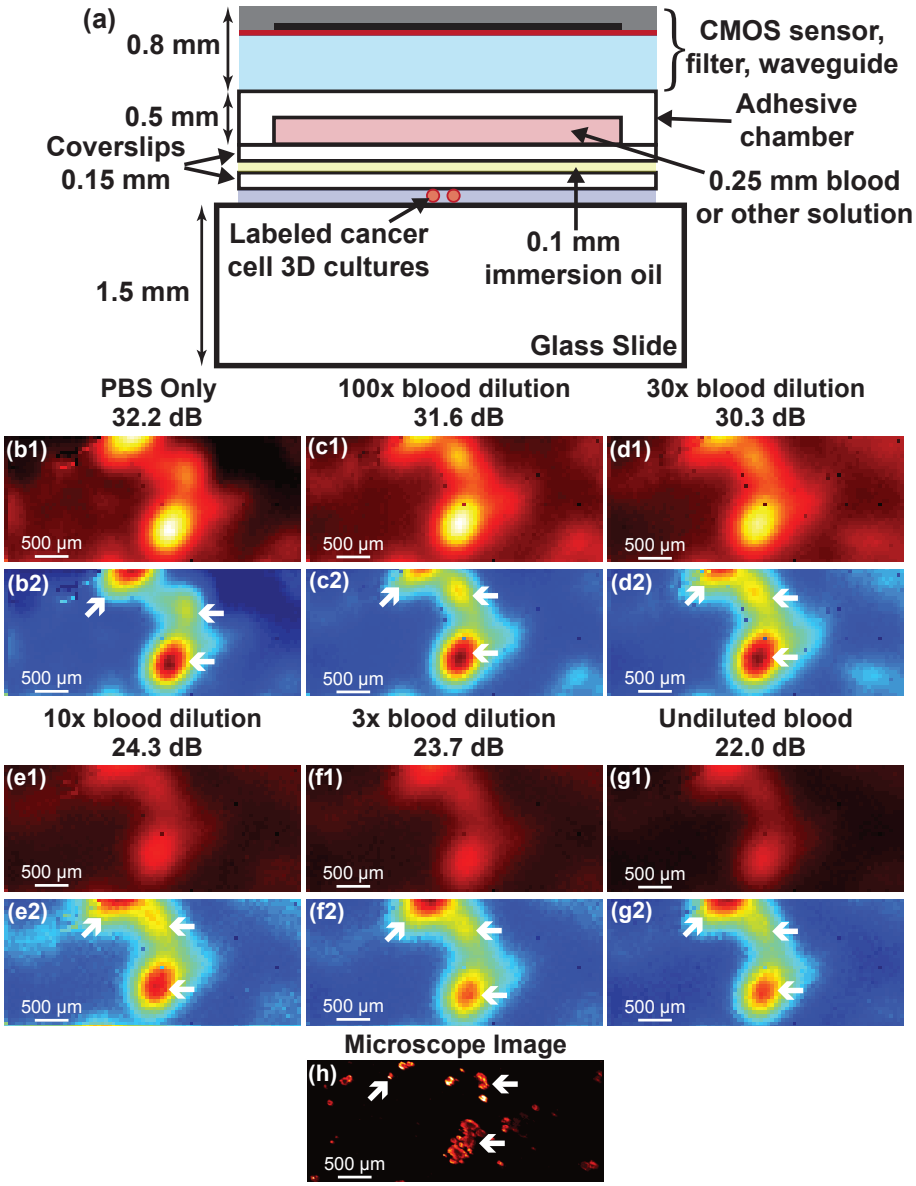

Figure 6.9: (a) Test setup for measuring the effect of different dilutions of blood. (b1-g1) One hundred averaged 50 ms custom sensor images taken for a pure PBS (clear) solution, 100X, 30X, 10X, and 3X dilutions of blood in PBS, as well as undiluted blood. The maximum SNR in each image is noted. (b2-g2) The images are normalized in order to more clearly visualize the increased noise for solutions containing more blood. (h) 1 s integration time microscope image for reference.

the tumor cavity would obscure the surgeons' view, hampering their ability to resect tissue. In order to evaluate the effect of a layer of blood with varying dilutions, we placed an adhesive chamber on top of a coverslip and filled the chamber with different

dilutions of blood in phosphate-buffered saline (PBS). The liquid layer in the chamber is 250 µm thickness. The chamber was then placed in between our custom sensor and coupled to the slide holding HCC1569 breast cancer cell cultures using immersion oil (Fig. 6.9(a)). The total cancer cell to image sensor distance is approximately 1.25 mm. One hundred 50 ms integration time images were taken and averaged for each blood dilution in order to evaluate the effect of each dilution on the resolution of the image. The images are shown in Fig. 6.9(b1-g1) when filling the chamber with pure PBS, 100X, 30X, 10X, and 3X dilutions of blood in PBS, and undiluted blood, respectively. To more easily visualize the images, they are normalized in Fig. 6.9(b2-g2), with each image scaled relative to its own maximum pixel. The 1 s integration time fluorescence microscope image is shown in Fig. 6.9(h) for reference.

There is no noticeable reduction in spatial resolution as the blood concentration is increased, but there is a reduction in the SNR. The blood scatters the emission light isotropically, essentially trading signal for background (reducing SNR). Due to the presence of the angle-selective gratings (ASGs), the majority of the scattered light is rejected by the image sensor and spatial resolution remains unaffected. While the SNR reduction is significant for high blood concentrations, up to 10 dB for a 250 µm layer of undiluted blood, with proper tumor cavity irrigation, dilutions on the order of 30-100X are common, and the SNR reduction will be limited to less than 2 dB.

6.7 Human HER2+ Breast Cancer Tissue Imaging

We demonstrate that tumor borders are clearly detected and tumor distinguished from normal tissue by imaging human HER2+ cancer tissue from a breast cancer patient. Slices from frozen tissue are mounted on a glass slide and imaged simultaneously using a fluorescence microscope and our custom sensor. The 75 ms integration time microscope and custom sensor images are shown in Fig. 6.10(a) and Fig. 6.10(b), respectively. In order to reduce noise, both microscope and custom sensor images are filtered with a 2D Gaussian filter with standard deviation equal to two pixels on the custom sensor, or 110 µm. The filtered versions are shown in in Fig. 6.10(c) and Fig. 6.10(d), respectively. A long integration time 5 s integration time microscope image is shown in Fig. 6.10(e) for reference. The brightest areas correspond to cancer tissue, the darkest areas to background from the slide, and the intermediate brightness areas to healthy tissue. The tumor margin is confirmed with immunohistochemistry and hematoxylin and eosin (H&E) stain images as shown in Fig. 6.10(f1) and Fig. 6.10(g1) of the areas indicated in the two labeled boxes in Fig. 6.10(e). Additional higher magnification fluorescence images (red) overlaid on DAPI images (blue) are shown in Fig. 6.10(f2) and Fig. 6.10(g2) for reference.

The tumor margin is clearly visible in the custom sensor images, with improved SNR after filtering. The unfiltered microscope image has significant noise, but after filtering has similar resolution and noise to the filtered image of the custom sensor. While the long integration time microscope image shows the cancer and healthy tissue

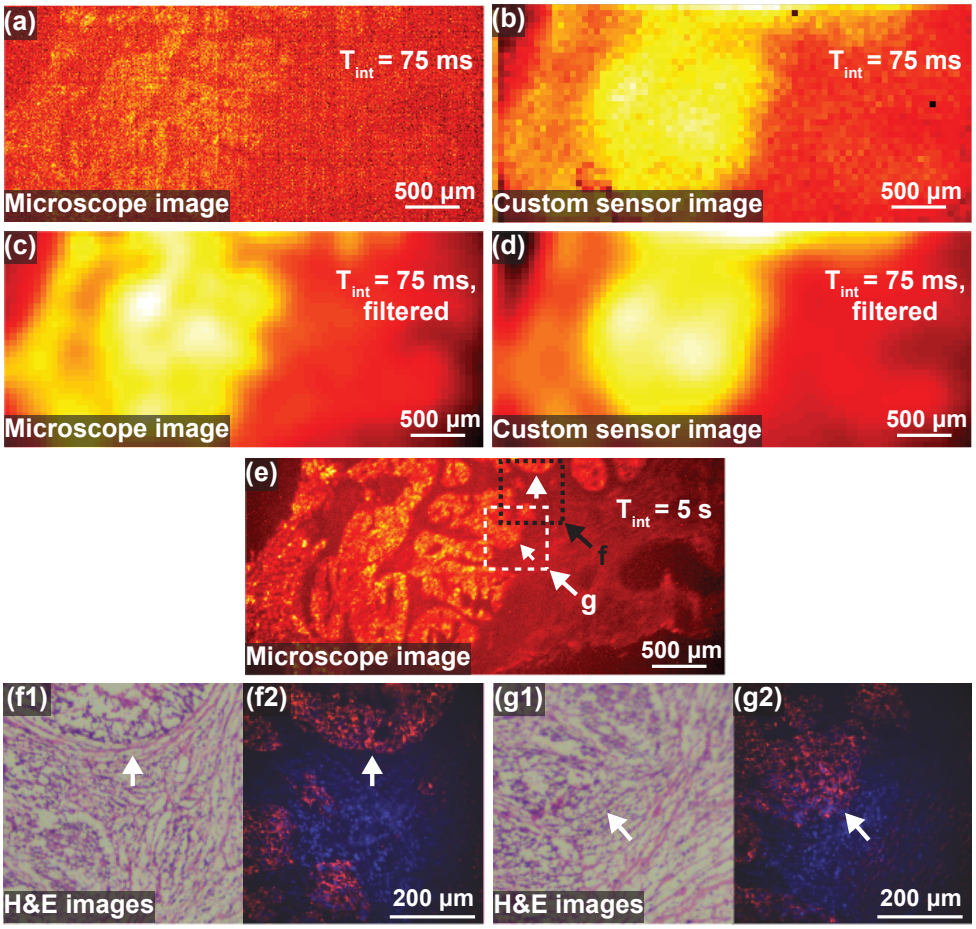

Figure 6.10: Images of human HER2+ breast cancer tissue slices. (a) Raw 75 ms fluorescence microscope image. (b) Raw 75 ms custom sensor image. (c) Fluorescence microscope image filtered with 2D Gaussian filter with standard deviation 110 µm. (d) Custom image filtered with 2D Gaussian filter with standard deviation 110 µm. (e) 5 s integration time fluorescence microscope image for reference. (f1,g1) Two regions, labeled f and g in (e), were examined using hematoxylin and eosin (H&E) as shown in order to confirm tumor margin. (f2,g2) Higher magnification fluorescence images (red) are shown overlaid on DAPI stain images (blue) of the same regions.

in higher resolution, this is not possible with short integration times due to excessive noise. For the same 75 ms integration time, our custom sensor detects tumor margin with similar performance to the fluorescence microscope, but maintains a significantly smaller form factor, allowing it to be used intraoperatively.

Another example image of the human HER2+ breast tumor is shown in Fig. 6.11. Fig. 6.11(a) shows a 75 ms integration time image taken using the image sensor with ASGs and a 15 µm thick amorphous silicon absorption filter. The corresponding microscope image taken with a 5 s integration time is shown for reference in Fig. 6.11(b),

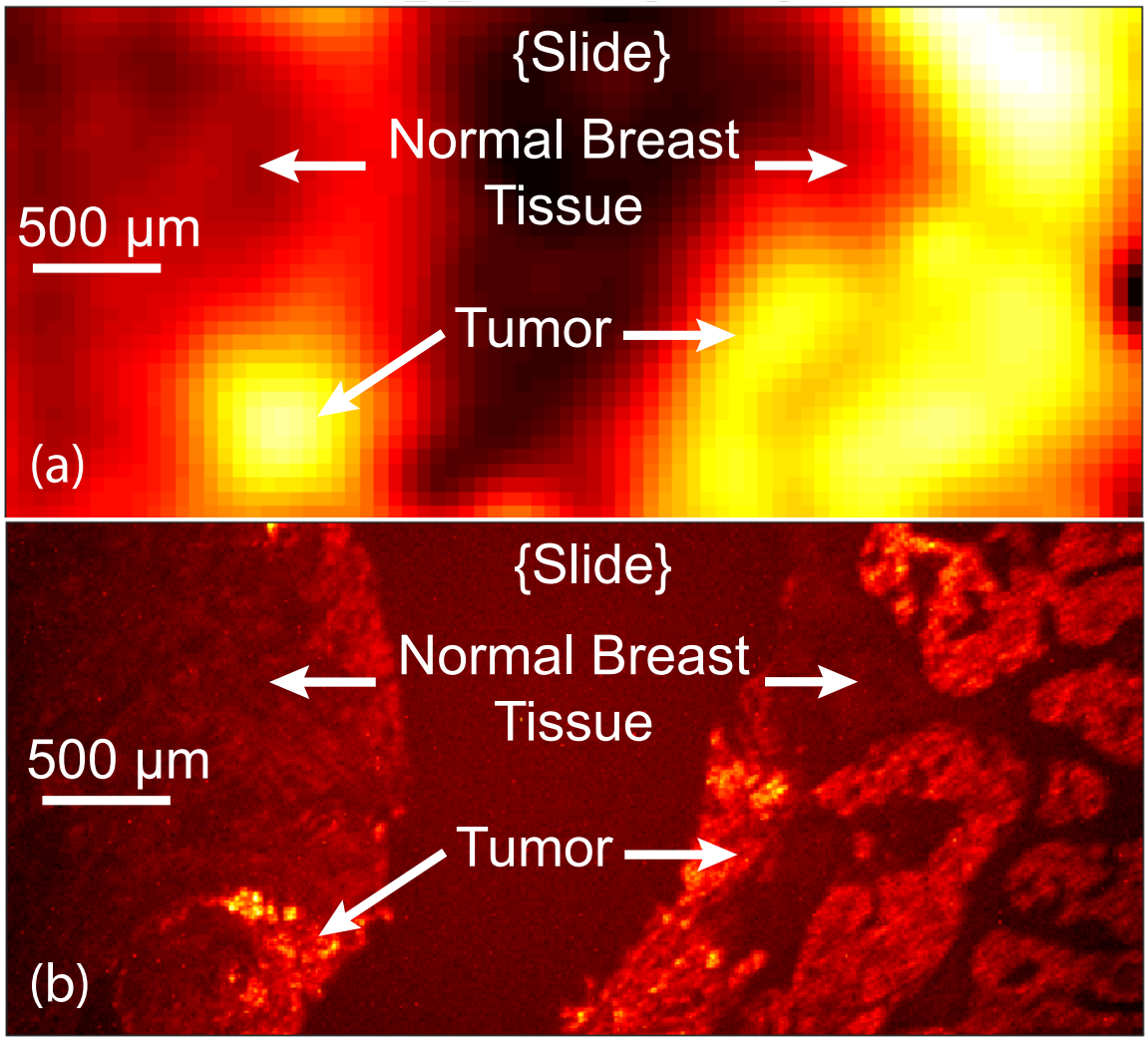

Figure 6.11: Images of human HER2+ breast tissue. (a) 75 ms image taken with the custom sensor. (b) 5 s fluorescence microscope image.

but this microscope image could not have been obtained in an operating room setting. Tumor infiltrating the normal breast tissue is seen as the brighter areas. The area labeled Slide is the background from the glass mounting slide, corresponding to filter bleed through and nonspecific binding. The cancer tissue is easily located and clearly distinguishable from both healthy tissue and the slide background with an integration time of only 75 ms in the custom sensor image. This allows our imaging system to be used intraoperatively and in real-time.

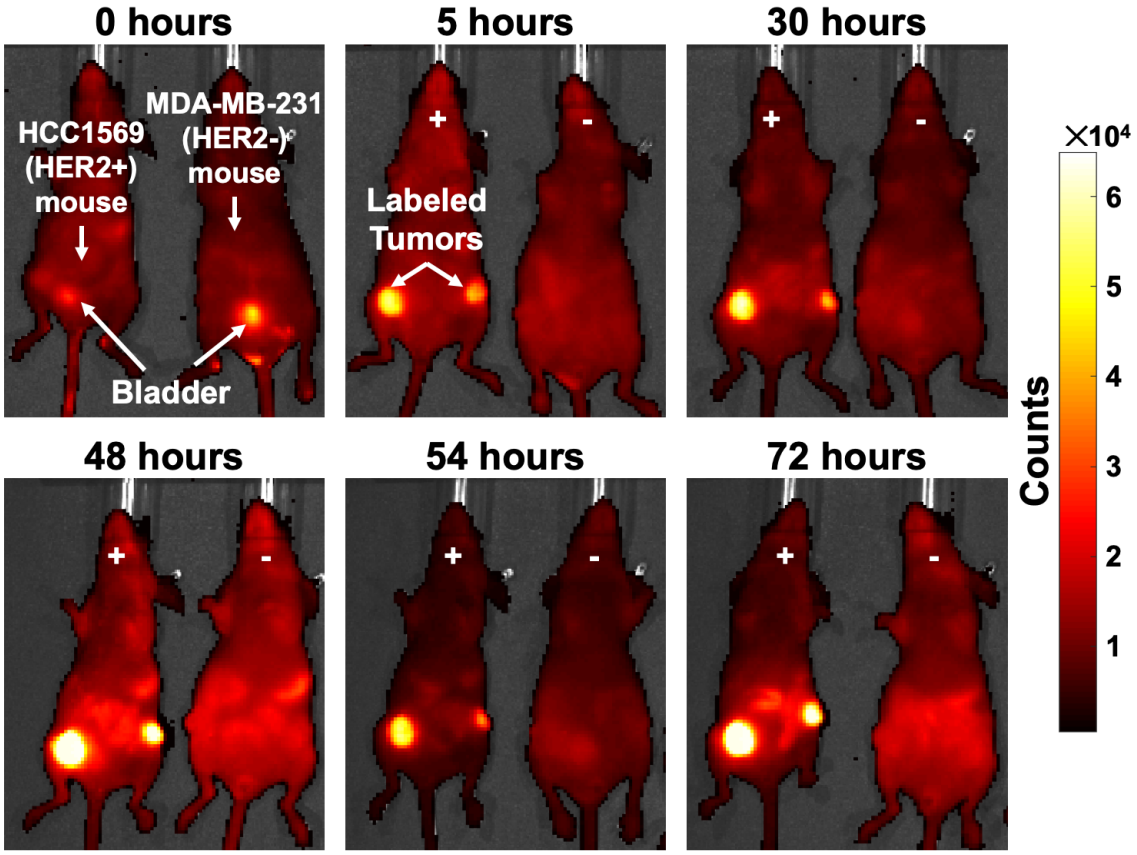

Figure 6.12: Images of mice injected with Trastuzumab IR700DX fluorescent probe over 72 hours after tail vein injection. Images are taken with an IVIS Spectrum live animal imaging system. Fluorescence emission is visible in the mice implanted with HER2+ breast cancer tissue after only 5 hours and the signal remains high through 72 hours.

6.8 Mouse Tumor Imaging

We also performed imaging on mouse tumor labeled *in vivo* using an antibody-fluorophore conjugate (Trastuzumab-IR700DX). HER2+ (HCC1569) and HER2- (MDA-MB-231) tumor cells were injected into mammary fat pads on both sides of four groups of mice and allowed to grow until approximately 1 cm in size. The mice were initially injected with 0.25, 0.5, 1, and 2.5 million cells for groups 1-4, respectively. A systemic tail vein injection of Trastuzumab-IR700DX was performed at this point and the mice were imaged over the subsequent 72 hours. Trastuzumab specifically targets HER2+ cancer, so mice bearing HER2- MDA-MB-231 tumors are the negative control. Fig. 6.12 shows the live animal images of group 1 mice at 0 hours, 5 hours, 30 hours, 48 hours, 54 hours, and 72 hours taken using an IVIS Spectrum live animal imaging system (Perkin Elmer). The fluorescence images are overlaid on

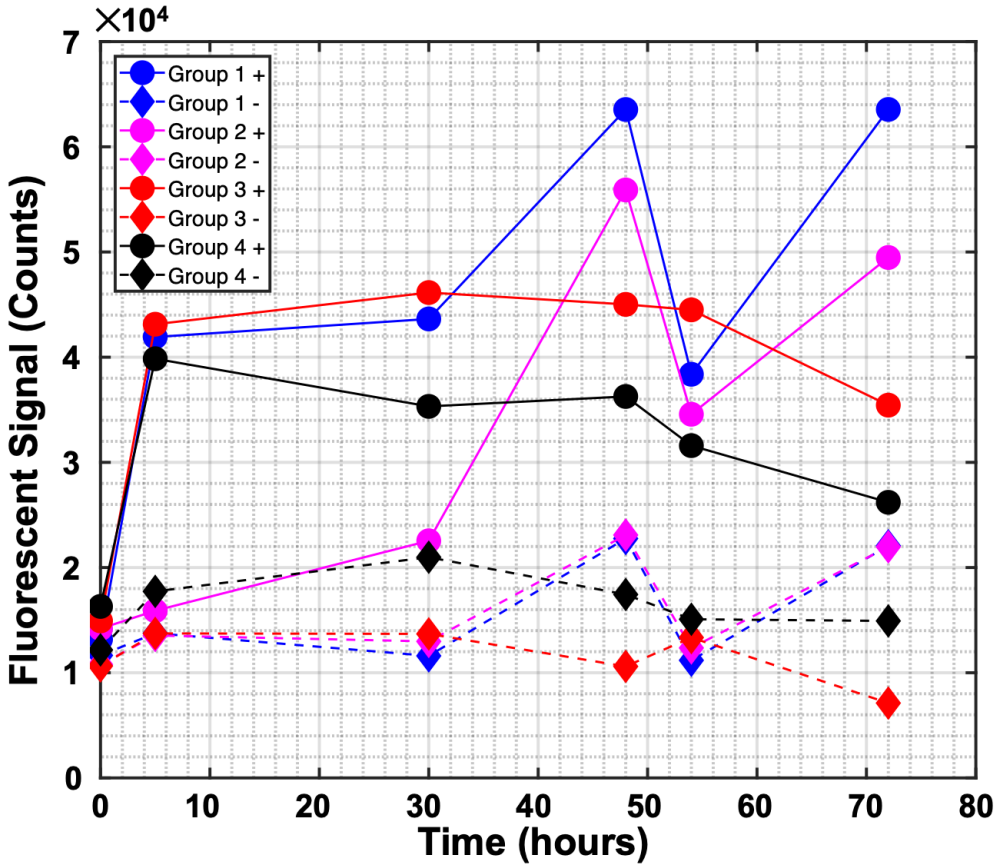

Figure 6.13: Measured intensity of HER2+ HCC1569 tumors (circles) and HER2- MDA-MB-231 tumors (diamonds) labeled with Trastuzumab IR700DX fluorescent probe. The intensity for four groups of mice, initially injected with 0.25, 0.5, 1, and 2.5 million cells for groups 1-4, respectively, are shown. The probe binds preferentially to the HER2+ cancer and the binding efficiency remains high over 72 hours.

photographs. The HCC1569 implanted mouse appears on the left side in each image and the MDA-MB-231 implanted mouse appears on the right. Trastuzumb-IR700DX binding is visible after 5 hours in the HCC1569 implanted mouse. The tumors are indistinguishable from background non-specific antibody binding for the MDA-MB-231 implanted mouse, indicating that the fluorescent probe correctly targets HER2+ breast cancer only.

The measured signal over 72 hours for a single tumor on each mouse for all four groups is shown in Fig. 6.13. The tumor signal generally increases rapidly over the first 5 hours and remains elevated through 72 hours. The signal from the HCC1569 tumor is 2.9X, 2.3X, 5.0X, and 1.8X larger than the MDA-MB-231 at 72 hours for groups 1-4, respectively, for an overall ratio of 3.0±1.2. However, the specific morphology of the tumor and the variable placement of the mice on the scanner at each time point affect the live animal measurement and cause the fluctuations visible over time in Fig. 6.13.

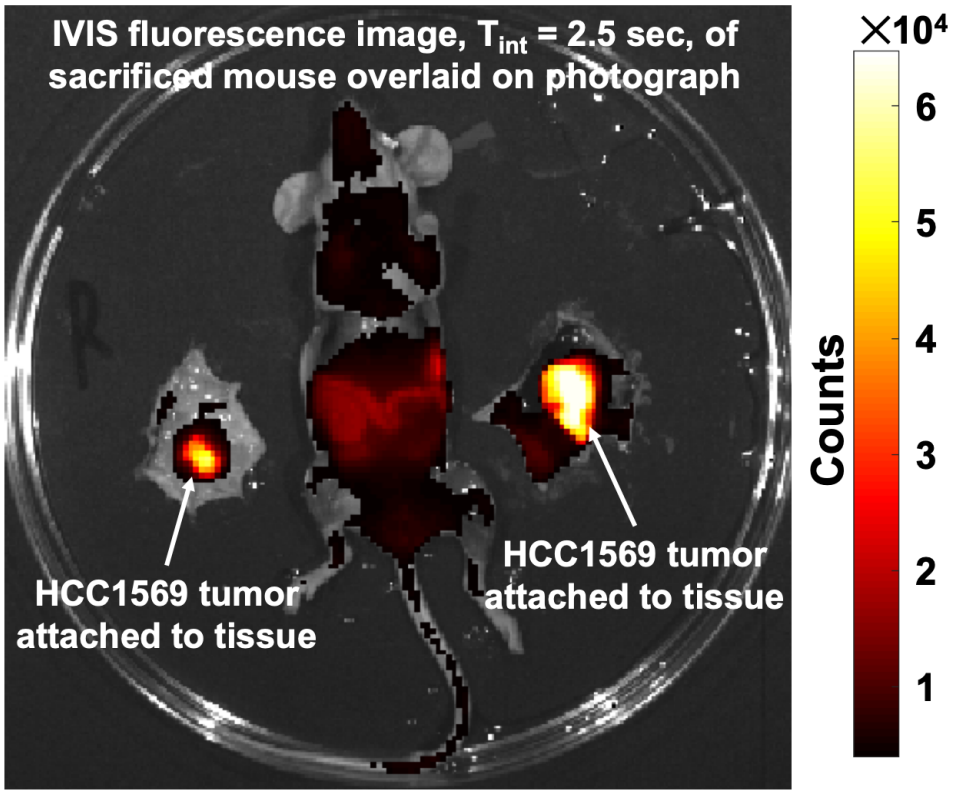

Figure 6.14: Overlaid IVIS fluorescence image and photograph of a mouse with sections removed. Each section contains tumor attached to the skin and surrounding healthy breast tissue.

Scattering and absorption in the skin also reduce the received signal. For these reasons, the intensity was measured after excision as well. At 72 hours we performed resections on the mice in order to remove the tumors, as shown in Fig. 6.14. An example HCC1569 implanted mouse is shown. Tumors were excised from the healthy tissue for each mouse and the excised tumor intensity was measured again using the IVIS. The intensity for all eight mice tumors is shown in Fig. 6.15(a). After excision, the HCC1569 tumor is 3.2X, 5.1X, 3.8X, and 3.2X brighter than the MDA-MB-231 for groups 1-4, respectively, for an overall ratio of 3.8±0.8. The number of initially injected cancer cells does not appear to noticeably affect measured intensity. These results indicate that the IR700DX probe effectively binds to HER2+ (HCC1569) breast cancer tissue and is clearly distinguishable from both HER2- (MDA-MB-231) cancer tissue and healthy tissue.

In order to evaluate the performance of our custom contact sensor system, imaging was performed on the resected mice tumor as well as healthy (non-cancer or normal) tissue. A 7.5 mW excitation laser light source at 633 nm was used to illuminate

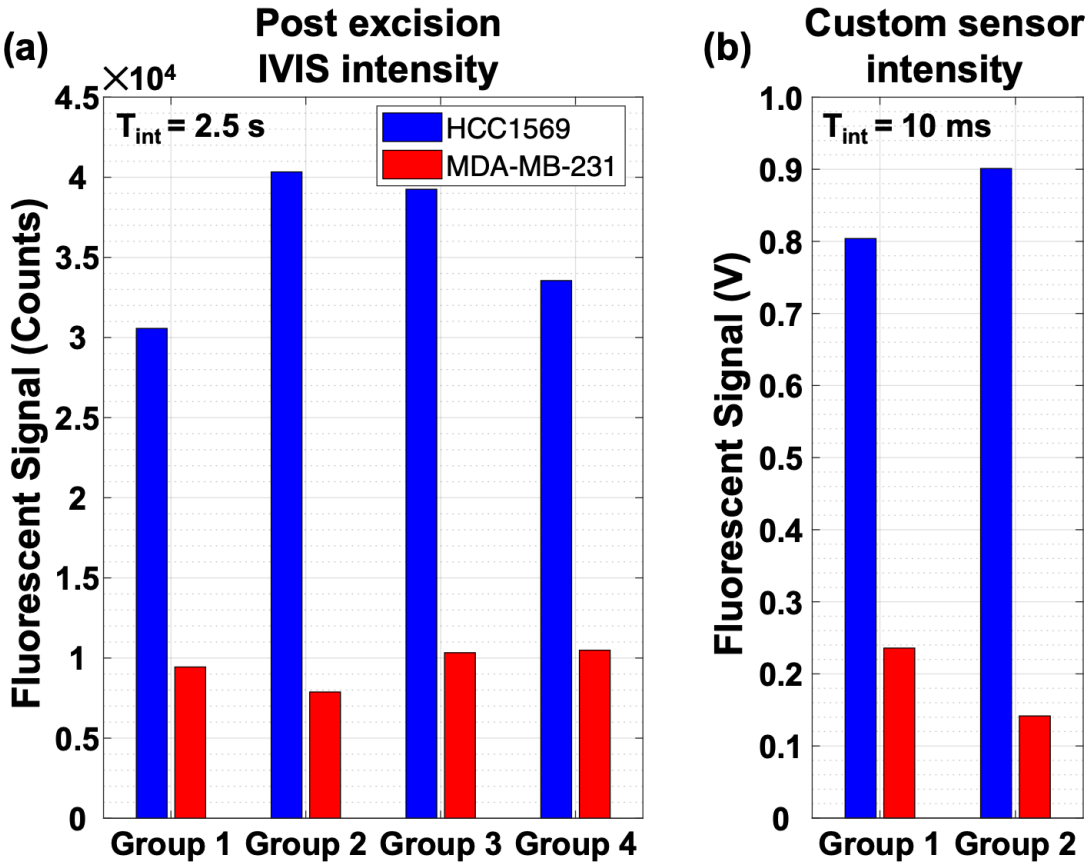

Figure 6.15: (a) Intensity of HCC1569 and MDA-MB-231 tumors for groups 1-4 after excision measured with the IVIS. (b) Intensity for the same tumors in group 1 and group 2 measured with the custom fluorescence contact imager using a 10 ms integration time.

the tissue. The measured intensity signal from the excised tumors for group 1 and group 2 mice is shown in Fig. 6.15(b). The intensity of the HER2+ (HCC1569) tumor is 3.4X and 6.4X larger than the intensity of the HER2- (MDA-MB-231) tumor for groups 1 and 2, respectively. These ratios are similar to, but slightly larger than, the intensity ratios measured using the IVIS imaging system.

To demonstrate distinguishing specifically labeled tumor cells from the negative control, we placed one of the excised HCC1569 tumors adjacent to one of the excised MDA-MB-231 tumors and imaged them using the IVIS and the custom image sensor. The IVIS image is shown in Fig. 6.16(a). The bright yellow areas correspond to HCC1569 tumor and the darker red areas correspond to MDA-MB-231 tumor. The intensity at two points is marked in the image and the HCC1569 tumor is approximately 3X brighter than the MDA-MB-231 tumor. The indicated subsection of the sample was imaged with the custom sensor using a 35 ms integration time and the resulting image is shown in Fig. 6.16(b). In this image, the HCC1569 region appears

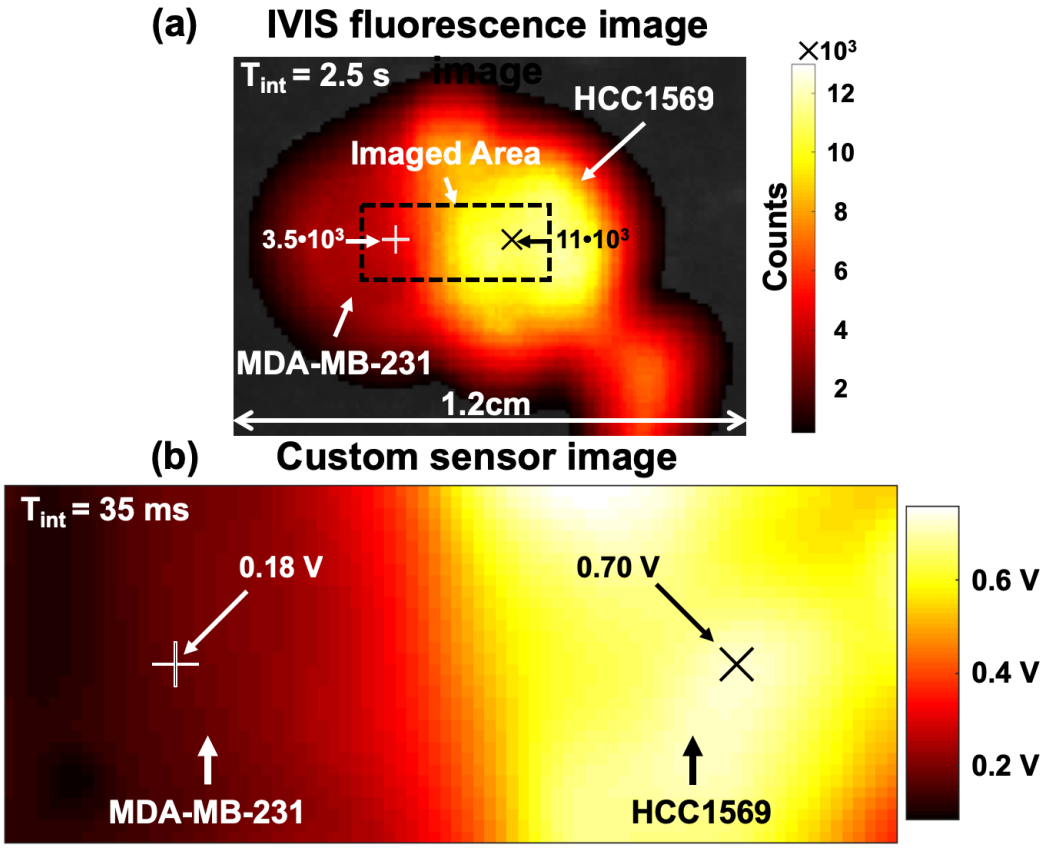

Figure 6.16: (a) IVIS fluorescence image of adjacent HCC1569 and MDA-MB-231 cancer tumors. The HCC1569 appears in bright yellow and the MDA-MB-231 in dark red. The fluorescent probe preferentially binds to the HER2+ HCC1569 cancer. (b) An image of the area indicated in the dashed box in (a) taken using the custom imager. The two types of cancer are clearly distinguishable with only a 35 ms integration time

3.9X brighter than the MDA-MB-231 tumor, again a slightly higher ratio than that found using the IVIS imager. Contact imagers only image the surface tissue of the sample, unlike the IVIS that integrates signal from its entire volume, and this can account for the improved contrast obtained with the custom sensor.

6.9 Microscopic Residual Mouse Tumor

The primary purpose of our custom sensor is to detect residual cancer tissue after removing the gross section of tumor. In order to demonstrate this, we have also performed imaging of residual tumor tissue. We performed resections on the excised sections of mouse tumor and healthy tissue described previously in order to remove

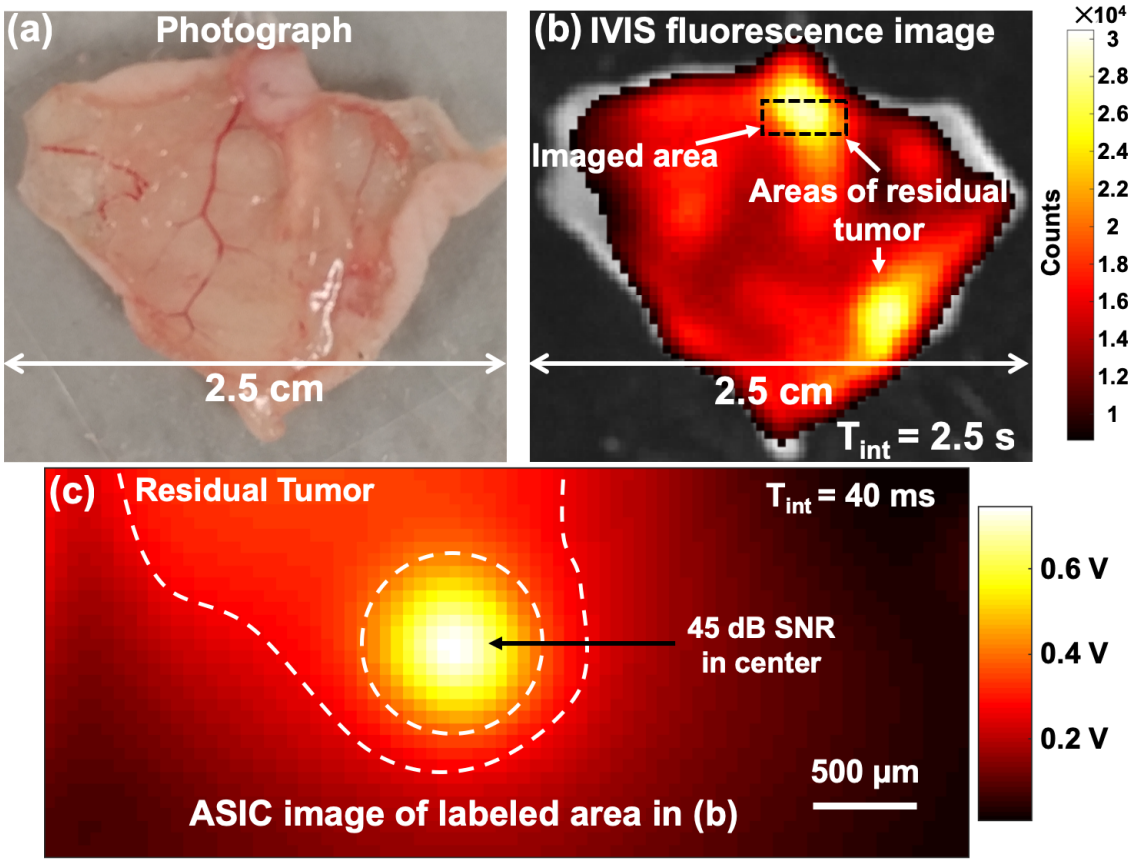

Figure 6.17: (a) Photograph of remaining tissue and skin after a large (∼1 cm) mouse tumor was removed. No tumor is visible to the naked eye. (b) Image of the same tissue taken with an IVIS fluorescence imager showing two clear areas of residual cancer. (c) Image of the area outlined in (b) taken with the ASIC showing the presence of ∼500 µm diameter section of tumor remaining on the tissue.

all of the tumor that was visible to the naked eye. Fig. 6.17(a) shows a section of mouse tissue and skin after a breast tumor (with diameter approximately 1 cm) was removed. No tumor is visible and it appears to be normal tissue. However, as shown in Fig. 6.17(b), an image taken using the IVIS live animal fluorescence imager, two areas of residual tumor remain on the tissue. We imaged the outlined area in Fig. 6.17(b) using the ASIC and the resulting image is shown in Fig. 6.17(c). A clear area of residual tumor is visible and outlined in white. A focus of tumor with diameter close to 500 µm is detected with a very high 45 dB SNR and an integration time of only 40 ms. This residual tumor could not have been detected without fluorescence imaging by eye or touch (the methods currently available to surgeons) after the removal of the large section of tumor.

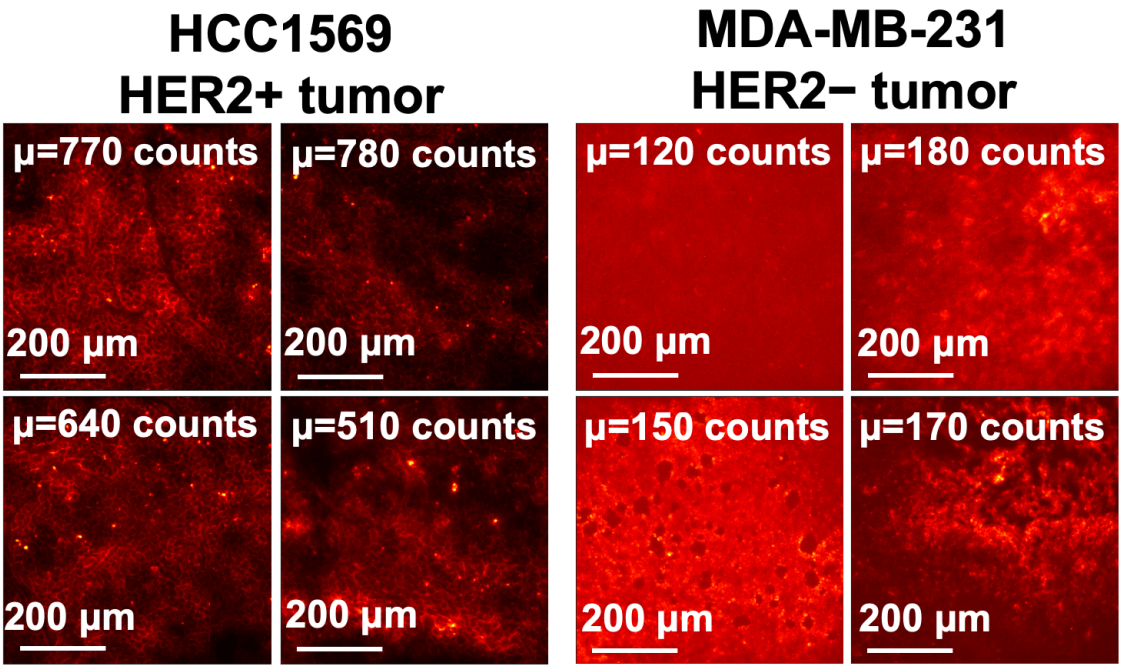

Figure 6.18: 300 ms integration time fluorescence microscope images of 14 µm sections of excised tumor. Each slice is taken from a different mouse injected with the Trastuzumab-IR700DX fluorescent probe. Images are normalized and mean photon counts per pixel are indicated for each image. The HER2+ breast cancer is a factor 4.5±1.1 times brighter than the HER2- breast cancer, indicating that the fluorescent probe correctly binds to HER2+ tumor.

6.10 Slide-Mounted Mouse Tumor Sections

We have also characterized and images sections of the mouse tumor described in the previous two sections. Using a fluorescence microscope, HER2+ tumors were measured to be 4.5±1.1 times brighter than HER2- tumors post excision as shown in Fig. 6.18. We also performed imaging of tumor sections with the custom imager and conventional fluorescence microscope and the resulting images are shown in Fig. 6.19. The defining tumor features that appear in the microscope image are clearly visible in the custom sensor image. Fig. 6.20 contains images of overlapping sections of HER2+ tumor and HER2- tumor. HER2+ tumor was readily distinguished from HER2- tumor using the custom fluorescence contact imager with integration times of only 70 ms or less, suitable for real-time imaging. Features are detectable with

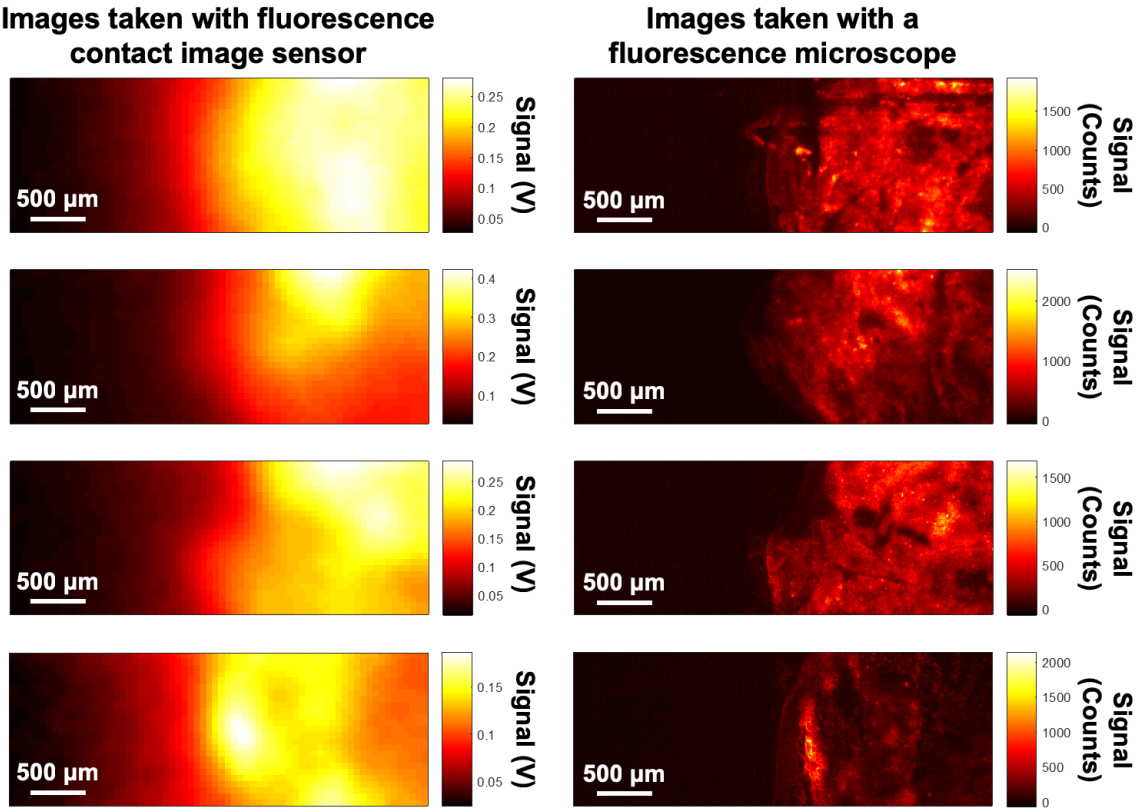

Figure 6.19: Images of four 14 µm thickness slices of excised mouse tumor tissue. Each slice comes from a different mouse bearing HCC1569, HER2+ tumors. The images on the left are taken with the custom fluorescence contact image sensor. The corresponding images on the right are taken with a fluorescence microscope for reference. All images are taken using a 70 ms integration time.

sub-millimeter resolution and signal-to-noise ratios of 33 dB. The sensor's ability to rapidly locate and distinguish cancer tissue as well as its small size-scale allow it to be used as an intraoperative probe for detection of residual tumor in the resection cavity.

6.11 Materials and Methods

This section describes the way the different biological samples used for testing the custom sensor were prepared. Additionally, we describe the details of the equipment used in the test setup.

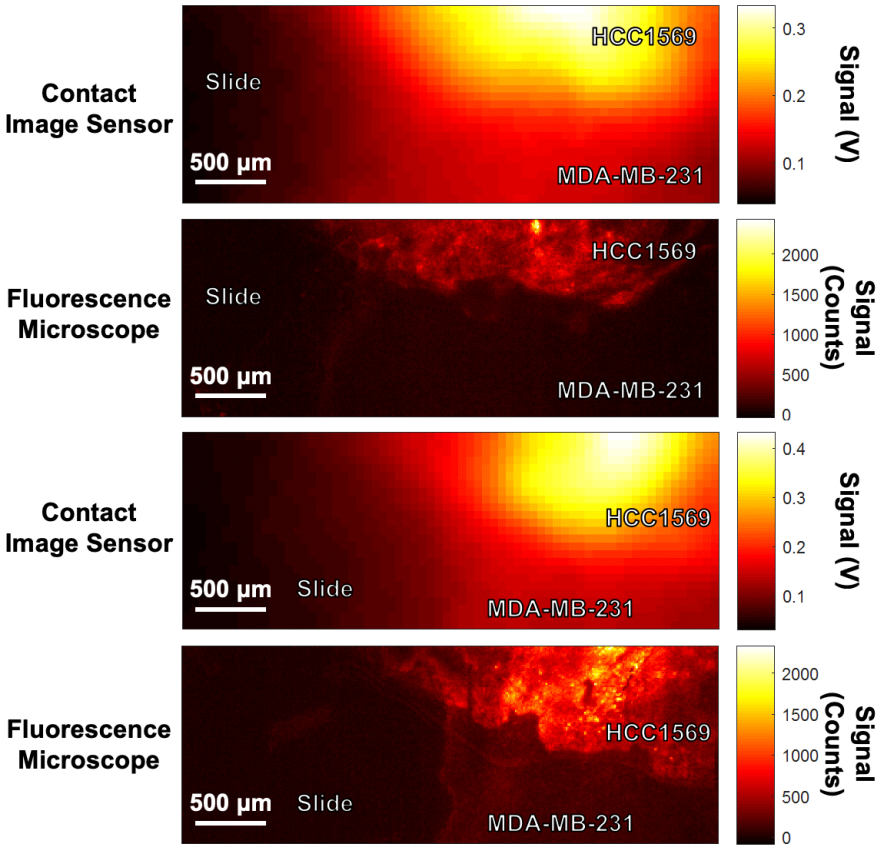

Figure 6.20: Images of overlapped 14 µm sections of HCC1569 (HER2+) tumor and MDA-MB-231 (HER2-) tumor. Images are taken with the custom fluorescence contact image sensor and a fluorescence microscope with 70 ms integration times. Both types of cancer are clearly distinguishable from each other and the background from the glass mounting slide using the custom contact image sensor. The signal-to-noise ratio is 33 dB or greater for the HCC1569 tumor.

6.11.1 3D Cell Culture Models

For characterization of the imager, three-dimensional (3D) cell culture models of breast cancer were used to generate cell clusters of varying size. Breast cell cultures consisted of HCC1569 (HER2-overexpressing) (obtained from ATCC) cultured in RPMI with 10 % FBS. 3D culture models were generated in Matrigel as described in [74, 75]. Cells were stained with HER2/ErbB2 (29D8) rabbit monoclonal antibody (#2165, Cell Signaling, Danvers MA) followed by anti-rabbit quantum dot (Qdot) 705 (Q11461MP, Thermofisher Waltham, MA). Each staining step takes approximately one hour at room temperature, for a total of two hours.

6.11.2 *Ex vivo* Tissue Margin

Ex vivo tissue margins were generated from patient samples of HER2+ and triple-negative breast cancers and compared with normal tissue counterparts from the same patient. Anonymized patient samples were obtained from Bioserve (Betsfiel, MD). Tissue was frozen in order to preserve enzyme and antigen functionality and 6 µm sections (slices) were cut for imaging. These slices of HER2+ tumor were stained with anti-HER2 antibody and secondarily with Qdot 705. Each staining step takes approximately one hour at room temperature, for a total of two hours. Adjacent slices were H&E stained for comparison. The slices were allowed to return to room temperature before imaging, preserving their optical properties.

6.11.3 *In Vivo* Mouse Tumor Models

The performance of our fluorescent probe was evaluated using *in vivo* breast tumor mice models. Mice were subcutaneously implanted with either HCC1569, a HER2+ breast cancer cell line targeted by our fluorescent probe, or MDA-MB-231, a HER2- breast cancer cell line that is not targeted. Mice were partitioned into four groups, with one HCC1569 implanted mouse and one MDA-MB-231 implanted mouse (negative control) in each group. Group 1-4 mice were implanted with either HCC1569 or MDA-MB-231 cells with amounts of 0.25, 0.5, 1, and 2.5 million cells, respectively, into the mammary gland on both sides. After three weeks, the mice were given 200 µL injections containing 0.8 mg of a Trastuzumab-IR700DX probe through the tail vein. Imaging was performed over the subsequent 72 hours. The Trastuzumab-IR700DX conjugate was prepared by LI-COR Biosciences (Lincoln, NE).

6.11.4 Test Setup

The custom imager with optical filter is mounted on a PCB. A field-programmable gate array (Opal Kelly XEM6010-LX45), also mounted on the PCB, is used to communicate between the image sensor and a PC. A slide containing 3D cancer cell cultures is placed on an XY-stage (MLS203) above an inverted fluorescence microscope (Leica DM-IRB) with a 2.5X objective. The custom imager is suspended above the microscope and positioned in contact with the cell sample slide using a Thorlabs XYZ stage (RB13M). Light from an Excelitas X-Cite 120LED attached to the microscope is passed through an optical filter to illuminate the 3D cultures or tissue samples at 450 nm or 650 nm when capturing the fluorescence microscope images. For the custom sensor images, collimated laser diode light sources at 455 nm or 633 nm are used for quantum dots and organic fluorophores, respectively. The laser diodes were purchased from QPhotonics and collimators from Thorlabs. Fluorescence microscope images are collected above 700 nm by the custom image sensor and a Hamamatsu ORCA-Flash4.0 V2 microscope camera simultaneously. An IVIS Spectrum

live-animal imaging system was used to capture images of the live mice and excised mouse tissue.

Chapter 7

Conclusion

Although the presence of microscopic residual tumor after a resection is known to significantly increase the chance of cancer recurrence across cancer subtypes, thorough, rapid visualization with 200 cell resolution within the small, complex, tumor bed remains a persistent challenge. The proposed scalable contact fluorescence image sensor can both fit and be maneuvered within a tumor cavity while imaging rapidly. It is enabled by a combination of on-chip angle-selective gratings integrated in a high-sensitivity custom CMOS image sensor and an integrated amorphous silicon optical filter.

The imager has been tested with a variety of breast cancer 3D cell culture, human breast tissue, and mouse tumor models in order to characterize its sensitivity, robustness to variation, and applicability to the operating room setting. Additionally, we have described algorithms for image deconvolution and automatic tumor cluster recognition in order to improve image quality and demonstrate the sensor can be used as part of an automated system for cancer detection, respectively. The sensor does not require microfluidics, cell cultures, or chemical reactions to be performed on its surface and instead cancer is labeled using a systemic injection of an antibody-fluorophore conjugate either on the same day as surgery or in the preceding days. Precision fabrication is not needed to deposit the amorphous silicon absorption filter and a standard CMOS process has been used to keep the cost of the sensor to a minimum, allowing it to be easily disposable.

A comparison of the imager presented in this paper to several other chip-scale imagers for biomedical applications appears in Table 1. These imagers generally fall into two categories: those that are capable of performing *in vivo* imaging ([44, 45]) and those that have been designed for lab-on-a-chip applications ([4, 46, 47]). The former sensors are only capable of imaging single points or large areas of tumor tissue and do not have sufficient resolution to image microscopic residual cancer consisting of foci containing only hundreds of cancer cells. The latter sensors can be capable of high resolution imaging, but typically require microfluidics or cell/tissue samples

	2011 [44]	2016 [45]	2009 [46]	2012 [47]	2017 [4]	This work
Detection method	Fluorescence	Fluorescence	Fluorescence	Chemiluminescence	Fluorescence	Fluorescence
Technology	0.18 µm CMOS	Discrete comp.	0.35 µm	0.35 µm	65 nm CMOS	0.18 µm CMOS
For *in vivo* use?	**Yes**	**Yes**	No	No	No	**Yes**
Array size	Single photodiode	6 photodiode clusters	7X8	128X64	Single photodiode	80X36
Pixel size	0.75 mm^2	1 mm^2	250 µmX250 µm	19 µmX19 µm	91.4 µmX123 µm	55 µmX55 µm
Excitation Power	N/A	500 mW*	3 mW	N/A	4 mW	7.5 mW
Imaging Rate	N/A	10 scan/s	N/A	N/A	N/A	20–100 frame/s
Integration time	500 µs	N/A	1 s	1–90 s	0.1–1 s	10–50 ms

Table 7.1: Performance Comparison to Other Chip-Scale Bioimagers
* Estimated based on reported laser diode current and datasheet.

to be placed on the ASIC surface, which make them unsuitable for *in vivo* imaging. The custom sensor described in this work combines the best qualities of both of these types of sensors. It has the high resolution and sensitivity necessary for detecting microscopic cancer, while maintaining a small form factor and fast imaging rate.

In summary, we have demonstrated highly sensitive tumor imaging using a scalable and lens-free platform that is able to detect cancer intraoperatively in real-time. This platform can be used to image any type of cancer with a targeted antibody and the sensor is small enough to be manipulable inside tumor cavities typically found in modern minimally invasive surgical procedures.

Bibliography

[1] A. Wang, P. R. Gill, and A. Molnar, "An angle-sensitive CMOS imager for single-sensor 3d photography," in *2011 IEEE International Solid-State Circuits Conference*, Feb. 2011, pp. 412–414.

[2] S. Sivaramakrishnan, A. Wang, P. Gill, and A. Molnar, "Design and Characterization of Enhanced Angle Sensitive Pixels," *IEEE Transactions on Electron Devices*, vol. 63, no. 1, pp. 113–119, Jan. 2016.

[3] S. Jayasuriya, S. Sivaramakrishnan, E. Chuang, D. Guruaribam, A. Wang, and A. Molnar, "Dual light field and polarization imaging using CMOS diffractive image sensors," *Opt. Lett., OL*, vol. 40, no. 10, pp. 2433–2436, May 2015.

[4] L. Hong and K. Sengupta, "Fully Integrated Optical Spectrometer in Visible and Near-IR in CMOS," *IEEE Transactions on Biomedical Circuits and Systems*, vol. 11, no. 6, pp. 1176–1191, Dec. 2017.

[5] A. E. Giuliano, J. L. Connolly, S. B. Edge, E. A. Mittendorf, H. S. Rugo, L. J. Solin, D. L. Weaver, D. J. Winchester, and G. N. Hortobagyi, "Breast Cancer—Major changes in the American Joint Committee on Cancer eighth edition cancer staging manual," *CA: A Cancer Journal for Clinicians*, vol. 67, no. 4, pp. 290–303, 2017.

[6] K. L. Kummerow, L. Du, D. F. Penson, Y. Shyr, and M. A. Hooks, "Nationwide Trends in Mastectomy for Early-Stage Breast Cancer," *JAMA Surg*, vol. 150, no. 1, pp. 9–16, Jan. 2015.

[7] R. L. Siegel, K. D. Miller, and A. Jemal, "Cancer statistics, 2015," *CA: A Cancer Journal for Clinicians*, vol. 65, no. 1, pp. 5–29, Jan. 2015.

[8] L. E. McCahill, R. M. Single, E. J. A. Bowles, H. S. Feigelson, T. A. James, T. Barney, J. M. Engel, and A. A. Onitilo, "Variability in Reexcision Following Breast Conservation Surgery," *JAMA*, vol. 307, no. 5, pp. 467–475, Feb. 2012.

[9] L. G. Wilke, T. Czechura, C. Wang, B. Lapin, E. Liederbach, D. P. Winchester, and K. Yao, "Repeat Surgery After Breast Conservation for the Treatment of

Stage 0 to II Breast Carcinoma: A Report From the National Cancer Data Base, 2004-2010," *JAMA Surg*, vol. 149, no. 12, pp. 1296–1305, Dec. 2014.

[10] A. B. Chagpar, B. K. Killelea, T. N. Tsangaris, M. Butler, K. Stavris, F. Li, X. Yao, V. Bossuyt, M. Harigopal, D. R. Lannin, L. Pusztai, and N. R. Horowitz, "A Randomized, Controlled Trial of Cavity Shave Margins in Breast Cancer," *New England Journal of Medicine*, vol. 373, no. 6, pp. 503–510, Aug. 2015.

[11] S. E. Singletary, "Surgical margins in patients with early-stage breast cancer treated with breast conservation therapy," *The American Journal of Surgery*, vol. 184, no. 5, pp. 383–393, Nov. 2002.

[12] Early Breast Cancer Trialists' Collaborative Group (EBCTCG), "Effects of radiotherapy and of differences in the extent of surgery for early breast cancer on local recurrence and 15-year survival: an overview of the randomised trials," *The Lancet*, vol. 366, no. 9503, pp. 2087–2106, Dec. 2005.

[13] T. A. Buchholz, M. R. Somerfield, J. J. Griggs, S. El-Eid, M. E. H. Hammond, G. H. Lyman, G. Mason, and L. A. Newman, "Margins for Breast-Conserving Surgery With Whole-Breast Irradiation in Stage I and II Invasive Breast Cancer: American Society of Clinical Oncology Endorsement of the Society of Surgical Oncology/American Society for Radiation Oncology Consensus Guideline," *Journal of Clinical Oncology*, vol. 32, no. 14, pp. 1502–1506, May 2014.

[14] M. S. Moran, S. J. Schnitt, A. E. Giuliano, J. R. Harris, S. A. Khan, J. Horton, S. Klimberg, M. Chavez-MacGregor, G. Freedman, N. Houssami, P. L. Johnson, and M. Morrow, "Society of Surgical Oncology–American Society for Radiation Oncology Consensus Guideline on Margins for Breast-Conserving Surgery With Whole-Breast Irradiation in Stages I and II Invasive Breast Cancer," *International Journal of Radiation Oncology*Biology*Physics*, vol. 88, no. 3, pp. 553–564, Mar. 2014.

[15] J. A. Wieder and M. S. Soloway, "Incidence, Etiology, Location, Prevention and Treatment of Positive Surgical Margincs after Radical Prostatectomy for Prostate Cancer," *The Journal of Urology*, vol. 160, no. 2, pp. 299–315, Aug. 1998.

[16] J. A. Eastham, M. W. Kattan, E. Riedel, C. B. Begg, T. M. Wheeler, C. Gerigk, M. Gonen, V. Reuter, and P. T. Scardino, "Variations Among Individual Surgeons in the Rate of Positive Surgical Margins in Radical Prostatectomy Specimens," *The Journal of Urology*, vol. 170, no. 6, Part 1, pp. 2292–2295, Dec. 2003.

[17] A. J. Stephenson, P. T. Scardino, M. W. Kattan, T. M. Pisansky, K. M. Slawin, E. A. Klein, M. S. Anscher, J. M. Michalski, H. M. Sandler, D. W. Lin, J. D.

Forman, M. J. Zelefsky, L. L. Kestin, C. G. Roehrborn, C. N. Catton, T. L. DeWeese, S. L. Liauw, R. K. Valicenti, D. A. Kuban, and A. Pollack, "Predicting the Outcome of Salvage Radiation Therapy for Recurrent Prostate Cancer After Radical Prostatectomy," *Journal of Clinical Oncology*, vol. 25, no. 15, pp. 2035–2041, May 2007.

[18] F. Sardanelli, G. M. Giuseppetti, P. Panizza, M. Bazzocchi, A. Fausto, G. Simonetti, V. Lattanzio, and A. Del Maschio, "Sensitivity of MRI Versus Mammography for Detecting Foci of Multifocal, Multicentric Breast Cancer in Fatty and Dense Breasts Using the Whole-Breast Pathologic Examination as a Gold Standard," *American Journal of Roentgenology*, vol. 183, no. 4, pp. 1149–1157, Oct. 2004.

[19] M. A. Haider, T. H. van der Kwast, J. Tanguay, A. J. Evans, A.-T. Hashmi, G. Lockwood, and J. Trachtenberg, "Combined T2-Weighted and Diffusion-Weighted MRI for Localization of Prostate Cancer," *American Journal of Roentgenology*, vol. 189, no. 2, pp. 323–328, Aug. 2007.

[20] J. V. Frangioni, "In vivo near-infrared fluorescence imaging," *Current Opinion in Chemical Biology*, vol. 7, no. 5, pp. 626–634, Oct. 2003.

[21] X. Gao, Y. Cui, R. M. Levenson, L. W. K. Chung, and S. Nie, "*In vivo* cancer targeting and imaging with semiconductor quantum dots," *Nature Biotechnology*, vol. 22, no. 8, pp. 969–976, Aug. 2004.

[22] H. Tada, H. Higuchi, T. M. Wanatabe, and N. Ohuchi, "In vivo Real-time Tracking of Single Quantum Dots Conjugated with Monoclonal Anti-HER2 Antibody in Tumors of Mice," *Cancer Res*, vol. 67, no. 3, pp. 1138–1144, Feb. 2007.

[23] M. McElroy, S. Kaushal, G. A. Luiken, M. A. Talamini, A. R. Moossa, R. M. Hoffman, and M. Bouvet, "Imaging of Primary and Metastatic Pancreatic Cancer Using a Fluorophore-Conjugated Anti-CA19-9 Antibody for Surgical Navigation," *World J Surg*, vol. 32, no. 6, pp. 1057–1066, Jun. 2008.

[24] M. Ogawa, N. Kosaka, P. L. Choyke, and H. Kobayashi, "In vivo Molecular Imaging of Cancer with a Quenching Near-Infrared Fluorescent Probe Using Conjugates of Monoclonal Antibodies and Indocyanine Green," *Cancer Res*, vol. 69, no. 4, pp. 1268–1272, Feb. 2009.

[25] G. M. van Dam, G. Themelis, L. M. A. Crane, N. J. Harlaar, R. G. Pleijhuis, W. Kelder, A. Sarantopoulos, J. S. de Jong, H. J. G. Arts, A. G. J. van der Zee, J. Bart, P. S. Low, and V. Ntziachristos, "Intraoperative tumor-specific fluorescence imaging in ovarian cancer by folate receptor-α targeting: first in-human results," *Nat Med*, vol. 17, no. 10, pp. 1315–1319, Oct. 2011.

[26] E. L. Rosenthal, J. M. Warram, E. d. Boer, T. K. Chung, M. L. Korb, M. Brandwein-Gensler, T. V. Strong, C. E. Schmalbach, A. B. Morlandt, G. Agarwal, Y. E. Hartman, W. R. Carroll, J. S. Richman, L. K. Clemons, L. M. Nabell, and K. R. Zinn, "Safety and Tumor Specificity of Cetuximab-IRDye800 for Surgical Navigation in Head and Neck Cancer," *Clin Cancer Res*, vol. 21, no. 16, pp. 3658–3666, Aug. 2015.

[27] M. Koch, J. S. d. Jong, J. Glatz, P. Symvoulidis, L. E. Lamberts, A. L. L. Adams, M. E. G. Kranendonk, A. G. T. T. v. Scheltinga, M. Aichler, L. Jansen, J. d. Vries, M. N. L.-d. Hooge, C. P. Schröder, A. Jorritsma-Smit, M. D. Linssen, E. d. Boer, B. v. d. Vegt, W. B. Nagengast, S. G. Elias, S. Oliveira, A. J. Witkamp, W. P. T. M. Mali, E. V. d. Wall, P. B. Garcia-Allende, P. J. v. Diest, E. G. E. d. Vries, A. Walch, G. M. v. Dam, and V. Ntziachristos, "Threshold Analysis and Biodistribution of Fluorescently Labeled Bevacizumab in Human Breast Cancer," *Cancer Res*, vol. 77, no. 3, pp. 623–631, Feb. 2017.

[28] K. Gotoh, T. Yamada, O. Ishikawa, H. Takahashi, H. Eguchi, M. Yano, H. Ohigashi, Y. Tomita, Y. Miyamoto, and S. Imaoka, "A novel image-guided surgery of hepatocellular carcinoma by indocyanine green fluorescence imaging navigation," *Journal of Surgical Oncology*, vol. 100, no. 1, pp. 75–79, Mar. 2009.

[29] E. de Boer, S. Samuel, D. N. French, J. M. Warram, T. R. Schoeb, E. L. Rosenthal, and K. R. Zinn, "Biodistribution Study of Intravenously Injected Cetuximab-IRDye700dx in Cynomolgus Macaques," *Mol Imaging Biol*, vol. 18, no. 2, pp. 232–242, Apr. 2016.

[30] S. L. Troyan, V. Kianzad, S. L. Gibbs-Strauss, S. Gioux, A. Matsui, R. Oketokoun, L. Ngo, A. Khamene, F. Azar, and J. V. Frangioni, "The FLARE^{TM} Intraoperative Near-Infrared Fluorescence Imaging System: A First-in-Human Clinical Trial in Breast Cancer Sentinel Lymph Node Mapping," *Annals of Surgical Oncology*, vol. 16, no. 10, pp. 2943–2952, Oct. 2009.

[31] J. W. Duparré and F. C. Wippermann, "Micro-optical artificial compound eyes," *Bioinspir. Biomim.*, vol. 1, no. 1, p. R1, 2006.

[32] V. I. Shaoulov and J. P. Rolland, "Compact relay lenses using microlenslet arrays," vol. 4832. International Society for Optics and Photonics, Dec. 2002, pp. 74–80.

[33] R. Völkel, M. Eisner, and K. J. Weible, "Miniaturized imaging systems," *Microelectronic Engineering*, vol. 67-68, no. Supplement C, pp. 461–472, Jun. 2003.

[34] S. B. Mondal, S. Gao, N. Zhu, G. P. Sudlow, K. Liang, A. Som, W. J. Akers, R. C. Fields, J. Margenthaler, R. Liang, V. Gruev, and S. Achilefu, "Binocular

Goggle Augmented Imaging and Navigation System provides real-time fluorescence image guidance for tumor resection and sentinel lymph node mapping," *Scientific Reports*, vol. 5, p. srep12117, Jul. 2015.

[35] Y. Liu, A. Q. Bauer, W. J. Akers, G. Sudlow, K. Liang, D. Shen, M. Y. Berezin, J. P. Culver, and S. Achilefu, "Hands-free, wireless goggles for near-infrared fluorescence and real-time image-guided surgery," *Surgery*, vol. 149, no. 5, pp. 689–698, May 2011.

[36] A. M. Zysk, K. Chen, E. Gabrielson, L. Tafra, E. A. M. Gonzalez, J. K. Canner, E. B. Schneider, A. J. Cittadine, P. S. Carney, S. A. Boppart, K. Tsuchiya, K. Sawyer, and L. K. Jacobs, "Intraoperative Assessment of Final Margins with a Handheld Optical Imaging Probe During Breast-Conserving Surgery May Reduce the Reoperation Rate: Results of a Multicenter Study," *Ann Surg Oncol*, vol. 22, no. 10, pp. 3356–3362, Oct. 2015.

[37] Y. Yoon, A. M. Mohs, M. C. Mancini, S. Nie, and H. Shim, "Combination of an Integrin-Targeting NIR Tracer and an Ultrasensitive Spectroscopic Device for Intraoperative Detection of Head and Neck Tumor Margins and Metastatic Lymph Nodes," *Tomography*, vol. 2, no. 3, pp. 215–222, Sep. 2016.

[38] M. Jermyn, K. Mok, J. Mercier, J. Desroches, J. Pichette, K. Saint-Arnaud, L. Bernstein, M.-C. Guiot, K. Petrecca, and F. Leblond, "Intraoperative brain cancer detection with Raman spectroscopy in humans," *Science Translational Medicine*, vol. 7, no. 274, pp. 274ra19–274ra19, Feb. 2015.

[39] A. M. Mohs, M. C. Mancini, S. Singhal, J. M. Provenzale, B. Leyland-Jones, M. D. Wang, and S. Nie, "Hand-held Spectroscopic Device for In Vivo and Intraoperative Tumor Detection: Contrast Enhancement, Detection Sensitivity, and Tissue Penetration," *Anal. Chem.*, vol. 82, no. 21, pp. 9058–9065, Nov. 2010.

[40] M. Villiger, D. Lorenser, R. A. McLaughlin, B. C. Quirk, R. W. Kirk, B. E. Bouma, and D. D. Sampson, "Deep tissue volume imaging of birefringence through fibre-optic needle probes for the delineation of breast tumour," *Scientific Reports*, vol. 6, p. srep28771, Jul. 2016.

[41] A. Cousins, G. L. Balalis, S. K. Thompson, D. F. Morales, A. Mohtar, A. B. Wedding, and B. Thierry, "Novel Handheld Magnetometer Probe Based on Magnetic Tunnelling Junction Sensors for Intraoperative Sentinel Lymph Node Identification," *Scientific Reports*, vol. 5, p. srep10842, Jun. 2015.

[42] S. Türkcan, D. J. Naczynski, R. Nolley, L. S. Sasportas, D. M. Peehl, and G. Pratx, "Endoscopic detection of cancer with lensless radioluminescence imaging and machine vision," *Scientific Reports*, vol. 6, p. srep30737, Aug. 2016.

[43] D. Shin, M. C. Pierce, A. M. Gillenwater, M. D. Williams, and R. R. Richards-Kortum, "A Fiber-Optic Fluorescence Microscope Using a Consumer-Grade Digital Camera for In Vivo Cellular Imaging," *PLoS ONE*, vol. 5, no. 6, p. e11218, Jun. 2010.

[44] R. T. Heitz, D. B. Barkin, T. D. O'Sullivan, N. Parashurama, S. S. Gambhir, and B. A. Wooley, "A low noise current readout architecture for fluorescence detection in living subjects," in *2011 IEEE International Solid-State Circuits Conference*, Feb. 2011, pp. 308–310.

[45] P. Demosthenous, C. Pitris, and J. Georgiou, "Infrared Fluorescence-Based Cancer Screening Capsule for the Small Intestine," *IEEE Transactions on Biomedical Circuits and Systems*, vol. 10, no. 2, pp. 467–476, Apr. 2016.

[46] B. Jang, P. Cao, A. Chevalier, A. Ellington, and A. Hassibi, "A CMOS fluorescent-based biosensor microarray," in *2009 IEEE International Solid-State Circuits Conference - Digest of Technical Papers*, Feb. 2009, pp. 436–437,437a.

[47] R. R. Singh, L. Leng, A. Guenther, and R. Genov, "A CMOS-Microfluidic Chemiluminescence Contact Imaging Microsystem," *IEEE Journal of Solid-State Circuits*, vol. 47, no. 11, pp. 2822–2833, Nov. 2012.

[48] N. Maeda, Y. S. Kim, Y. Hikosaka, T. Eshita, H. Kitada, K. Fujimoto, Y. Mizushima, K. Suzuki, T. Nakamura, A. Kawai, K. Arai, and T. Ohba, "Development of sub 10μm ultra-thinning technology using device wafers for 3d manufacturing of terabit memory," in *2010 Symposium on VLSI Technology*, Jun. 2010, pp. 105–106.

[49] K. Nishimura, Y. Sato, J. Hirase, R. Sakaida, M. Yanagida, T. Tamaki, M. Takase, H. Kanehara, M. Murakami, and Y. Inoue, "An over 120db simultaneous-capture wide-dynamic-range 1.6e- ultra-low-reset-noise organic-photoconductive-film CMOS image sensor," in *ISSCC Digest of Technical Papers*, Jan. 2016, pp. 110–111.

[50] J. Bogaerts, R. Lafaille, M. Borremans, J. Guo, B. Ceulemans, G. Meynants, N. Sarhangnejad, G. Arsinte, V. Statescu, and S. v. d. Groen, "105x65mm2 391mpixel CMOS image sensor with >78db dynamic range for airborne mapping applications," in *ISSCC Digest of Technical Papers*, Jan. 2016, pp. 114–115.

[51] F. P. Bolin, L. E. Preuss, R. C. Taylor, and R. J. Ference, "Refractive index of some mammalian tissues using a fiber optic cladding method," *Appl. Opt., AO*, vol. 28, no. 12, pp. 2297–2303, Jun. 1989.

[52] G. Agranov, V. Berezin, and R. H. Tsai, "Crosstalk and microlens study in a color CMOS image sensor," *IEEE Transactions on Electron Devices*, vol. 50, no. 1, pp. 4–11, Jan. 2003.

[53] H. Rhodes, G. Agranov, C. Hong, U. Boettiger, R. Mauritzson, J. Ladd, I. Karasev, J. McKee, E. Jenkins, W. Quinlin, I. Patrick, J. Li, X. Fan, R. Panicacci, S. Smith, C. Mouli, and J. Bruce, "CMOS imager technology shrinks and image performance," in *2004 IEEE Workshop on Microelectronics and Electron Devices*, 2004, pp. 7–18.

[54] A. Penzkofer and P. Sperber, "Measurement of absorption cross sections in the long-wavelength region of the S0-S1 absorption band of dyes," *Chemical Physics*, vol. 88, no. 2, pp. 309–313, Aug. 1984.

[55] L. Wang, A. K. Gaigalas, and V. Reipa, "Optical properties of Alexa^{TM} 488 and Cy^{TM} 5 immobilized on a glass surface," *Biotechniques*, vol. 38, no. 1, pp. 127–132, 2005.

[56] G. Hong, S. M. Tabakman, K. Welsher, Z. Chen, J. T. Robinson, H. Wang, B. Zhang, and H. Dai, "Near-Infrared-Fluorescence-Enhanced Molecular Imaging of Live Cells on Gold Substrates," *Angew. Chem. Int. Ed.*, vol. 50, no. 20, pp. 4644–4648, May 2011.

[57] K. Ito, M. Mitsunaga, T. Nishimura, M. Saruta, T. Iwamoto, H. Kobayashi, and H. Tajiri, "Near-Infrared Photochemoimmunotherapy by Photoactivatable Bifunctional Antibody–Drug Conjugates Targeting Human Epidermal Growth Factor Receptor 2 Positive Cancer," *Bioconjugate Chem.*, vol. 28, no. 5, pp. 1458–1469, May 2017.

[58] M. Garland, J. J. Yim, and M. Bogyo, "A Bright Future for Precision Medicine: Advances in Fluorescent Chemical Probe Design and Their Clinical Application," *Cell Chemical Biology*, vol. 23, no. 1, pp. 122–136, Jan. 2016.

[59] J. T. Alander, I. Kaartinen, A. Laakso, T. Pätilä, T. Spillmann, V. V. Tuchin, M. Venermo, and P. Välisuo, "A Review of Indocyanine Green Fluorescent Imaging in Surgery," *Journal of Biomedical Imaging*, vol. 2012, pp. 7:7–7:7, Jan. 2012.

[60] M. Dandin, P. Abshire, and E. Smela, "Optical filtering technologies for integrated fluorescence sensors," *Lab on a Chip*, vol. 7, no. 8, pp. 955–977, 2007.

[61] L. Hong, S. McManus, H. Yang, and K. Sengupta, "A fully integrated CMOS fluorescence biosensor with on-chip nanophotonic filter," in *2015 Symposium on VLSI Circuits (VLSI Circuits)*, Jun. 2015, pp. C206–C207.

[62] D. Ho, M. O. Noor, U. J. Krull, G. Gulak, and R. Genov, "CMOS Spectrally-Multiplexed FRET-on-a-Chip for DNA Analysis," *IEEE Transactions on Biomedical Circuits and Systems*, vol. 7, no. 5, pp. 643–654, Oct. 2013.

[63] C. Lee, B. Johnson, and A. Molnar, "An on-chip 72x60 angle-sensitive single photon image sensor array for lens-less time-resolved 3-D fluorescence lifetime imaging," in *2014 Symposium on VLSI Circuits Digest of Technical Papers*, Jun. 2014, pp. 1–2.

[64] A. F. Coskun, I. Sencan, T.-W. Su, and A. Ozcan, "Lensfree Fluorescent On-Chip Imaging of Transgenic Caenorhabditis elegans Over an Ultra-Wide Field-of-View," *PLOS ONE*, vol. 6, no. 1, p. e15955, Jan. 2011.

[65] R. H. Klazes, M. H. L. M. van den Broek, J. Bezemer, and S. Radelaar, "Determination of the optical bandgap of amorphous silicon," *Philosophical Magazine Part B*, vol. 45, no. 4, pp. 377–383, Apr. 1982.

[66] G. D. Cody, T. Tiedje, B. Abeles, B. Brooks, and Y. Goldstein, "Disorder and the optical-absorption edge of hydrogenated amorphous silicon," *Physical Review Letters*, vol. 47, no. 20, p. 1480, 1981.

[67] C.-K. Chung, M.-Q. Tsai, P.-H. Tsai, and C. Lee, "Fabrication and characterization of amorphous Si films by PECVD for MEMS," *Journal of Micromechanics and Microengineering*, vol. 15, no. 1, pp. 136–142, Jan. 2005.

[68] B. Lipovšek, A. Jóskowiak, J. Krč, M. Topič, D. M. F. Prazeres, V. Chu, and J. P. Conde, "Characterisation of hydrogenated silicon–carbon alloy filters with different carbon composition for on-chip fluorescence detection of biomolecules," *Sensors and Actuators A: Physical*, vol. 163, no. 1, pp. 96–100, Sep. 2010.

[69] C. Richard, A. Renaudin, V. Aimez, and P. G. Charette, "An integrated hybrid interference and absorption filter for fluorescence detection in lab-on-a-chip devices," *Lab on a Chip*, vol. 9, no. 10, pp. 1371–1376, 2009.

[70] E. Yıldırım, Ç. Arpali, and S. A. Arpali, "Implementation and characterization of an absorption filter for on-chip fluorescent imaging," *Sensors and Actuators B: Chemical*, vol. 242, pp. 318–323, Apr. 2017.

[71] L. Blockstein, C. C. Luk, A. K. Mudraboyina, N. I. Syed, and O. Yadid-Pecht, "A PVAc-Based Benzophenone-8 Filter as an Alternative to Commercially Available Dichroic Filters for Monitoring Calcium Activity in Live Neurons via Fura-2 AM," *IEEE Photonics Journal*, vol. 4, no. 3, pp. 1004–1012, Jun. 2012.

[72] E. Carregal-Romero, C. Fernández-Sánchez, A. Eguizabal, S. Demming, S. Büttgenbach, and A. Llobera, "Development and integration of xerogel polymeric absorbance micro-filters into lab-on-chip systems," *Opt. Express, OE*, vol. 20, no. 21, pp. 23 700–23 719, Oct. 2012.

[73] Y. Dattner and O. Yadid-Pecht, "Low Light CMOS Contact Imager with an Integrated Poly-Acrylic Emission Filter for Fluorescence Detection," *Sensors*, vol. 10, no. 5, pp. 5014–5027, May 2010.

[74] C. C. Park, H. Zhang, M. Pallavicini, J. W. Gray, F. Baehner, C. J. Park, and M. J. Bissell, "β1 Integrin Inhibitory Antibody Induces Apoptosis of Breast Cancer Cells, Inhibits Growth, and Distinguishes Malignant from Normal Phenotype in Three Dimensional Cultures and In vivo," *Cancer Res*, vol. 66, no. 3, pp. 1526–1535, Feb. 2006.

[75] J.-M. Nam, Y. Onodera, M. J. Bissell, and C. C. Park, "Breast Cancer Cells in Three-dimensional Culture Display an Enhanced Radioresponse after Coordinate Targeting of Integrin α5β1 and Fibronectin," *Cancer Res*, vol. 70, no. 13, pp. 5238–5248, Jul. 2010.